Synthesis of Sulphated Transition Metal Oxides Supported on Mesoporous Silica using Direct Impregnation Method and Their Catalytic Activities

SHENG KAI LI

A thesis submitted to

Auckland University of Technology

in partial fulfilment of the requirements for the degree

of

Master of Applied Science (MAppSc)

2011

School of Applied Science

Primary Supervisor: Roger WHITING

Table of Content

ATTESTATION OF AUTHORSHIP iii
ACKNOWLEDGEMENT iv
ABSTRACT v
LIST OF FIGURES vii
LIST OF TABLES ix
LIST OF ABBREVIATIONS x

Chapter 1 INTRODUCTION 1
1.1 Sulfate Promoted Transition Metal Oxides as Catalysts 1
1.1.1 Concepts of acids and superacids 1
1.1.2 Catalytic properties of sulfate promoted transition metal oxides 5
1.1.3 Limitation of the sulfated metal oxides in catalysis 15
1.2 Mesoporous Silica Materials as Catalysts 15
1.2.1 Development history of the mesoporous silica materials 16
1.2.2 Catalytic properties of mesoporous silica material 17
1.3 Sulfated Metal Oxides Supported on Mesoporous Silica 20
1.3.1 Advantages for the combination 20
1.3.2 Synthesis methods 20
1.3.3 Past work and current gap 22
1.4 Research Objective 23
1.5 Experimental Design 23

Chapter 2 EXPERIMENTAL METHODS 26
2.1 Chemical Reagents 26
2.2 Catalysts Synthesis 27
2.3 Catalytic Activity Evaluation using Acetic acid and *n*-Butanol Esterification 30
2.4 Catalyst Characterization Methods 32
2.4.1 Powder X-ray diffraction (XRD) 32
2.4.2 Nitrogen adsorption isotherm method 33
2.4.3 Scanning electron microscope (SEM) 34
2.4.4 Diffuse reflectance infrared fourier transform spectroscopy (DRIFTS) 35
2.4.5 Hammett indicators for acid strength measurement 36
2.4.6 Thermal gravimetric analysis 37

Chapter 3 RESULTS AND DISCUSSIONS 39
3.1 Catalytic Effects on Acetic Acid and *n*-Butanol Esterification 39
3.1.1 Esterification mechanism 39
3.1.2 Determination of the product composition 42
3.1.3 Esterification rates analysis 46
3.2 Formation of the Catalysts 50

3.2.1 MCM-41 structure formation by TEOS and CTAB 50
3.2.2 Effects of thermal treatments 52
3.2.3 Thermal decomposition analysis 55
3.3 Catalysts Struture and Surface Characterization 57
3.3.1 Catalysts crystallography and morphology 58
3.3.2 Catalysts surface area and porosity determination 66
3.4 Nature of Active Sites 80
3.4.1 Acidity measurements of solid superacid catalysts 80
3.4.2 S-TiO_2/MCM-41 active sites 82
3.4.3 S-ZrO_2/MCM-41 active sites 87
3.4.4 S-Fe_2O_3/MCM-41 active sites 90

Chapter 4 CONCLUSIONS AND DEVELOPMENTS 94
4.1 Overall Conclusions 94
4.2 Further Developments 96

REFERENCES 97

APPENDIX 103

ATTESTATION OF AUTHORSHIP

I hereby declare that this submission is my own work and that, to the best of my knowledge and belief, it contains no material previously published or written by another person except that which appears in the citations and acknowledgements. Nor does it contain material which to a substantial extent I have submitted for the qualification for any other degree of another university or other institution of higher learning.

Candidate Signature:_____

Date:_____

ACKNOWLEDGEMENT

I would like to show my great appreciation to my primary supervisor Dr. Roger Whiting of Auckland University of Technology. The thesis would not have been possible without Dr. Whiting's guidance, suggestions, and encouragement throughout the course.

Also thanks to my secondary and additional supervisor Dr. John Robertson of Auckland University of Technology and Dr. Yuhong Wang of Shanghai Institute of Technology for their valuable advices and help during the project.

In addition, I am indebted to Geoff Waterhouse and his PhD fellow Vedran Jovic of the University of Auckland for their assistance in the nitrogen adsorption isotherm and X-ray diffraction measurements. Completing this work proved to be a mission for the whole of April.

Lastly I'm grateful to my parents for their financial and moral support to do my master degree in New Zealand.

ABSTRACT

The purpose of the present study is to further develop a method of direct impregnation in the preparation of sulfated titania, zirconia and ferric oxides supported on the mesoporous silica molecular sieve (MCM-41) as acid catalyst composites (C. Chen et al., 2001; Y. Wang et al., 2009) and to characterize their structures and acid nature.

Sulfated transition metal oxides such as S-TiO_2, S-ZrO_2, and S-Fe_2O_3 as solid superacids have been received much attention due to their significant catalytic activities in hydrocarbon conversions such as esterification, isomerization, alkylation, etc. The remarkable catalytic activities for these sulfated transition metal oxides are mainly attributed to their properties as superacids. The generation and structures of Brönsted and Lewis acid sites are responsible for these activities (Corma et al., 1994; Yadav & Nair, 1999). Unfortunately, the relatively small surface area for the sulfated transition metal oxides may limit their usefulness in catalytic activities (J. Wang & Mou, 2008; Y. Wang et al., 2009).

Nano-scale particle mesoporous molecular sieves have advantages in catalysis due to their large pore size, pore volume, uniform pore structures and high specific surface area (Giraldo et al., 2007; Kresge et al., 1992). The large pore size and volume provide adequate diffusion of molecules through the catalyst pores. Fine solid powders with high surface areas ensure probable collisions among the reaction substrates. However, these mesoporous silica materials such as MCM-41 and SBA-15 have their limitation in the low acid strength without the addition of other metal ions (Giraldo et al., 2007).

A direct impregnation method has been developed to explore the positive characteristic of both materials discussed above. The sulfated metal oxides continue manifest their remarkable catalytic activities while the high surface area of the mesoporous silica structure ensures a large number of acid sites. The use of direct

exchange of metal containing precursors in the as-synthesized MCM-41 substrate produced catalyst composites which were evaluated for the esterification of acetic acid and *n*-butanol. S-TiO_2/MCM-41 and S-ZrO_2/MCM-41 catalyst composites exhibit the higher esterification rates than S-Fe_2O_3/MCM-41. After calcination the MCM-41 and metal compounds were found to agglomerate and the metals dispersed onto as well as inside the mesopore structure. S-TiO_2/MCM-41 with up to 80wt% metal loading still retained the MCM-41 mesoporous structure after high temperature calcination. However for S-ZrO_2/MCM-41 and S-Fe_2O_3/MCM-41 composites, the mesopores became blocked with up to 70wt% and 50wt% content loadings respectively. Both Brönsted and Lewis acid sites were detected on the three kinds of catalyst composites in spite of their diminishing in numbers with increasing temperature. For both the acid sites and the structures were responsible for the catalytic performances of S-TiO_2/MCM-41, S-ZrO_2/MCM-41, and S-Fe_2O_3/MCM-41 catalyst composites as the solid superacids catalysts in the reactions.

LIST OF FIGURES

Figure 1.1 *Acid strength chart of various kinds of superacids* *3*
Figure 1.2 *FESEM image of SBA-15 mesoporou silica* *17*
Figure 1.3 *Mesoporous silica surface Brönsted acid sites* *19*
Figure 1.4 *Brönsted and Lewis acid sites of MCM-41 with corporation of aluminum* *20*
Figure 1.5 *Catalyst composite synthesis flow chart by the direct impregnation method* *24*

Figure 2.1 *Skeletal formula of tetraethyl orthosilicate, TEOS* *26*
Figure 2.2 *Structure of cetyl trimethylammonium bromide, CTAB* *26*
Figure 2.3 *Batch reactor set of acetic acid glacial and n-butanol esterification* *30*
Figure 2.4 *SHIMADZU 2010 gas chromatography with FID detector* *31*
Figure 2.5 *Schematic of the SIEMENS D5000 diffractometer* *33*
Figure 2.6 *TriSTAR 3000 micromeritics* *34*
Figure 2.7 *JEOL NeoScope JCM-5000 benchtop scanning electronic microscope* *35*
Figure 2.8 *In-situ cell for pyridine adsorption* *35*
Figure 2.9 *SHIMADZU IR Prestige-21 Infrared spectrophotometer* *36*
Figure 2.10 *Hammett indicators for catalysts acid strength measurement* *37*

Figure 3.1 *IR spectrum of n-Butyl acetate using 70wt% S-TiO_2/MCM-41 catalyst* *42*
Figure 3.2 *IR spectrum of n-Butyl acetate using 70wt% S-ZrO_2/MCM-41 catalyst* *43*
Figure 3.3 *IR spectrum of n-Butyl acetate using 70wt% S-Fe_2O_3/MCM-41 catalyst* *43*
Figure 3.4 *GC chromatogram of the esterification product by using c_i catalyst* *45*
Figure 3.5 *Esterification rates comparison by group I, II, and III catalyst composites* *48*
Figure 3.6 *Catalysts repetitive use test by catalyst composites with 80wt% metal compounds loading* *48*
Figure 3.7 *Refractive index (n_D^{20}) of acetic acid and n-butanol esterification versus 4hrs time on stream by S-TiO_2/MCM-41 catalyst composite* *49*
Figure 3.8 *Formation of MCM-41 like structure by TEOS and CTAB* *52*
Figure 3.9 *Drying process of the wet porous material* *53*
Figure 3.10 *Physical and chemical processes on the catalyst support during drying* *54*
Figure 3.11 *TGA profiles in air of $Ti(SO_4)_2$ and MCM-41* *56*
Figure 3.12 *Working mechanism of the X-ray diffraction* *58*
Figure 3.13 *The Bragg's Law X-ray diffraction* *59*
Figure 3.14 *XRD pattern of the MCM-41 catalyst* *60*
Figure 3.15 *2D and 3D geometrical description of the MCM-41 structure* *61*
Figure 3.16 *Scanning electron micrographs of the MCM-41 sample* *62*
Figure 3.17 *Scanning electron micrographs of S-TiO_2/MCM-41 catalyst composites* *63*
Figure 3.18 *XRD patterns of the S-ZrO_2/MCM-41 catalyst composites* *64*
Figure 3.19 *Scanning electron micrographs of S-ZrO_2/MCM-41 catalyst composites* *65*
Figure 3.20 *Scanning electron micrographs of S-Fe_2O_3/MCM-41 catalyst composites* *65*
Figure 3.21 *MCM-41 adsorption isotherm* *67*
Figure 3.22 *Schematic illustrations of the pore adsorption* *68*

Figure 3.23 *Langmuir and B.E.T. theory of molecular adsorption* *69*
Figure 3.24 *B.E.T. surface area plot for the specific surface area calculation* *71*
Figure 3.25 *Nitrogen adsorption isotherms of S-TiO_2/MCM-41 samples* *72*
Figure 3.26 *Pore size distribution curves of MCM-41 and S-TiO_2/MCM-41 samples* *74*
Figure 3.27 *Nitrogen adsorption isotherms of S-ZrO_2/MCM-41 samples* *75*
Figure 3.28 *Pore size distribution curves of MCM-41 and S-ZrO_2/MCM-41 samples* *77*
Figure 3.29 *Nitrogen adsorption isotherms of S-Fe_2O_3/MCM-41 samples* *78*
Figure 3.30 *Pore size distribution curves of MCM-41 and S-Fe_2O_3/MCM-41 samples* *79*
Figure 3.31 *FTIR spectra of group I samples annealed at 623 K for 2 hr* *84*
Figure 3.32 *C_{2v} chelate and C_{2v} bridge sulfate structures* *84*
Figure 3.33 *In-situ DRIFT-pyridine adsorption of S-TiO_2/MCM-41 catalyst composites* *85*
Figure 3.34 *High temperature In-situ DRIFT spectra of 80wt% loading S-TiO_2/MCM-41* ... *86*
Figure 3.35 *FTIR spectra of group II samples annealed at 623 K for 2 hr* *88*
Figure 3.36 *In-situ DRIFT-pyridine adsorption of S-ZrO_2/MCM-41 catalyst composites* *89*
Figure 3.37 *High temperature In-situ DRIFT spectra of 80wt% loading S-ZrO_2/MCM-41* ... *90*
Figure 3.38 *FTIR spectra of group III samples annealed at 623 K for 2 hr* *91*
Figure 3.39 *In-situ DRIFT-pyridine adsorption of S-Fe_2O_3/MCM-41 catalyst composites* ... *92*
Figure 3.40 *High temperature In-situ DRIFT spectra of 80wt% loading S-Fe_2O_3/MCM-41* . *92*

LIST OF TABLES

Table 1.1 *Techniques used for catalyst characterization* *25*

Table 2.1 *Classification of catalyst composites with different groups* *30*
Table 2.2 *Parameters for GC analysis of the synthesized n-butyl acetate* *32*
Table 2.3 *Hammett indicators used for acid strength measurement* *37*

Table 3.1 *Summary of the peak numbers and retention time of the synthesized product via groups of catalyst composites with different metal compounds loadings*.....*46*
Table 3.2 *Overall esterification rates by group I, II, and III catalyst composites*.....*47*
Table 3.3 *Decomposition temperatures of the catalyst composites*.....*57*
Table 3.4 *Relative pressure range from 0.05 to 0.30 for MCM-41 catalyst B.E.T. surface area calculation*.....*70*
Table 3.5 *Surface area and porosity properties of the group I catalyst composites*.....*73*
Table 3.6 *Surface area and porosity properties of the group II catalyst composites* *76*
Table 3.7 *Surface area and porosity properties of the group III catalyst composites*.....*79*
Table 3.8 *Acidity strength of S-TiO_2/MCM-41s by using various Hammett indicators*.....*83*
Table 3.9 *Acidity strength of S-ZrO_2/MCM-41s by using various Hammett indicators*.....*87*

LIST OF ABBREVIATIONS

B.E.T. theory	S. Brunauer, P. H. Emmett, and E. Teller theory
BJH pore size distribution	Barret-Joyner-Halenda pore size distribution
CTAB	Cetyl trimethylammonium bromide
DRIFTS	Diffuse reflectance infrared fourier transform spectroscopy
GC	Gas chromatography
MCM-41	Mobile crystalline of materials
SBA-15	Santa Barbara amorphous (type material)
SEM	Scanning electron microscopy
TEOS	Tetraethylorthosilicate
TGA	Thermal gravimetric analysis
XDR	X-ray diffraction

Chapter 1 INTRODUCTION

1.1 Sulfate Promoted Transition Metal Oxides as Catalysts

Owing to the environmental consideration of the currently used industrial acid catalysts such as phosphoric acid (H_3PO_4), hydrogen fluoride (HF), or hydrochloric acid (HCl), there is an urgent need to develop new catalytic technologies which are non-polluting and atom-efficient (all atoms are involved in the chemical reaction).

Sulfate promoted metal oxides which belong to the category of solid superacids are now receiving more attentions with the aim of replacing the conventional liquid acid catalysts which are highly corrosive, hazardous and environmentally polluting. This kind of solid superacid catalyst has advantages in the strength and type (Brönsted or Lewis) of acidity. These matter for enhanced activity, ease of separation from the reaction mixtures and reaction selectivity and specificity (Yadav & Nair, 1999). In addition, with sulfate ions modifying the metal oxides, they appear to show relatively increased surface areas and improved acidities.

In order to have an adequate understanding of the properties of sulfate promoted metal oxides and their catalytic activities in chemical reactions, there follows a description of the basic acid theories. These involve acid definition, acidity measurement and the superacid concept. The functionalities of this kind of superacids, their preparation, catalytic performance, structure, active site generation, and their limitations are discussed through the following sections.

1.1.1 Concepts of acids and superacids

Defining of acid and acidity The first clear definition of acidity can be traced back before the 20th century. Arrhenius (Arrhenius, 1887) who explained variations in the strength of different acids based on his electrolytic experiments. Arrhenius' theory

suggests acids are substances that dissociate in water and yield the hydrogen ions whereas bases dissociate to yield hydroxide ions.

By 1923 J. N. Brönsted and G.N. Lewis (Brønsted, 1923; Lewis, 1923) generalized their acid-base concepts which are known as the Brönsted-Lowry theory and the Lewis acid-base theory. Brönsted defined an acid as a species that can donate a proton (H^+) and base as a species that can accept it. This dissociation of an acid HA in a solvent can be written as an acid-base equilibrium (1.1):

$$HA \quad S \rightleftharpoons A^- \quad SH \qquad (1.1)$$

Ionization of the Brönsted acid HA in solvent S leads to a new acid SH^+ and a base A^-. In this way, Brönsted base H_2O molecule can be the conjugated base of the acid H_3O^+ as SH^+ (Olah, Prakash, & Sommer, 1985).

On the other hand, Lewis defined an acid as a substance that can accept electrons and a base that can donate electrons. Then, Lewis acids are electron-deficient molecules or ions such as BF_3 or carbocations (carbonium ion). On the other hand, Lewis bases are molecules that contain non-bonded electron pairs (such as in ethers, amines, etc) (Olah et al., 1985). The typical Lewis acid has the reactions (1.2):

$$BF_3 \quad :O\ CH_3\ _2 \rightleftharpoons BF_3{:}O\ CH_3\ _2 \qquad (1.2)$$

Measurement of acidity Since introduced in 1909 by the Danish chemist Sorensen (Sorensen & Enzymstudien, 1909), pH scale has become so far the most commonly used chemical method in acidity or basicity measurement of a solution. The pH scale measures how acidic and/or basic a substance is with ranges from 0 to 14, and a pH 7 is the neutral standard. However, the pH scale has the limiting condition in expressing neither the more concentrated acidity nor the function for non-aqueous solutions (Olah et al., 1985).

The Hammett acidity function, H_0 therefore provides a measure to describe the acidity of concentrated and non-aqueous strong acidic solutions which fills the limitations of the pH scale (Olah et al., 1985). Developed in 1932 by Hammett and Deyrup (Hammett & Deyrup, 1932), H_0 has the scale extended to negative values below zero. On this scale, pure sulfuric acid H_2SO_4 (18.4 M) has a H_0 value of -12.0, hydrogen fluoride (HF) has H_0 of -10.3 (see ***Figure 1.1*** below).

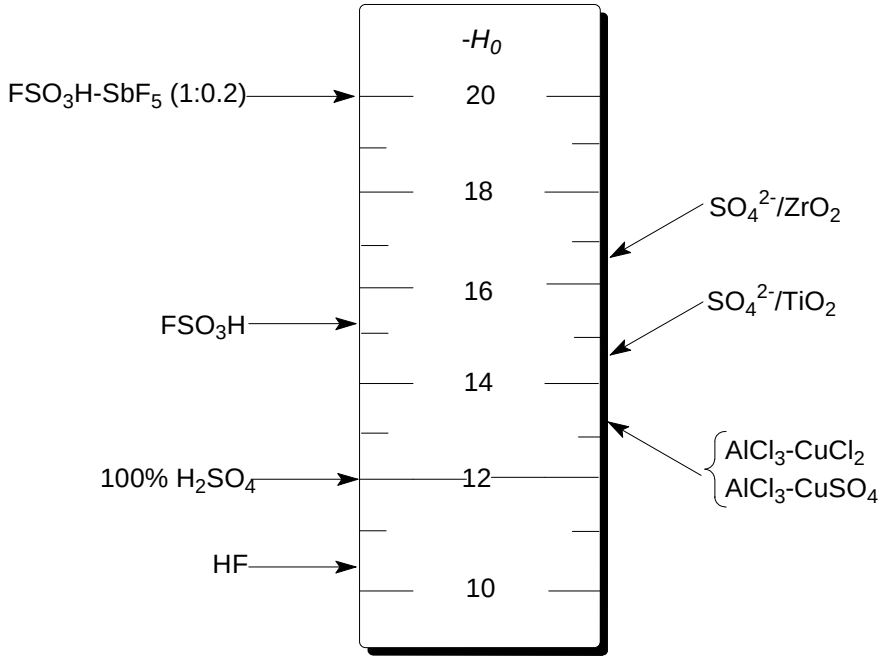

Figure 1.1 *Acid strength of some liquid and solid superacids, redrawn from* (Yadav & Nair, 1999).

Note that the Hammett acidity function clearly avoids water in its system (Olah et al., 1985). By using this acidity measurement without solvent leveling effects between the solvents and solutes are eliminated. It also becomes possible to directly compare the acidities among different pure substances without considering water as solvent.

The Hammett acidity function is applied in the field of physical organic chemistry for the study of acid-catalyzed reactions (Roberts & Russell, 2005).

Defining of superacid Firstly created in 1927 by Conant and Hall (Hall & Conant, 1927), the term ‘superacid’ had been defined as any acid system that is stronger than 100% sulfuric acid (H_2SO_4, 18.4 M), i.e. $H_0 \leq$ -12.0 by Gillespie (Gillespie, Peel, & Gold, 1971). In order to achieve acidities beyond this limit (H_0, -12.0), treatment has to start with an already strong acid (HA, $H_0 \approx 10.0$) and add it to a stronger acid which increases the ionization (Olah et al., 1985).

This can be realized either by dissolving a strong Brönsted acid, HB (e.g. H_2SO_4), capable of ionizing in the medium, B^- (1.3) or by adding a strong Lewis acid, L (e.g. SbF_5) which will shift the autoprotonation equilibrium by forming a more delocalized counterion (LA^-) with the strong acid (1.4) (Olah et al., 1985). And in both cases, a remarkable acidity jump occurs around the H_0 values. ***Figure 1.1*** displays a wide range of superacids Hammett acidity function scale H_0 from -10.2 (HF) to -20.0 (1:0.2 FSO_3H-SbF_5) (Yadav & Nair, 1999). And under some conditions there is even a higher level than -20.0 (Yadav & Nair, 1999).

$$HA \quad HB \rightleftharpoons H_2A \quad B^-;\ \text{e.g. } H_2SO \quad FSO_3H \rightleftharpoons HFSO_3H \quad HSO^- \qquad (1.3)$$

$$2HA \quad L \rightleftharpoons H_2A \quad LA^-;\ \text{e.g. } SbF \quad 2FSO_3H \rightleftharpoons HFSO_3H \quad SbF \quad SO_3F^- \qquad (1.4)$$

Categories of superacids Similar to the conventional acid systems, the superacid system can be divided into Brönsted superacids, Lewis superacids, Brönsted-Lewis superacids and solid superacids. The solid superacids involve liquid acid mounted on suitable carriers, combinations of inorganic salts (e.g. $AlCl_3$-$CuCl_2$, $AlCl_3$-$CuSO_4$), sulfated ion-promoted metal oxides (e.g. SO_4^{2-}/TiO_2, SO_4^{2-}/ZrO_2, SO_4^{2-}/Fe_2O_3), metal-promoted superacids, and zeolite (e.g. ZSM-5) (Yamaguchi, 1990). Some H_0 values for the different types of superacids (from liquid to solid superacids) are displayed in ***Figure 1.1***.

In the following section, discussion will focus on the sulfate ion promoted metal oxides, in particular Brönsted acid sulfate promoted transition metal oxides, their preparation, functionalities in catalysis and active sites natures. In addition, the real existing shortcomings of this kind of solid superacid catalyst which restrict its development will be pointed out, foreshadowing further investigation.

1.1.2 Catalytic properties of sulfate promoted transition metal oxides

Why are transition metals good for catalysis A 'transition metal', also defined as a *d*-block metal, is one which forms one or more stable ions which have incompletely filled *d*-orbitals (McNaught & Wilkinson, 1997). For example, Ti (titanium), $[Ar]3d^1 4s^2$, V (vanadium), [Ar] $3d^3 4s^2$, Mn (manganese), $[Ar]3d^5 4s^2$, Fe (iron), $[Ar]3d^6 4s^2$, etc. They are all typical transition metals lacking the full *d* level ($d < 10$) electron structure.

By the exhibiting a wide range of electronic structures, transition metals appear in a wide range of oxidation states (e.g. iron has +2, +3, and manganese has +2, +3, +4, +6, +7).This is the significant feature different from non-transition metal elements. In the case of iron (Fe), the reasons for the various oxidation states lie in the 4*s* and the 3*d* orbitals having very similar energies. There is no huge jump in the amount of energy when removing the third electron after the two electrons from the 4*s* are lost (see electronic structures **Scheme 1** below). Iron can be easily transformed into its ionic compounds.

	Fe	$[Ar]3d^6 4s^2$	
Scheme 1	Fe^{2+}	$[Ar]3d^6$	losing $4s^1$, $4s^2$
	Fe^{3+}	$[Ar]3d^5$	losing $4s^1$, $4s^2$, and then $3d^1$

Thus for the catalytic reactions, the rich electron states of transition metal ions can help electron movements of the *d*-orbitals, preventing electrons building up on the

reaction sites, thereby achieving a low energy transition state and sequence accelerating reaction rates (Rao & Raveau, 1995).

Another feature of the transition metals is the surface adsorption of the metal elements(Rao & Raveau, 1995). The surface of transition metals provides a place for adsorbing molecules to participate in the reactions by improving the chances of them being in the right orientation to react. Without the surface adsorption they are just simple random collisions.

According to the reasons above, transition metals and their metal oxides can be considered ideal for the catalytic reactions. Furthermore, through the sulfate ion promoted transition metal oxides, acid strength of the compounds is further enhanced (H_0 > -15.0) for acid catalysis.

Some typical sulfate promoted transition metal oxides that are widely used as superacid catalysts involve sulfated titania (IV) (S-TiO_2) (Mukaida, Ishikawa, Yoneya, Satoh, & Watanabe, 1988), sulfated zirconia (IV) (S-ZrO_2) (Bensitel, Saur, Lavalley, & Mabilon, 1987), sulfated ferric (III) oxides (S-Fe_2O_3) (Magnacca et al., 2003), sulfated vanadium (V) pentoxide (S-V_2O_5) (Dunn et al., 1998), and sulfated chrome (III) oxides (S-Cr_2O_3) (S. Wang, Murata, Hayakawa, Hamakawa, & Suzuki, 1999) , etc.

Preparation of sulfate promoted metal oxides catalysts Preparation of the various sulfated metal oxides depends very much on the nature of the precursor materials. Some of the variables are the precipitating agents for forming sol-gel solutions, the types of sulfating agents, the impregnation methods, and the calcination temperatures (Olah et al., 1985). By exposing freshly prepared $Ti(OH)_4$ to 1 M sulfuric acid followed by calcination in air at 773 K for 3 hr, Hino and Arata (M. Hino & Arata, 1979b) firstly obtained the solid catalyst S-TiO_2 which is active for the isomerization of butane and isobutane in high yield at room temperature. Acid strength of the

synthesized solid superacids catalyst was indicated as $H_0 \geq$ -14.5. Subsequently, also by Hino and Arata (M. Hino & Arata, 1980b), $Zr(OH)_4$ was exposed to 1 M sulfuric acid and calcined in air at 873 K, the catalyst obtained was able to isomerize butane at room temperature with H_0 of -13.75. The acid strength was evaluated by a color change method using Hammett indicators (M. Hino & Arata, 1980b).

Regardless of various preparation methods, three characteristics of these kinds of sulfate promoted metal oxides have been widely recognized (Olah et al., 1985; Yadav & Nair, 1999). These are the larger specific surface area, improved acidity, and the ability to maintain acidity after high temperature calcinations (773 to 873 K). Moreover, they are easy to regenerate and reutilize.

Catalytic performance Catalytic performance of the sulfated metal oxide superacid catalysts can be assessed using a number of organic reactions. These reactions are mainly the conversion of saturated (aromatic) hydrocarbons, like alkylation of aromatic hydrocarbons, acylation of aromatics, carboxylation, formylation, and polymerization (Olah et al., 1985). The initial key step in these reactions is the formation of the intermediate carbocations which involves alkane isomerization, cracking and alkylation (Olah et al., 1985).

Hino et al. proved SO_4^{2-}/Fe_2O_3, SO_4^{2-}/TiO_2, and SO_4^{2-}/ZrO_2 catalysts were the active catalysts for the butane isomerization to isobutane reaction (M. Hino & Arata, 1979a, 1979b, 1980b; Makoto Hino, Kobayashi, & Arata, 1979).

The mechanism for the hydrocarbon isomerization under superacid condition is driven by the alkane protonation (Olah et al., 1985). With acid catalyst provides H^+, C–H bonds occur protolysis on the alkane which is evidenced by the formation of minor amounts of hydrogen. Then the ionization step takes place through protolysis in the formation of *iso*-butane ion. In excess of superacids, the ion structure is remarkably stabilized (see **Scheme 2**).

Scheme 2

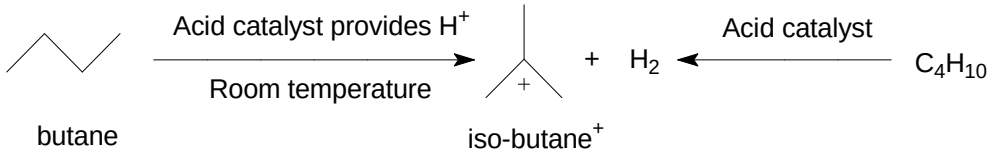

Friedel-Crafts acetylation of aromatics is an aromatic electrophilic substitution reaction. The overall transformation involves the displacement of an aryl hydrogen atom with an acyl moiety derived from the corresponding acyl halide (chloride) by the production of an alkyl aryl ketone (Paragen, 2008). Superacid coordinates as acid catalyst plays the role in converting the acyl chloride into the acylium cation (Barwell, 2002). The coordination activates the chloride ion and then results the acylium cation (**Scheme 3**, 1). The acylium cation is then electrophilic enough to undergo the ions replacement (**Scheme 3**, 2):

Scheme 3

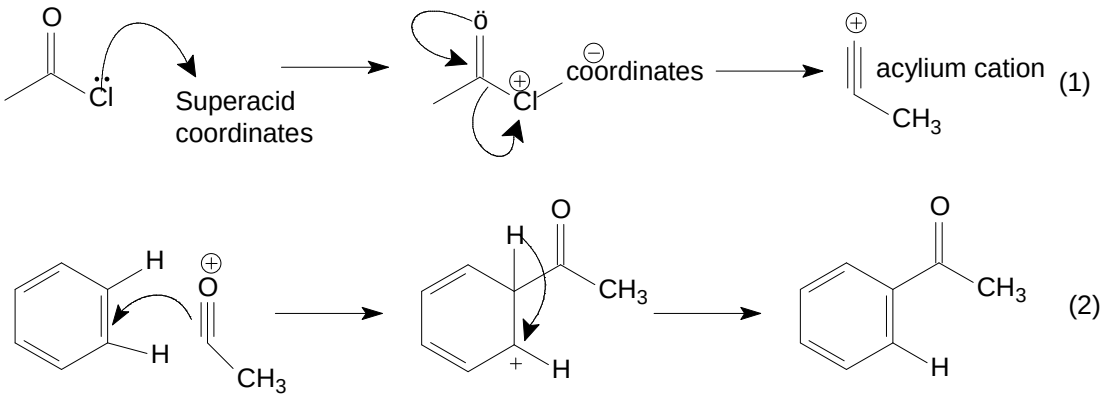

In the work by Arata and Hino (M. Hino & Arata, 1980a), sulfate ion treated iron oxides catalyzing polymerization of ethyl and methyl vinyl ethers lead to high yields of poly methyl vinyl ethers. These showed high degrees of crystallinity.

The key step in the cationic polymerization of alkenes is the formation of a carbocationic intermediate (see **Scheme 4**), which can then start propagation by

reactions and with excess monomer (Olah et al., 1985). Cationic polymerization of alkenes can be initiated by stable alkyl or acyl cations (E^+) (Olah et al., 1985) under acid catalysts promoting the forward reaction.

Scheme 4

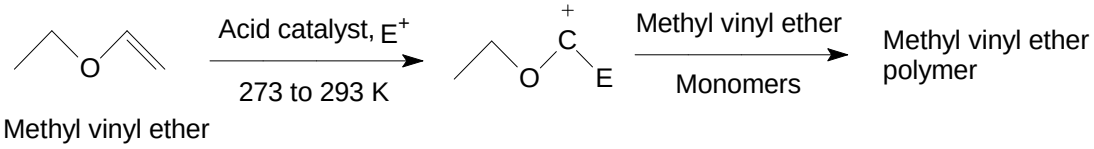

Nature of active sites The remarkable catalytic activities of the solid superacid anion promoted transition metal oxides are largely attributed to their strong acidities as superacids. The strong acidities of these various sulfated metal oxide superacids depend on the number, ratio, types (Lewis/Brönsted) and structures of the active sites (Busca, 2006; Corma, Fornes, Juan-Rajadell, & Nieto, 1994; Sohn & Jang, 1992; Yadav & Nair, 1999; Yamaguchi, 1990).

These characteristics can be investigated by using a range of techniques including IR spectroscopy, temperature programmed desorption, etc. Previous research in this area was mostly focus on sulfated zirconia which is used to represent a wider range of sulfate promoted metal oxides. **Scheme 5** displays the basic structure of S-ZrO_2 with covalent S=O bonds proposed by Kumbha et al. (Yadav & Nair, 1999).

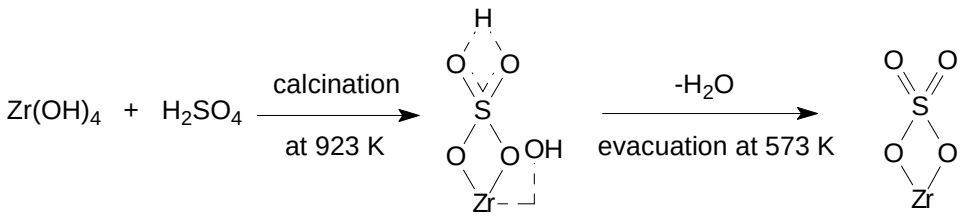

Scheme 5 Redrawn model proposed by Kumbhar et al. (Yadav & Nair, 1999).

The first possible mechanism for the generation of sulfated zirconia active sites was

proposed by Chen et al. (F. R. Chen, Coudurier, Joly, & Vedrine, 1993; Yadav & Nair, 1999). This mechanism suggested a two-step chemical reaction between the superficial hydroxyl groups of zirconium hydroxide and the adsorbed sulfate anions (H_2SO_4) in the formation of S-ZrO_2 acid sites. The first chemical reaction occurs during the impregnation with sulfate sources and the subsequent drying (1.5):

$$Zr\text{–}OH + H_2SO_4 \rightarrow Zr\text{–}O_2\text{–}SO_2 + 2\,H_2O \quad (1.5)$$

And the second step involves the calcination of the catalyst at temperatures above 673 K (1.6):

$$Zr\text{–}O_2\text{–}SO_2 \rightarrow ZrO_2 + SO_2 + H_2O \quad (1.6)$$

The presence of the sulfate anions may explain the sintering resistance, the stabilization of the tetragonal phase, the higher surface area, and the smaller crystal size (F. R. Chen et al., 1993; Yadav & Nair, 1999). Accordingly, the incorporation of the sulfate anions on the ZrO_2 surface was thought to increase the number and strength of the Lewis acid sites (Yadav & Nair, 1999).

Yamaguchi proposed another possible scheme for the formation of sulfated metal oxide active sites (Yadav & Nair, 1999; Yamaguchi, 1990). **Scheme 6** represents the production and structure of active sites by sulfur promotion. Here formation of the structure II from structure I was shown for the case of ammonium sulfate. Other sulfur sources similarly form structure II. Thus, whatever the starting sulfur materials are, once they are oxidized at the metal oxide surface, they all form structure II. It has been further mentioned that such structures are thought to develop at defects, edges or corners of the metal oxide surface (Yamaguchi, 1990). This kind of phenomenon can be explained as the ‘coordinative unsaturation’ of metal oxides (Yamaguchi, 1990).

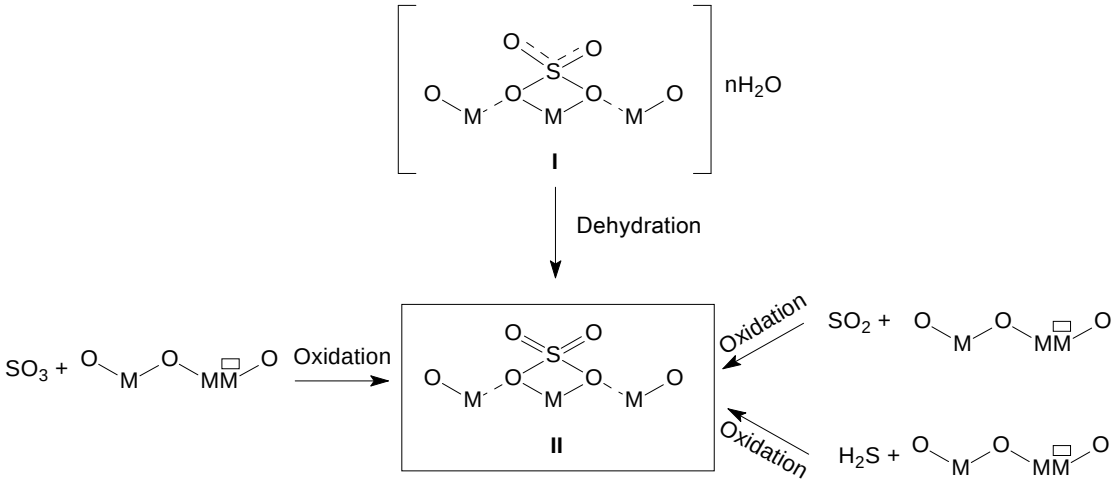

Scheme 6 Redrawn model proposed by Yamaguchi (Yamaguchi, 1990).

The characteristic of structure II is the presence of two covalent S=O bonds. This structure has been proved to be essential for the acid-catalyzed reactions (Yamaguchi, 1990). In the effects of hydration on the ZrO_2/SO_4^{2-} catalyst system, Morterra et al. pointed out that surface sulfates exhibit a highly covalent character through dehydration (which is also demonstrated by a large shift in the IR band for S=O from 1330 to 1370 cm^{-1} after pyridine adsorption). These surface sulfates are associated with strong Lewis acid sites in electron adsorption (Morterra, Cerrato, Pinna, Signoretto, & Strukul, 1994); While, through partial rehydration, water acts as a weak Lewis base and catalyst surface sulfates gradually convert into a less covalent form and then into an ionic form which leads to a decrease in Lewis acid sites and an increase of Brönsted acid sites. This explains the gradually extinguished catalytic activity (Morterra et al., 1994). Covalent sulfated structure II therefore has a strong ability to accept electrons from a basic molecule. This is responsible for the superacid site generation.

Davis et al. explained changes of structure and valence of sulfate species with decomposition at high temperatures (above 923 K) during catalyst preparation (Davis, Keogh, & Srinivasan, 1994). They suggested a different scheme which is able to explain losses of surface sulfates as SO_3 at high calcination temperatures (see **Scheme**

7). This acid site structure contains both Brönsted and Lewis acid sites, as well as the two covalent S=O bonds. When heated to high temperatures, the sulfur is lost from the dried material.

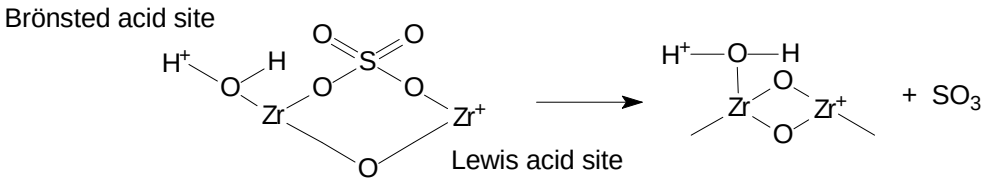

Scheme 7 Redrawn model proposed by Davis et al. (Davis et al., 1994).

However, the scheme proposed above by Davis et al. is incapable of explaining the loss of sulfates as SO_2 as this involves the reduction of S^{6+} to S^{4+} with a corresponding oxidation of some Zr or O species (Davis et al., 1994).

The model proposed by Clearfield et al. (see **Scheme 8**) took into consideration the formation of Brönsted acid sites along with the Lewis sites for the active site structure. The Brönsted sites have higher acidity (Clearfield, Serrette, & Khazi-Syed, 1994).

Generation of the Brönsted acid site is based on the bisulfate ion (HSO_4^-). Rather than the foregoing adsorption of water molecules, the bisulfate ion is predominate species in sulfuric acid media (Arata & Hino, 1990; Morterra et al., 1994). The generation of the Brönsted sites requires ammonium sulfate used as the sulfating agent (Clearfield et al., 1994). Bisulfate ion can display a Zr–O–Zr bridge of hydrated zirconia as shown in **Scheme 8**. IR spectroscopy has shown that on heating to 573 K, an adjacent hydroxyl (-OH) group can interact with the bisulfate ion to release water. This gives structure II below. This results in the generation of Lewis-type acidity (see **Scheme 8**) (Clearfield et al., 1994).

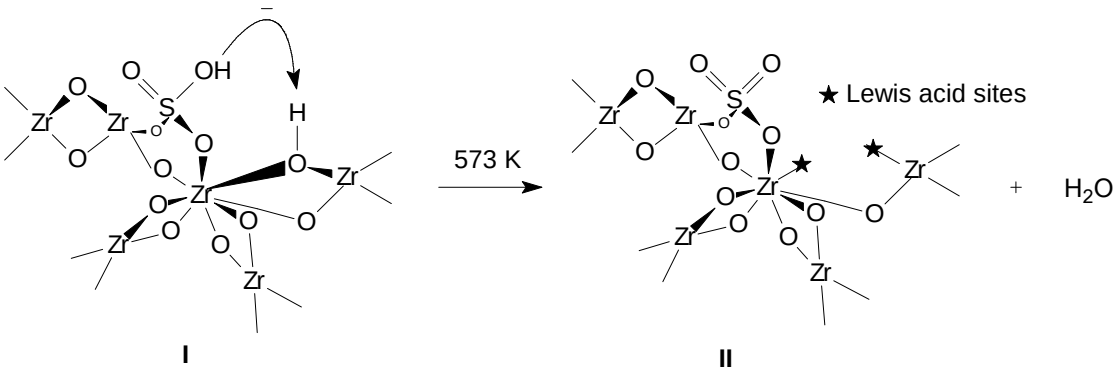

Scheme 8 Redrawn model proposed by Clearfield et al. (Clearfield et al., 1994).

On the other hand, hydroxyl groups can react with an adjacent Zr–OH–Zr bridge to liberate water and leave the bisulfate ion intact (HSO_4^-) (Clearfield et al., 1994). The intactness of the bisulfate ion yields Brönsted sites, and these bisulfate groups acting as Brönsted acid sites account for the strong acidity of the catalyst (Clearfield et al., 1994). Here, the strength of Lewis acid sites is weak because they tend to withdraw electrons from the sulfate group thus weakening the SO–H bonds adjacent to the Lewis acid sites (Clearfield et al., 1994).

Babou et al. postulated a structure for the active sites. The active sites result from the action of the protons (H^+) on the S-ZrO_2 surface. The Lewis acid sites are responsible for more of the active sites (Babou, Coudurier, & Vedrine, 1995).

In the aqueous impregnation solution, H_2SO_4 is totally ionized as a strong acid according to **Scheme 9**:

$$H_2SO \quad \square \quad SO^{2-} \quad 2H \qquad \textbf{(Scheme 9)}$$

The zirconium hydroxide surface traps the protons by the following reaction:

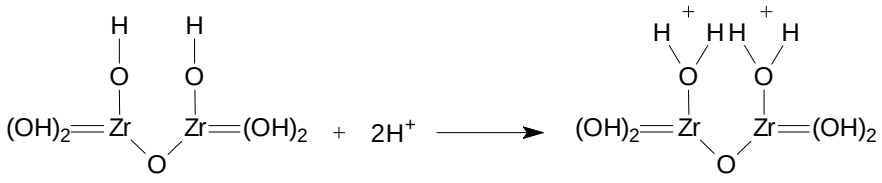

Sulfate ions (SO_4^{2-}) are then trapped onto the ionized surface with the ionization equilibrium shifting to the right hand side:

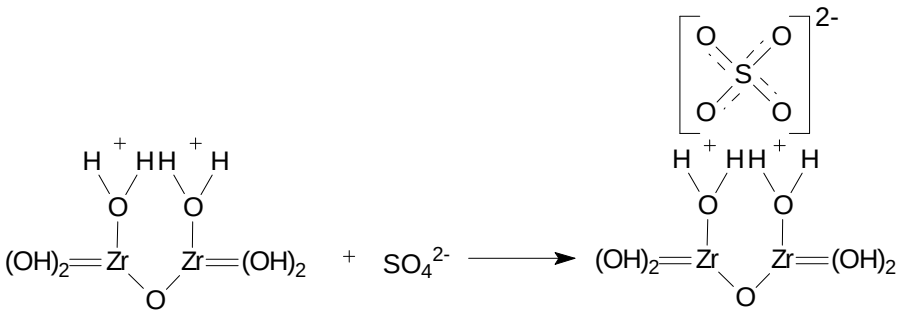

Dehydration at temperatures below 473 K results in the loss of a water molecule from the ionized surface leading to the formation of structure I below:

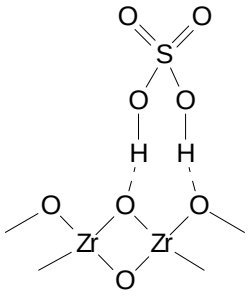

I

Further desorption above 473 K liberates another water molecule with the formation of $(SO_3)_{ads}$ linked by the dative bonds (coordinate bonds), structure II:

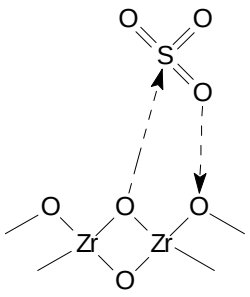

II

By this means, the stability of the structure II is established by the amphoteric characters of the Lewis acid and base sites, SO_3 and ZrO_2 respectively (Babou et al., 1995). The $(SO_3)_{ads}$ species exhibits strong Lewis acid properties (Babou et al., 1995).

1.1.3 Limitation of the sulfated metal oxides in catalysis

Limitations of sulfated metal oxides as catalysts Sulfate promoted transition metal oxides have a significant catalytic activity on a variety of chemical reactions. However, difficulties in increasing the surface area of the metal oxides through conventional preparative methods have largely limited their usefulness as catalysts. This has been pointed out in some recent research publications (C. L. Chen, Li et al., 2001; Lei, Xu, Tang, Hua, & Gao, 2000; Y. Wang, Gan, Whiting, & Lu, 2009; Xia, Hidajat, & Kawi, 2002). The surface area of sulfate treated metal oxides is relative small. For example, sulfate treated zirconia is reported having surface area less than 100 m^2/g (J. H. Wang & Mou, 2008). This significantly restricts the adsorption of the reactants onto the metal surface and consequently diminishes chances for the reactants collision.

1.2 Mesoporous Silica Materials as Catalysts

Based on the nanotechnology, mesoporous silica materials are considered as another kind of catalyst active in the chemical reactions (Giraldo et al., 2007). The prefix

‘meso-’ means a level between ‘macro’ and ‘micro’, meanwhile the suffix ‘porous’ indicates the ‘pore’ structure of this kind of material. Therefore, mesoporous silica is a material on a ‘meso’ scale with a porous surface structure. It can be regarded as a sieve with holes greater than 2 nm and less than 50 nm (Rouquerol et al., 1994). Due to the unique surface structure and their potential active sites, mesoporous silica materials provide the possibilities for a range of catalytic reactions to occur.

In this section of the article, the special pore surface structure will be introduced from its development history, formation mechanism, catalytic active sites, and limitations for its wider applications.

1.2.1 Development history of the mesoporous silica materials

Development history Firstly synthesized in 1989 by the Japanese researchers Yanagisawa et al. (Yanagisawa, Shimizu, Kuroda, & Kato, 1990), the original mesoporous silica presented as a three-dimensional silica networks with micro pores from 2 to 4 nm in diameter and *ca*. 900 m^2g^{-1} for the surface area (Yanagisawa et al., 1990). This can be regarded as the precursor of the mesoporous silica materials. Two years later (1992), a breakthrough in the mesoporous silica material development happened with the synthesis of a higher surface area and adsorption capacity material ‘Mobile Crystalline of Materials’, namely MCM-41 (Kresge, Leonowicz, Roth, Vartuli, & Beck, 1992). Supported on the liquid crystal templates, MCM-41 has the uniform mesopores with size 3 to 10 nm (Kresge et al., 1992). Years later in 1998, another milestone for the mesoporous silica family development was the synthesis of SBA-15 (Santa Barbara Amorphous type material) by the researchers from the University of California in Santa Barbara (Zhao et al., 1998). The SBA-15 (see ***Figure 1.2*** below) has the highly ordered two-dimensional hexagonal silica copolymer mesophases structure with pore sizes from 4.6 to 30 nm (Zhao et al., 1998).

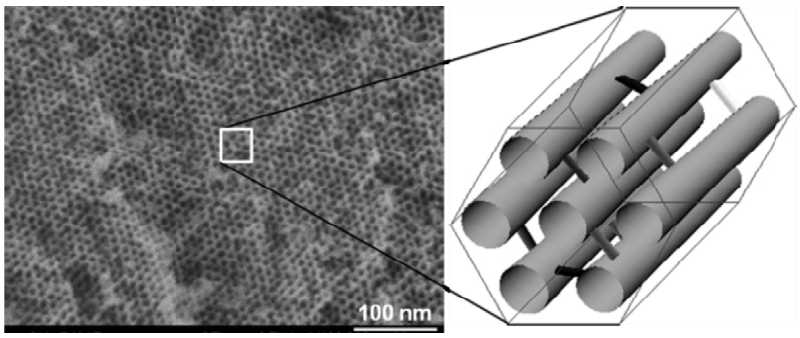

Figure 1.2 *Ordered mesoporous silica (SBA-15 material) with high resolution filed emission SEM image of the pore structure and the hexagonal pore arrangement representation* (Kleitz).

Until now, a wider range of the mesoporous silica nanoparticles such as MCM-X type materials, SBA-X type materials, types MSU-, KSW-, FSM-, etc have been developed with different porous and morphological characteristics for the wide ranges of applications.

1.2.2 Catalytic properties of mesoporous silica material

Pore structure formation Preparation of the MCM-41 materials takes place under mild conditions (below 393 K) in the presence of anionic, cationic, gemini or neutral surfactants, under either basic or acidic conditions (Giraldo et al., 2007). The final calcination process is essential in removing the impurities and stabilizing the hexagonal pore structure.

The formation of the pore structure in mesoporous silica materials follows the liquid-crystal templating mechanism proposed by A. Sayari. This involves a three-step process illustrated below (Sayari, 1996).

Precursor solutions are combinations of silica sources such as sodium silicate, tetraethylorthosilicate (TEOS), tetramethylortosilicate (TMOS), etc with templating

solutions. The first step, driven by electrostatic interaction, is the formation of ion pairs between polycharged inorganic species on the one hand and the surfactant on the other (**Scheme 10** step A):

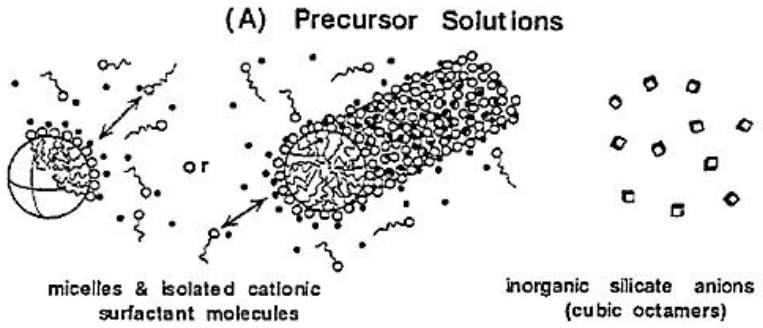

Through ion exchange, the ion pairs then self-organize into a mesophase with a liquid-crystal structure (step B). The structure of the mesophase depends on the composition of the mixture, the pH and the temperature.

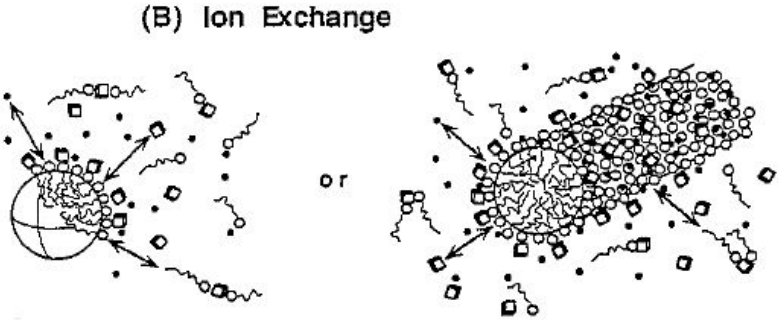

The last step is the condensation of the inorganic species leading to a rigid structure (step C) (Sayari, 1996).

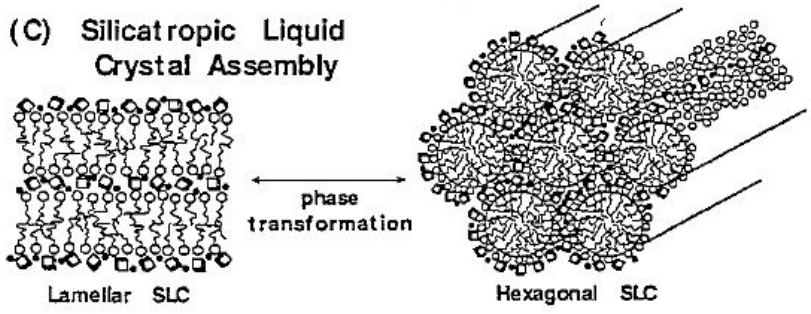

Active sites Mesoporous silica catalytic activities for large molecules (Zhao et al., 1998), heterogeneous reactions (Giraldo et al., 2007) are exhibited not only when they act as independent catalysts, but also when they incorporate metal or metal compounds such as aluminum (Giraldo et al., 2007).

As independent catalysts with high surface area and large pore volume, mesoporous silica provides reactant molecules adequate diffusion room through the catalyst pores. These pores allow the direct interaction with acidic sites on the material wall surface. The generation of active acid site depends on single and geminal silanol group structures on the surface wall behaving as Brönsted acid sites (see ***Figure 1.3***) (Giraldo et al., 2007). However, the acid strength of the Brönsted acid sites is weak due to the neutrality of silica molecules.

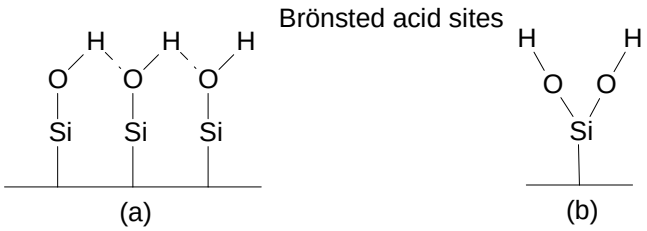

Figure 1.3 *Schematic representation of (a) geminal and (b) silanol groups exist on the surface of mesoporous silica* (Giraldo et al., 2007).

With the incorporation of a trivalent metal such as aluminum into the lattice during mesoporous silica synthesis or by post-synthesis grafting, Giraldo et al. pointed out the increasing number of Brönsted acid sites with the tetrahedral substitution of aluminum in the mesoporous structure (Giraldo et al., 2007). The presence of tri-coordinated aluminum species in the framework gives weak Lewis acid sites. ***Figure 1.4*** shows the Brönsted acid sites and the Lewis acid sites generated on the two structures.

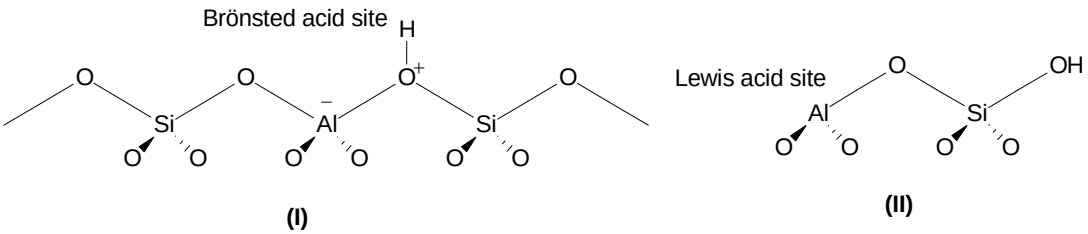

Figure 1.4 *Representation of Brönsted and Lewis acid sites in mesoporous silica generated by structure (I) tetra- and (II) tri-coordinated aluminum* (Giraldo et al., 2007).

From this it can be seen that the weak acid strength of mesoporous silica materials as an independent catalyst without the incorporated metal ions mean that its catalytic activity is limited.

1.3 Sulfated Metal Oxides Supported on Mesoporous Silica

1.3.1 Advantages for the combination

Effectiveness of the composites The combination of sulfate promoted metal oxide with mesoporous silica sieves gives catalysts the advantages of both starting materials These two materials exhibit desirable loading, large surface area, uniform pore size, and adequate pore volumes. Thus, they provide an ideal platform for the solid state (crystalline) metal oxides dispersion. This results in further developing the strong acidities of this kind of solid superacid catalyst, especially in applications for reactions containing bulky molecules (Y. Wang et al., 2009).

1.3.2 Synthesis methods

Composite synthesis In order to incorporate metal ions into mesoporous silica materials, methods for the composite synthesis can be direct physical mixture or

chemical impregnation method. For direct physical mixing it will lead to weak Brönsted and Lewis acidity, low surface acidities, low conversion rates, and activities. On the other hand, various chemical impregnation methods can make up for these disadvantages in achieving different composite properties and catalytic activities (C. L. Chen, Cheng, Lin, Wong, & Mou, 2001; C. L. Chen, Li et al., 2001; Y. Wang et al., 2009; Xia et al., 2002).

Here, three different impregnation methods for metal oxides onto the mesoporous silica sieve surface will be introduced. They are chemical liquid deposition of zirconium sulfate, the one-step incipient wetness impregnation method of zirconium sulfate and the direct impregnation of titanium sulfate. A discussion of their loading abilities and catalytic activities will be compared to obtain the optimum strategy for the further research.

Chemical liquid deposition Chemical liquid deposition method is the method occurring under liquid conditions in forming the solid composites. Reported by Xia et al. (Xia et al., 2002) in a fluoride medium, $Zr(OH)_4$ was first prepared through $Zr(OPr^n)_4$ hydrolysis, MCM-41 powder was then dispersed into the zirconium solution. Solid decomposition was obtained after the mixture was evaporated, and further dry and calcined to form $Zr(OH)_4$/MCM-41 (Xia et al., 2002).

By this method, SO_4^{2-}/ZrO_2/MCM-41 shows uniformity of mesoporous structure, strong Brönsted and Lewis acidities, and high catalytic activities for gas-phase methyl tertiary butyl ether synthesis (Xia et al., 2002). However, this method seems unable to achieve zirconia loadings higher than 26.7% (Xia et al., 2002).

One-step incipient wetness impregnation method For the one-step incipient wetness impregnation method, metal precursor $Zr(SO_4)_2$ was dissolve in methanol solution. The synthesized catalyst support (hollow tubular siliceous MCM-41) was then added with the mixture and zirconium sulfate was coated onto the mesoporous silica pores

by capillary action. The final S-Zr/MCM-41 was obtained through further drying and calcination (C. L. Chen, Cheng et al., 2001).

S-Zr/MCM-41 synthesized by this method has strong acid sites generated by the well-dispersed sulfated zirconia. However, S-Zr/MCM-41 gave very low catalytic activity in the *n*-butane isomerization which was explained by the many sulfated ZrO_2 crystals trapped inside the small pores of silica gel (C. L. Chen, Cheng et al., 2001).

Direct impregnation There are problems in maintaining the crystalline structure of MCM-41 when higher loading of metal oxides were introduced under high acidity condition. In an endeavor to solve this problem, a novel direct impregnation method was applied by Wang et al. in the S-TiO_2/MCM-41 synthesis (Y. Wang et al., 2009).

Here, titania sulfate was directly impregnated onto the as-synthesized silicate composite instead of impregnating them onto a calcined MCM-41 material. The ion exchange process was efficient enough to induce a large amount of impregnation while the mesostructure was intact. With this technique, problems of pores filling up leading to blockages can be avoided as the surfactant still almost fills the channels during the impregnation-dispersion process. Moreover, high titania loadings (higher than 50%) were achieved due to the as-synthesized process of MCM-41 (Y. Wang et al., 2009).

1.3.3 Past work and current gap

Past work Past work has been completed by Wang et al. (Y. Wang et al., 2009) in synthesizing the S-TiO_2 supported on MCM-41 catalyst by using the direct impregnation method. In Wang's work, this new approach was successful, giving high titania sulfate loading without the serious blockage of the pore structure on MCM-41, and it showed strong catalytic activities in the esterification of acetic acid and *n*-butanol.

Current gaps Few studies have been carried out on other sulfate promoted transition metal oxides supported on mesoporous silica materials by the direct impregnation method. There is a wide range of potential catalyst composites by this means need to be investigated.

1.4 Research Objective

Objective Based on the work by Wang et al (Y. Wang et al., 2009) on titania sulfate, the aim of the present research is to further develop the direct impregnation method in synthesis the zirconia sulfate and ferric oxides sulfate supported on the MCM-41 structure, and to achieve high (higher than 50 %) metal oxides loading contents for the catalyst composites.

1.5 Experimental Design

The synthesis of mesoporous silica sieves with ranges of sulfate promoted transition metal oxides titania, zirconia and ferric by using direct impregnation method were carried out. Their catalytic activities were evaluated with the acetic acid and *n*-butanol esterification, and the catalyst composites' structure, porosity, and acidity were characterized by various techniques.

Catalysts preparation Tetraethyl orthosilicate (TEOS) was chosen as the silica source and cetyl trimethylammonium bromide (CTAB) in alkali solution as the template solution in forming the MCM-41 like mesopore shapes. Synthesis for the acid catalyst composites by impregnation titania (IV) sulfate, zirconia (IV) sulfate and ferric oxide (III) sulfated are applied onto the as-synthesized surfactant-silicate composites (direct impregnation) with calculated mole compositions and ranges of metal oxides loading

from 40% to 80%. Through precipitation and thermal treatments for these sol-gel mixtures, final synthesized catalysts were in the forms of S-TiO_2/MCM-41, S-ZrO_2/MCM-41 and S-Fe_2O_3/MCM-41.Synthesis of the catalyst composites by direct impregnation method is outlined in flow chart ***Figure 1.5*** below:

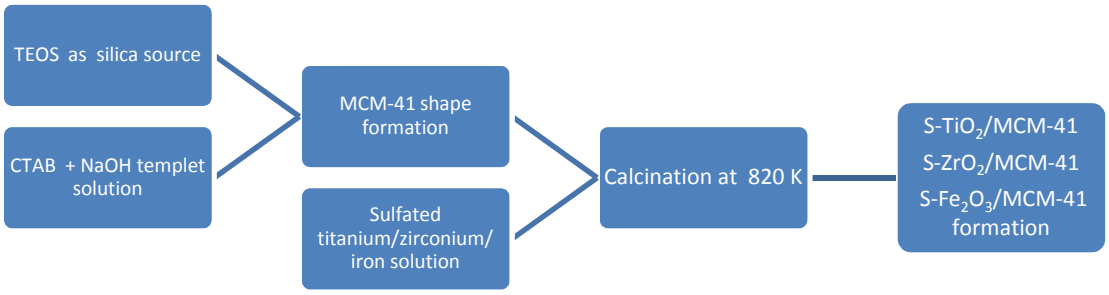

Figure 1.5 *Flow chart of the catalyst composites synthesis by direct impregnation method.*

Catalytic activity evaluation Catalytic activities of the resultant S-TiO_2/MCM-41, S-ZrO_2/MCM-41 and S-Fe_2O_3/MCM-41 catalysts composites were evaluated by carrying out by esterification of acetic acid and *n*-butanol reactions.

Material characterization The synthesized materials were characterized with powder XRD, SEM, nitrogen adsorption for B.E.T. surface area, DRIFT, Hammett indicators, and TGA. Powder X-ray diffraction (XRD) and scanning electron microscope (SEM) was used in determining the physical nature of the phases. The surface areas of the samples were measured by liquid nitrogen adsorption method (B.E.T. surface area). Hammette indicators were used for solid acid catalyst acidity measurement. Diffuse Reflectance Infrared Fourier Transform (DRIFT) spectra of the synthesized samples after adsorbing pyridine were recorded in identifying types of acid sites. Also,

Thermal Gravimetric Analysis (TGA) by the correlation between weight changes and temperature changes was carried out to determine the proper sample preparation temperatures. ***Table 1.1*** lists techniques for the catalysts characterization and information to be obtained.

Table 1.1 *Techniques used for catalyst characterization.*

Technique	Information
Structural and textural characteristics	
SEM	Texture
XRD	Nature of phases
N_2 adsorption isotherm	Surface area and porosity
Acidity measurements	
DRIFT	Types of acid sites
Hammett Indicator	Acid strength
Preparation temperature	
TGA	Weight changes

Data analysis Analyzed date for the different types of catalyst composites with various metal compound loadings were mostly displayed in the form of spectra plots. Thus some information can be interpreted, graphed and listed for further discussion.

Chapter 2 EXPERIMENTAL METHODS

2.1 Chemical Reagents

Silica source Tetraethyl orthosilicate , TEOS, $Si(OC_2H_5)_4$, consists of four ethyl groups attached to an orthosilicate SiO_4^{4-} moiety (see ***Figure 2.1***). It is a colorless liquid with molecular weight 208.33 g/mol. TEOS (CAS No. 78-10-4, Acrōs Organics, 98 %, 250 ml) was used as the silica source in the synthesis of mesoporous silica, MCM-41.

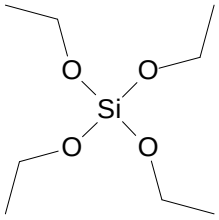

Figure 2.1 *Skeletal formula of tetraethyl orthosilicate, TEOS.*

Template solution Cetyl trimethylammonium bromide, CTAB, $(C_{16}H_{33})N(CH_3)_3Br$ (see ***Figure 2.2***), with the molecular weight 364.45 g mol^{-1}, white powder, as a cationic surfactant in forming and controlling MCM-41 like structure is used for the template solution in the mesoporous silica synthesis (CAS No. 57-09-0, AJAX Chemicals, 95%, 100 g).

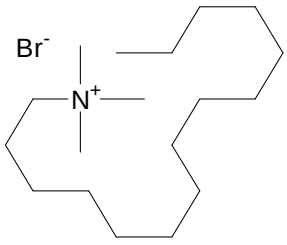

Figure 2.2 *Structure of cetyl trimethylammonium bromide, CTAB. Chain structure of CTAB starts with carbon atom and ends with a nitrogen cation.*

Sulfated metal solutions Sulfated transition metal solutions were prepared by dissolving the calculated amounts of (see section **2.2**) titanium sulfate [$Ti(SO_4)_2$, 240.00 g mol^{-1} mole weight, CAS No. 13693-11-3, Fisher Scientific], zirconium sulfate [$Zr(SO_4)_2$, 283.34 g mol^{-1} mole weight, CAS No. 34806-73-0, Aldrich Chemistry], and ferric sulfate [$Fe_2(SO_4)_3$, 399.86 g mol^{-1} mole weight, CAS No. 10028-22-5,BDH] powders into distilled water.

2.2 Catalysts Synthesis

Synthesized catalysts composites S-TiO_2/MCM-41, S-ZrO_2/MCM-41, and S-Fe_2O_3/MCM-41 were prepared by the direct impregnation method. As-synthesized MCM-41 was impregnated with appropriate amounts of titanium sulfate, zirconium sulfate and iron sulfate solutions. The following method was reported by Wang et al. (Y. Wang et al., 2009).

CTAB powder was dissolved into distilled water with 2 mol L^{-1} NaOH solution and with titanium (IV) sulfate, zirconium (IV) sulfate, and ferric (III) sulfate solutions respectively. Once fully dissolved, the silica source, TEOS was added dropwise into the solution at room temperature with vigorously stirring.

Preparation of the sol-gel mixtures were made up according to the composition (mole ratio) below:

$$\mathrm{CTAB: TEOS: NaOH: H_2O: Ti\ SO_2} \quad 1.0: 3.75: 1.64: 434: \mathrm{TiO_2}\%;$$
$$\mathrm{CTAB: TEOS: NaOH: H_2O: Zr\ SO_2} \quad 1.0: 3.75: 1.64: 434: \mathrm{ZrO_2}\%;$$
$$\mathrm{CTAB: TEOS: NaOH: H_2O: Fe_2\ SO_3} \quad 1.0: 3.75: 1.64: 434: \mathrm{Fe_2O_3}\%.$$

The weight of the TiO_2%, ZrO_2%, and Fe_2O_3% contents were taken to be 80wt%,

70wt%, 60wt%, 50wt% and 40wt% of the total mixture respectively.

For S-TiO_2/MCM-41, for ratios from 80wt% to 40wt%, titanium (Ti) mole amount of titanium sulfate $Ti(SO_4)_2$ to the silicon (Si) mole amount of TEOS should be:

$$80\%\ TiO_2\ \text{content, Ti: Si}\quad 1:1;$$
$$70\%\ TiO_2\ \text{content, Ti: Si}\quad 1:2;$$
$$60\%\ TiO_2\ \text{content, Ti: Si}\quad 1:3;$$
$$50\%\ TiO_2\ \text{content, Ti: Si}\quad 1:4;$$
$$40\%\ TiO_2\ \text{content, Ti: Si}\quad 1:5.$$

Based on the silicon mole percent of TEOS is 13.48wt%, titanium mole percent of titania sulfate is 19.94wt%. Thus, 80wt% TiO_2 loading should be 2.54 of the mole composition for the above gel mixture, 70wt% TiO_2 loading is1.27 mole composition, 60wt% TiO_2 loading is 0.85 mole composition, 50wt% TiO_2 loading is 0.63 mole composition, and 40wt% TiO_2 loading is 0.51 mole composition. That is:

$$\text{CTAB: TEOS: NaOH: } H_2O\text{: 80\% Ti SO}_2\quad 1.0:3.75:1.64:434:2.54;$$
$$\text{CTAB: TEOS: NaOH: } H_2O\text{: 70\% Ti SO}_2\quad 1.0:3.75:1.64:434:1.27;$$
$$\text{CTAB: TEOS: NaOH: } H_2O\text{: 60\% Ti SO}_2\quad 1.0:3.75:1.64:434:0.85;$$
$$\text{CTAB: TEOS: NaOH: } H_2O\text{: 50\% Ti SO}_2\quad 1.0:3.75:1.64:434:0.63;$$
$$\text{CTAB: TEOS: NaOH: } H_2O\text{: 40\% Ti SO}_2\quad 1.0:3.75:1.64:434:0.51.$$

For S-ZrO_2/MCM-41, zirconium mole percent of the zirconia sulfate is 32.20wt%, while silicon mole percent of TEOS is 13.48wt%. Then by the mole composition of CTAB, TEOS, NaOH, H_2O, and $Zr(SO_4)_2$, mole composition of 80wt% ZrO_2 loading is 1.57, 70wt% ZrO_2 loading is 0.78, 60wt% ZrO_2 loading is 0.52, 50wt% ZrO_2 loading is 0.39 and 40wt% ZrO_2 loading is 0.31. That is:

$$\text{CTAB: TEOS: NaOH: } H_2O\text{: 80\% Zr SO}_2\quad 1.0:3.75:1.64:434:1.57;$$

$$\mathrm{CTAB: TEOS: NaOH: H_2O: 70\% Zr\ SO_2}\quad 1.0: 3.75: 1.64: 434: 0.78;$$

$$\mathrm{CTAB: TEOS: NaOH: H_2O: 60\% Zr\ SO_2}\quad 1.0: 3.75: 1.64: 434: 0.52;$$

$$\mathrm{CTAB: TEOS: NaOH: H_2O: 50\% Zr\ SO_2}\quad 1.0: 3.75: 1.64: 434: 0.39;$$

$$\mathrm{CTAB: TEOS: NaOH: H_2O: 40\% Zr\ SO_2}\quad 1.0: 3.75: 1.64: 434: 0.31.$$

And for S-Fe_2O_3/MCM-41, iron mole percent of the ferric oxide sulfate is 13.97wt%, while silicon mole percent of TEOS is 13.48wt%. Then by the mole composition of CTAB, TEOS, NaOH, H_2O, and $Fe_2(SO_4)_3$, mole composition of 80wt% Fe_2O_3 loading is 3.62, 70wt% Fe_2O_3 loading is 1.81, 60wt% Fe_2O_3 loading is 1.21, 50wt% Fe_2O_3 loading is 0.91 and 40wt% Fe_2O_3 loading is 0.72. That is:

$$\mathrm{CTAB: TEOS: NaOH: H_2O: 80\% Fe_2\ SO_3}\quad 1.0: 3.75: 1.64: 434: 3.62;$$

$$\mathrm{CTAB: TEOS: NaOH: H_2O: 70\% Fe_2\ SO_3}\quad 1.0: 3.75: 1.64: 434: 1.81;$$

$$\mathrm{CTAB: TEOS: NaOH: H_2O: 60\% Fe_2\ SO_3}\quad 1.0: 3.75: 1.64: 434: 1.21;$$

$$\mathrm{CTAB: TEOS: NaOH: H_2O: 50\% Fe_2\ SO_3}\quad 1.0: 3.75: 1.64: 434: 0.91;$$

$$\mathrm{CTAB: TEOS: NaOH: H_2O: 40\% Fe_2\ SO_3}\quad 1.0: 3.75: 1.64: 434: 0.72.$$

The blank control MCM-41 catalyst sample was prepared as the same mole composition without the addition of metal sulfates.

pH values of these sol-gel mixtures were maintained at 10.2 with 30% ammonia.

After heating at 373 K for 2 days, the product was washed, filtered, dried at 353 K in the dry oven (Model: Clayson oven, Brendale, Australia) overnight and then calcined at 823 K for 5 hr in the furnace (Model: McGregor, NL 200, Auckland, New Zealand) producing the final catalyst composites MCM-41, S-TiO_2/MCM-41, S-ZrO_2/MCM-41, and S-Fe_2O_3/MCM-41 with different sulfated metal oxides loading contents (see ***Table 2.1***).

Table 2.1 *Classification of catalyst composites with different groups (transition metal*

compounds) and loading contents (from 40wt% to 80wt%).

Group I	a_i	b_i	c_i	d_i	e_i	
S-TiO_2/MCM-41	80wt%	70wt%	60wt%	50wt%	40wt%	
Group II	a_{ii}	b_{ii}	c_{ii}	d_{ii}	e_{ii}	*m:*
S-ZrO_2/MCM-41	80wt%	70wt%	60wt%	50wt%	40wt%	MCM-41
Group III	a_{iii}	b_{iii}	c_{iii}	d_{iii}	e_{iii}	
S-Fe_2O_3/MCM-41	80wt%	70wt%	60wt%	50wt%	40wt%	

2.3 Catalytic Activity Evaluation using Acetic acid and *n*-Butanol Esterification

Evaluation operation Acetic acid and *n*-butanol esterification reactions were carried out in the batch reaction set (see ***Figure 2.3***) which consists with the thermometer, condenser, diverter, and mantle.

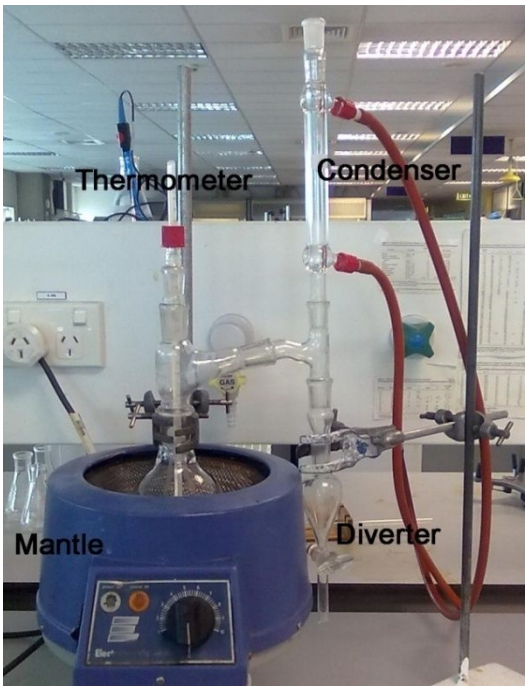

Figure 2.3 *Batch reactor set of acetic acid glacial and n-butanol esterification.*

The glacial acetic acid and *n*-butanol mixture with 1:1.1 v/v (10 ml and 11 ml) was mixed with approximately 0.2 g of each catalyst. Reactions were carried out between 116 to 125^{o}C at atmospheric pressure. The MCM-41 catalyst was run as the control at same reaction conditions.

Qualitative analysis for synthesized esterification products by group I, II, and III catalyst composites were determined through the SHIMADZU 2010 gas chromatography (Kyoto, Japan) with a flame ionization detector (FID) (see ***Figure 2.4***). Instrument parameters were set up as shown in ***Table 2.2***.

Figure 2.4 *SHIMADZU 2010 gas chromatography with FID detector.*

Table 2.2 *Parameters for GC analysis of the synthesized n-butyl acetate.*

GLC	**SHIMADZU GC2010**
Column	ZP-Wax
Column Temperature	50.0^{o}C
Column Flow	0.71 ml/min
Detector	FID
Detector Temperature	200^{o}C
Injection Temperature	250^{o}C
Pressure	59.1 kPa
Total Flow	146.0 ml/min
Retention Time: *n*-butyl acetate	7.08 min

The overall esterification rates of acetic acid and *n*-butanol to butyl acetate were measured by a titration method: 0.500 mol L^{-1} KOH 95% ethanol standard solution was prepared. This was used to titrate with 1 ml mixture of 1:1.1 v/v of acetic acid glacial and *n*-butanol. Phenolphthalein was used as indicator by consuming volume V_0 of KOH standard solution. Same method was used by titrating with the reacted butyl acetate after 4hrs reaction time with volume *V*. The esterification rates were calculated according to equation (2.1):

$$\text{Esterification Rate\%} \quad \frac{V_0 - V}{V_0} \quad 100\% \quad 2.1$$

2.4 Catalyst Characterization Methods

2.4.1 Powder X-ray diffraction (XRD)

XRD operation The powder X-ray diffraction patterns of the three synthesized

catalyst composites groups S-TiO_2/MCM-41 (group I), S-ZrO_2/MCM-41 (group II) S-Fe_2O_3/MCM-41 (group III) and MCM-41 were recorded on the SIEMENS D5000 diffractometer (Madison, WI, U.S.A.) (see ***Figure 2.5***) with CuKα radiation (wavelength λ = 0.15406 nm) at 40 kV and 50 mA. The 2θ angle was regulated between 1.3 ^{o} (min) and 50 ^{o} (max) with a scanning rate of 2 ^{o}/min. X-ray diffraction patterns of the grounded samples were then recorded.

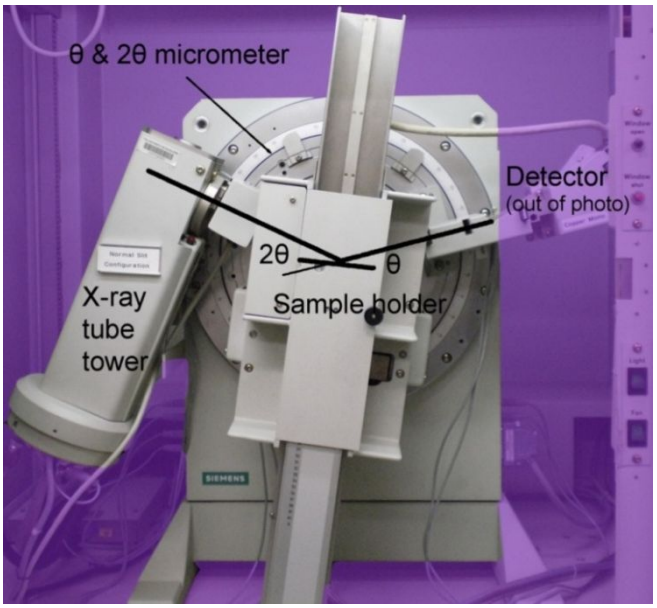

Figure 2.5 *Schematic of the SIEMENS D5000 diffractometer, located in the Science building, the University of Auckland, New Zealand.*

2.4.2 Nitrogen adsorption isotherm method

Surface area and porosity determination Degree of porosity (specific surface area, pore volume, and pore size and its distribution) was analyzed based on the nitrogen adsorption isotherm. The N_2 adsorption-desorption isotherms were obtained by using the TriStar 3000 Micrometitics (Norcross, GA, U.S.A., see ***Figure 2.6***).

Figure 2.6 *TriSTAR 3000 micromeritics with a 2.75 Liter nitrogen dewar along with the degass equipment on the right side.*

Prior to analysis, each sample was outgassed for 2 hr at 523 K. Measurements were taken at 77 K in the liquid nitrogen bath. Adsorbed nitrogen volume under the equilibrated pressure (P) and the saturation pressure (P_0) was recorded for each of the seventeen catalyst samples after average 20hrs' adsorption.

For the specific surface of the group I, II, III and *m* catalyst composites were calculated according to the B.E.T. theory in the range of relative pressure (P/P_0) between 0.05 to 0.25; Pore volume was calculated from the amount of vapour adsorbed at a relative pressure close to the unity (P/P_0 = 0.99) (Lowell & Shields, 1991; Ye, Dong, & Zhang, 2009); And the B.J.H. method was used to obtain the pore size distributions (C. L. Chen, Cheng et al., 2001; Xia et al., 2002).

2.4.3 Scanning electron microscope (SEM)

SEM operation Scanning electron micrographs of group I, II, III and *m* catalyst composites were obtained by the JEOL NeoScope JCM-5000 SEM (Tokyo, Japan).

Catalyst samples were directly mounted into the sample chamber. The system was then vacuumed and micrographs were recorded.

Figure 2.7 *JEOL NeoScope JCM-5000 benchtop scanning electronic microscope.*

2.4.4 Diffuse reflectance infrared fourier transform spectroscopy (DRIFTS)

Pyridine pre-treatment inside the 'in-situ' DRIFT cell Probe molecule pyridine was introduced through the self-built '*in-situ*' DRIFT cell. The equipment is connected with rubber tubing under seal and vacuum condition (see ***Figure 2.8***).

Figure 2.8 *Set-up of the in-situ cell in transporting through the pyridine vapour.*

The analyzed samples were pre-heated at 673 K for 3h before being placed into the cell. The cell was kept dry and free of air. Pyridine vapour was introduced under mild heating for 30 min.

DRIFT equipment operation DRIFT spectra for the catalysts active sites characterization after adsorbing pyridine were recorded on the SHIMADZU IR Prestige-21 Infrared spectrophotometer (Kyoto, Japan) (see ***Figure 2.9***). Spectra were recorded from room temperature to 773 K in the range of 1700 to 1400 cm^{-1}.

Figure 2.9 *SHIMADZU IR Prestige-21 Infrared spectrophotometer.*

In addition, IR absorption for calcined samples were obtained between 4000 to 400 cm^{-1} after annealed at 673 K for 1 hr, samples were diluted with KBr powders.

2.4.5 Hammett indicators for acid strength measurement

Acidity strength measurement Acid strength measurement with the Hammett indicators was referred by J.L. Ropero-Vega et al. (Ropero-Vega, Aldana-Perez, Gomez, & Nino-Gomez, 2010) in the case of sulfated titania and zirconia.

About 0.01 g catalyst sample was suspended in 5 ml benzene overnight. Two indicator drops in benzene solution were then added to the resulting dispersed solution in identifying the acid or basic color (see ***Table 2.3*** and ***Figure 2.10***).

Table 2.3 *Hammett indicators used for acid strength measurement.*

Indicator	pK_a	Acid color	Basic color
Bromothymol blue	+ 7.2	Yellow	Blue
Methyl red	+ 4.8	Red	Yellow
Cresol bromine green	+ 3.8	Yellow	Blue
Thymol blue	+ 1.2	Red	Yellow

Figure 2.10 *Hammett indicators for catalysts acidity strength measurement: methyl red, bromothymol blue, thymol blue, and cresol bromine green (from left to right).*

2.4.6 Thermal gravimetric analysis

Catalyst composites thermal gravimetric analysis was operated by the calcining furnace (Model: McGregor, NL 200, Auckland, New Zealand) from room temperature to 800^{o}C. The synthesized catalyst composites and MCM-41 were analyzed. Sample weights were recorded under various calcinations temperatures by the analytical

balance. Then a series of %weight loss versus temperature change curves were plotted.

Chapter 3 RESULTS AND DISCUSSIONS

3.1 Catalytic Effects on Acetic Acid and *n*-Butanol Esterification

n-Butyl acetate is an organic compound used as solvent in the production of lacquer, fiber, plastic, medicine, as well as food synthetic fruit flavorings. This kind of colorless sweet fruit smelling flammable liquid can be found in fruits such as apple, pineapple, banana, etc. For industrial manufacturing, *n*-butyl acetate is synthesized by the esterification of *n*-butanol and acetic acid catalyzed by sulfuric acid.

However, for the traditional homogeneous sulfuric acid catalyst has become less attractive because of its chemicals are corrosive, hard to recycle and environmental pollution. Thus, there is a trend to develop the solid superacid catalysts as the substitute in the manufacture of *n*-butyl acetate (Cui, Gao, Jin, Zhao, & Dong, 2008; Guan et al., 2010; H. Guo, Chen, & Yan, 2010; Li et al., 2010; Luo, Ren, Zhang, & Qiang, 2009).

3.1.1 Esterification mechanism

Acetic acid and n-butanol esterification *n*-Butanol (BuOH) and acetic acid (HOAc) react to form butyl acetate (BuOAc) as below (3.1):

$$\mathrm{BuOH} \quad \mathrm{HOA} \square \ \mathrm{BuOAc} \quad \mathrm{H_2O} \quad (3.1)$$

This chemical reaction takes place under liquid-phase conditions, with the temperatures range from 310 to 525 K, at 1 atm pressure in the presence of acid catalysts (W. Song, Venimadhavan, Manning, Malone, & Doherty, 1998).

The acid catalysts are normally homogeneous catalysts (e.g. sulfuric acid, sulfo catio exchangers), heteropoly (e.g. zeolites), or heterogeneous catalysts. For the present

study, heterogeneous solid superacid S-TiO_2, S-ZrO_2 and S-Fe_2O_3 supported on MCM-41 catalyst composites' catalytic activities were evaluated by the esterification. The *n*-butanol and acetic acid esterification has been widely used in the catalytic activity evaluations of various solid superacid catalysts (Nagaraju, 1997; W. Song et al., 1998; Timofeeva et al., 2001; Y. Wang et al., 2009; Xia et al., 2002).

Mechanism for the formation of butyl acetate The mechanism for the acetic acid and *n*-butanol esterification with sulfuric acid catalyst follows five steps (Brown, 1995) (**Scheme 11**).

The first step is acetic acid taking a proton from the concentrated sulfuric acid. The proton attaches to the lone pairs of the oxygen double-bonded to the acyl carbon (**Scheme 11**, a):

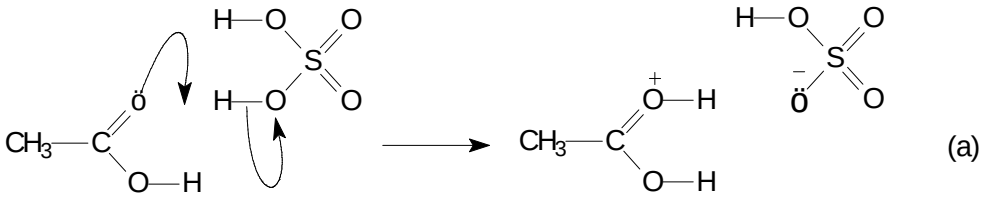

(a)

The positive charge then shifts onto the carbon atom, given the resonance structure below (**Scheme 11**, b):

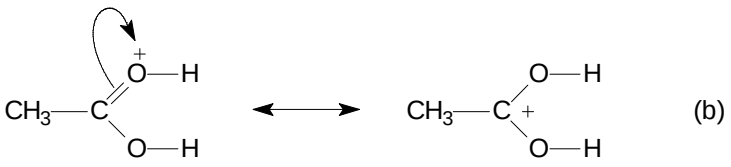

(b)

The second step is the positive charge on the carbon atom attacked by the lone pairs on the oxygen of the *n*-butanol molecule (**Scheme 11**, c):

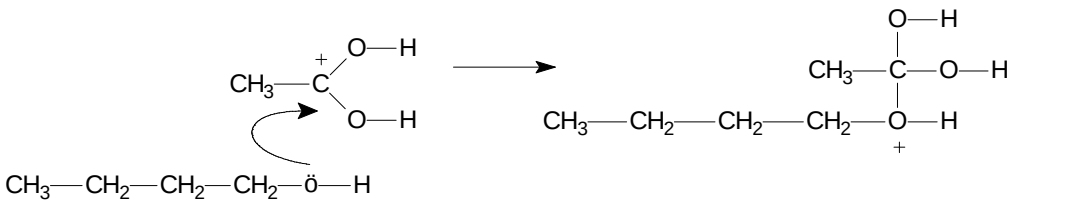

A proton then gets transferred from the bottom oxygen atom to one of the other oxygen atom which makes step three (**Scheme 11**, d):

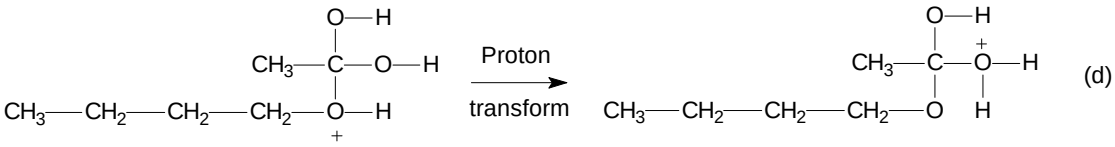

Step four is the water molecule removal from the ion (**Scheme 11**, e):

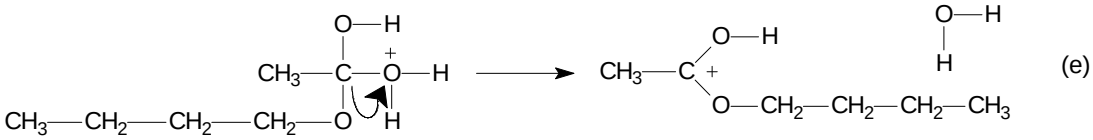

The last step is the hydrogen removal from the oxygen atom by the reaction with the hydrogen sulfuate ion which was formed back in the first step (**Scheme 11**, f):

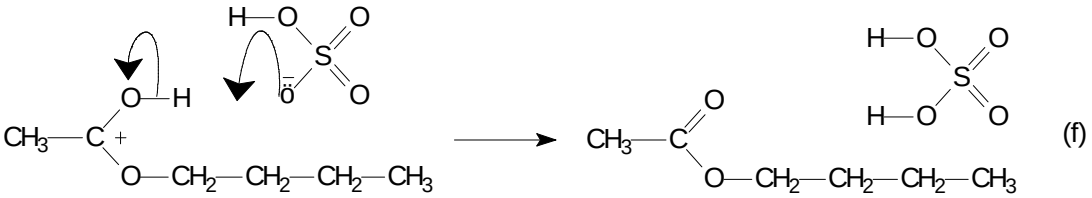

Thus, the butyl acetate has been formed with the acid catalyst being regenerated. In reducing the changes of the reverse reaction occurrence, the reaction is drown forward by distilling *n*-butyl acetate as it is formed.

3.1.2 Determination of the product composition

IR spectroscopy Based on the molecular vibration and infrared radiation absorption, IR spectroscopy is a powerful tool for characterizing functional groups of organic compounds. The FTIR technique was used to measure the adsorption spectra. It applies Fourier transform (a mathematical algorithm) to convert the raw data (interferogram) into the desired result: a plot of transmittance,%T against wavenumber, cm^{-1}. By comparing the IR spectrum with the reference, it enables to identify major structural and component features of certain groups of atoms in a molecular.

Figure 3.1, ***3.2*** and ***3.3*** display the IR spectra in wavenumber (cm^{-1}) of the esterification synthesized product by S-TiO_2/MCM-41, S-ZrO_2/MCM-41, and S-Fe_2O_3/MCM-41 catalyst composites with 70wt% metal compounds loading.

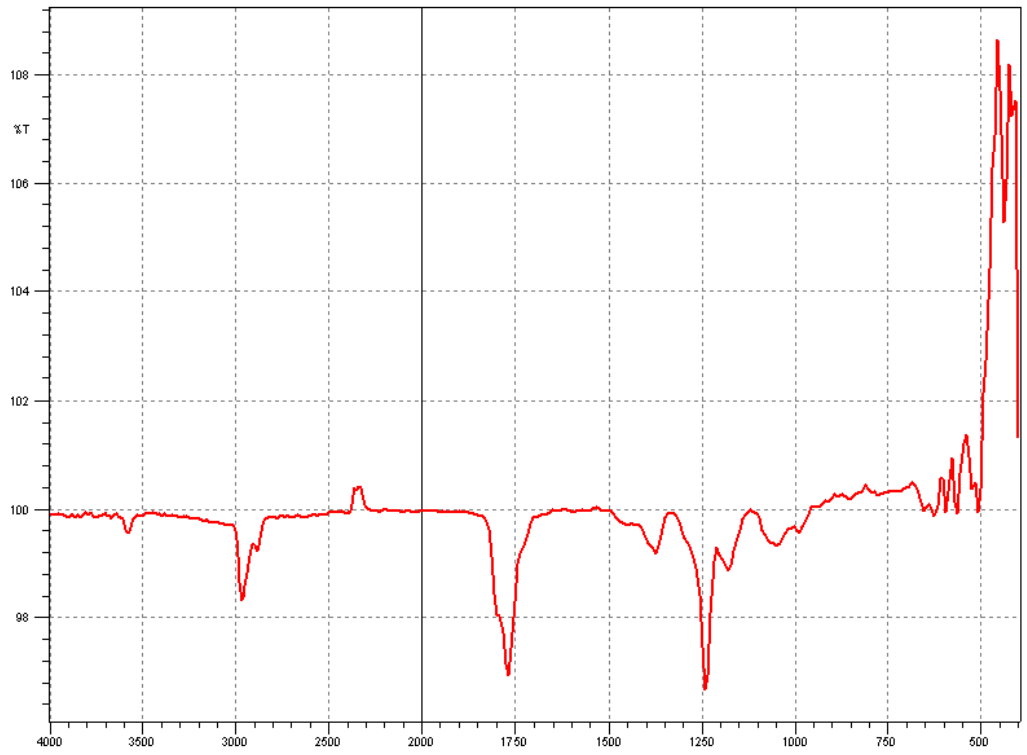

Figure 3.1 *IR spectrum of the synthesized n-butyl acetate by using 70wt% S-TiO_2/MCM-41 catalyst.*

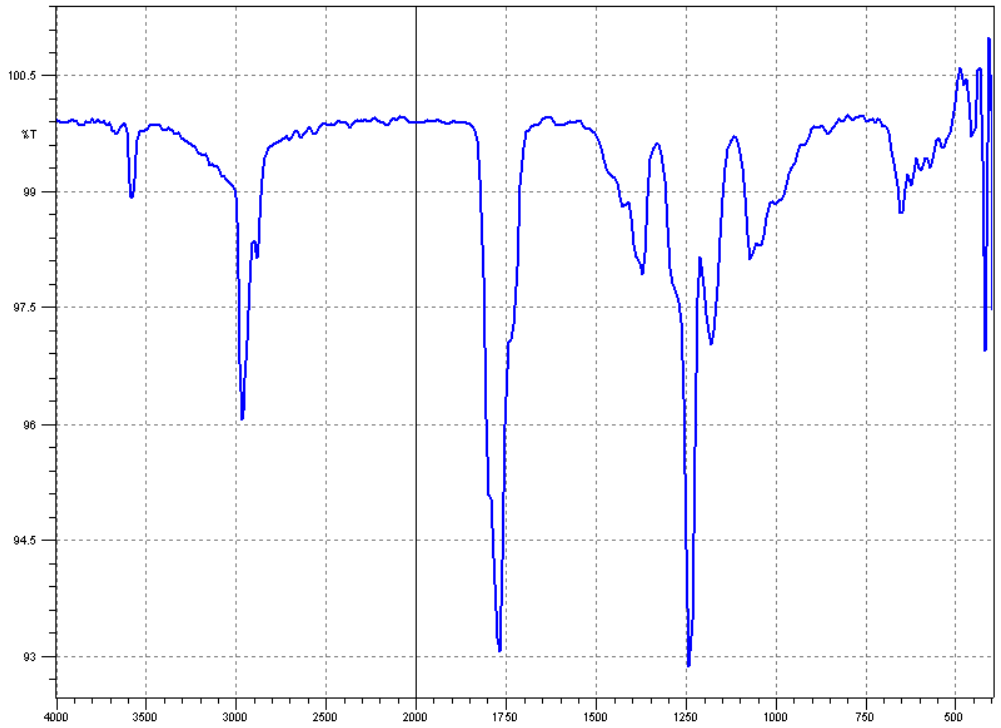

Figure 3.2 *IR spectrum of the synthesized n-butyl acetate by using 70wt% S-ZrO_2/MCM-41 catalyst.*

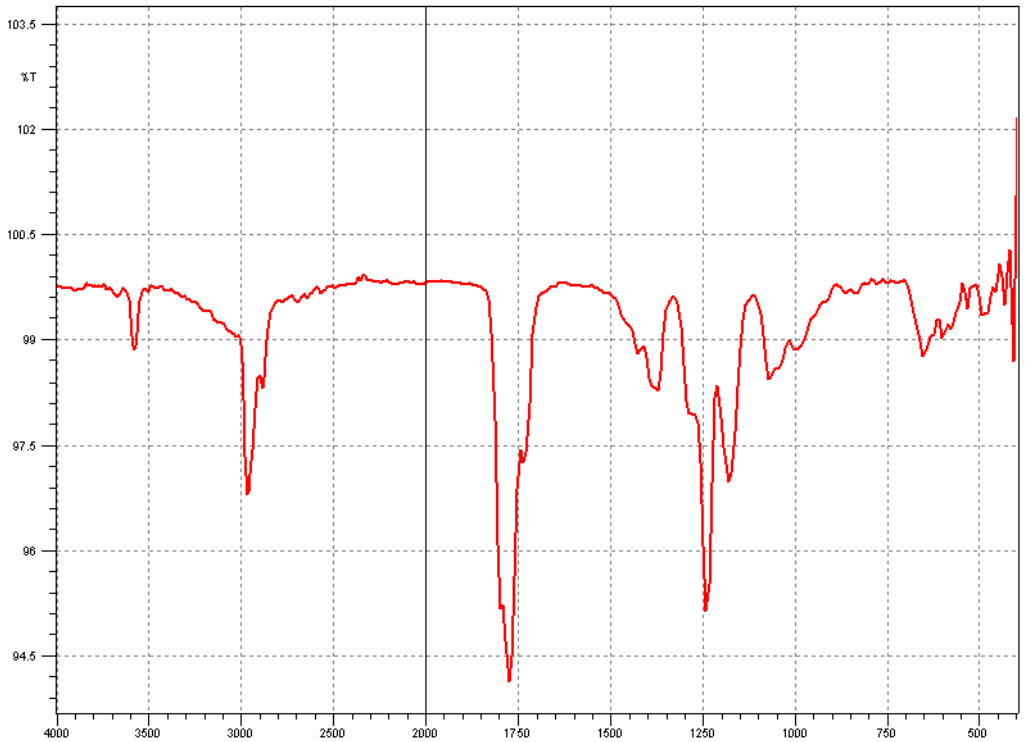

Figure 3.3 *IR spectrum of the synthesized n-butyl acetate by using 70wt% S-Fe_2O_3/MCM-41 catalyst.*

From the downward peaks of chemical bonds IR absorption in ***Figure 3.1***, ***3.3*** and ***3.3***, characteristic peaks near 1750 cm^{-1} imply the saturated ester structure of the product compound. Region from 4000 to 2500 cm^{-1} corresponds to the adsorption caused by C-H bonds which occurs near 3000 cm^{-1}. In the fingerprint portion of the IR spectrum (region below 1500 cm^{-1}), a large number of absorptions occur due to the C-C single-bond vibration (Clayden, 2001; McMurry, 2000). In ***Figure 3.3*** the smaller peak at 1250 cm^{-1} than the peak at 1750 cm^{-1} may indicate the low purity of the synthesized product.

This information is identical with the *n*-butyl acetate IR spectrum compared from the reference spectrum (QASoft Database) which means the synthesized products by group I, II, and III catalysts are mostly *n*-butyl acetate. In addition, there are no characteristic peaks of ether (1070-1150 cm^{-1}), alkenyl (1650 cm^{-1}), or aldehyde (1730 cm^{-1}) groups in the spectra of the synthesized products. This demonstrated the high purity of the esterification synthesized products as well as the high selectivity and specificity of the catalyst composites.

GC qualitative analysis Gas chromatography (GC) is the technique in identifying the mixture components with high degree of certainty (Simpson, 1970). It is the separation of complex volatile mixture by distribution between a gaseous phase and a stationary phase. The sample is run on a suitable column under a fixed set of operating conditions. Thus tentative identifications can be assigned to those components having identical retention times to standards.

Figure 3.4 shows a representative chromatogram of the esterification synthesized product by using c_i catalyst. Similar peak numbers and retention times also appear in other synthesized products via various catalysts in this study. These results are listed

in ***Table 3.1***.

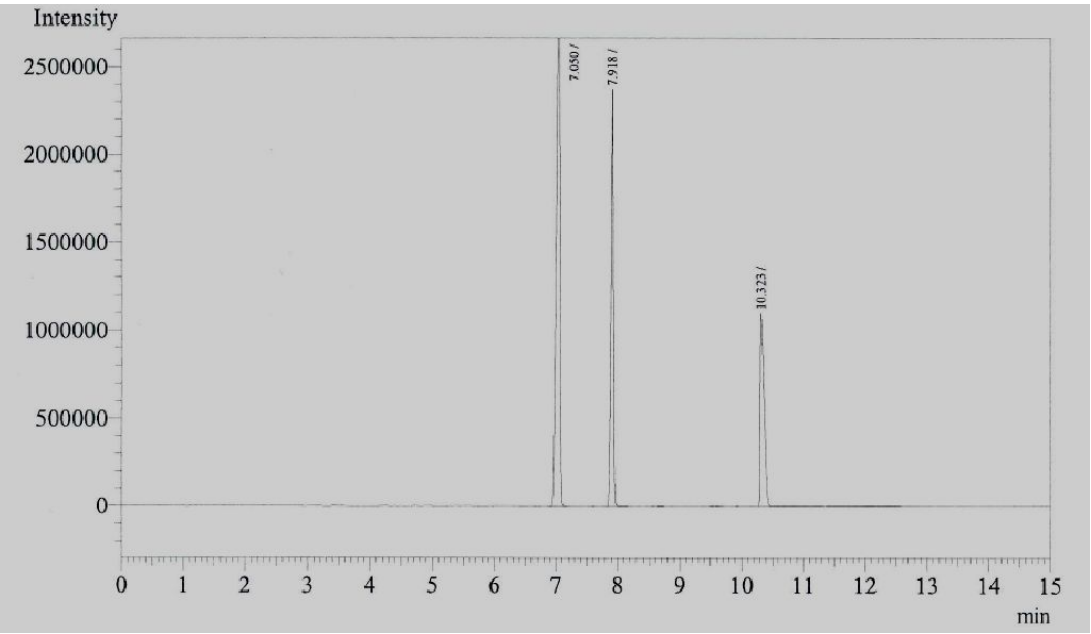

Figure 3.4 *GC chromatogram of the esterification products synthesized product by using* c_i *catalyst.*

The retention times of the peaks in the above GC chromatogram are identical those of known standards. This result further confirms the high selectivity and purity of the three groups of catalyst composites catalyzed products. There are mostly starting materials (*n*-butanol, acetic acid) and final products (*n*-butyl acetate) present in the system throughout the reaction.

Table 3.1 *Peak numbers and retention time of the synthesized product via groups of catalyst composites with different metal compounds loadings.*

	Catalyst	No. of Peaks	Retention Time (min)		
Group I S-TiO_2/MCM-41	a_i, 80wt%	3	7.059	7.939	10.299
	b_i, 70wt%	3	7.053	7.921	10.320
	c_i, 60wt%	3	7.050	7.918	10.323
	d_i, 50wt%	3	7.109	7.965	10.303
	e_i, 40wt%	3	7.041	7.920	10.325
Group II S-ZrO_2/MCM-41	a_{ii}, 80wt%	3	7.086	7.955	10.316
	b_{ii}, 70wt%	3	7.046	7.923	10.329
	c_{ii}, 60wt%	3	7.038	7.914	10.308
	d_{ii}, 50wt%	3	7.088	7.949	10.325
	e_{ii}, 40wt%	3	7.053	7.924	10.328
Group III S-Fe_2O_3/MCM-41	a_{iii}, 80wt%	3	7.049	7.930	10.312
	b_{iii}, 70wt%	3	7.063	7.934	10.304
	c_{iii}, 60wt%	3	6.627	7.670	10.240
	d_{iii}, 50wt%	3	7.075	7.934	10.323
	e_{iii}, 40wt%	3	7.059	7.926	10.326
n-Butyl acetate Std.	N/A	1	7.078	–	–
n-Butanol Std.	N/A	1	–	7.961	–
Acetic acid Std.	N/A	1	–	–	10.321

3.1.3 Esterification rates analysis

Overall comparison of esterification rates The overall esterification rates of *n*-butyl acetate by group I, II, and III catalyst composites with various sulfated metal oxides loading contents are displayed in ***Table 3.2*** and ***Figure 3.5***.

Table 3.2 *Overall esterification rates by group I, II, and III catalyst composites.*

Group I	Esterification rate, %	*Group II*	Esterification rate, %	*Group III*	Esterification rate, %
a_i	90	a_{ii}	96	a_{iii}	79
b_i	80	b_{ii}	94	b_{iii}	77
c_i	74	c_{ii}	88	c_{iii}	76
d_i	70	d_{ii}	86	d_{iii}	68
e_i	67	e_{ii}	73	e_{iii}	58

Compared with the esterification rate 52% by MCM-41, group I, II, and III catalyst composites show their improved yields with the incorporation of metal compounds. This indicates the high catalytic activities for the three sulfated transition metal oxides catalysts act in the reaction. The results show that the catalytic activities increase with the increasing of S-TiO_2, S-ZrO_2, and S-Fe_2O_3 loading. High esterification rates (average: 78.4%) for group I, II, and III catalyst composites demonstrate the strong acidities of the S-TiO_2/MCM-41, S-ZrO_2/MCM-41 and S-Fe_2O_3/MCM-41 prepared by the direct impregnation method. They are mainly attributed to the acid nature (Brönsted and Lewis acid sites) of the catalyst surface. Eesterification rates of the catalyst composites with sulfated ferric oxides (S-Fe_2O_3/MCM-41) appear the lowest among of three groups. And catalyst composites with zirconia sulfate (S-ZrO_2/MCM-41) show the highest catalytic activities for the reactions. Correlations between the catalyst structure natures and their catalytic activities will be found in section **3.3**.

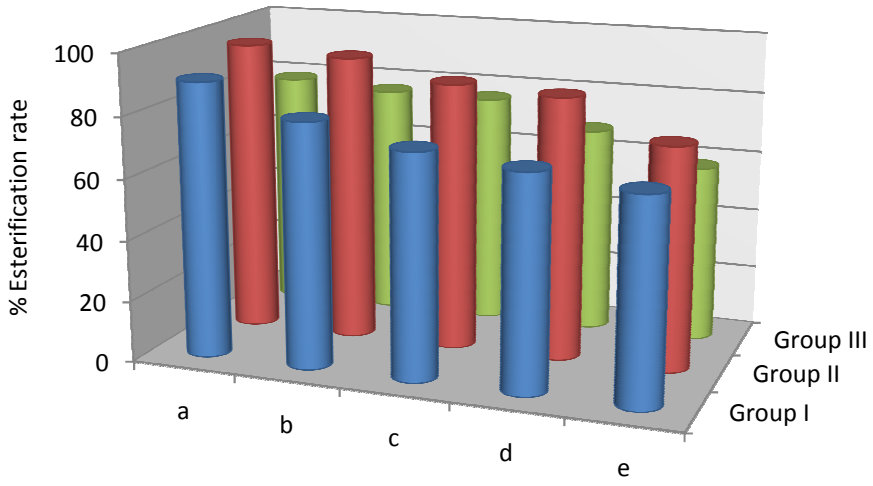

Figure 3.5 *Comparison of n-butyl acetate esterification rates by group I, II, and III catalyst composites catalyzed reactions.*

From ***Figure 3.6*** it can be seen that esterification rates for all the three groups of catalyst composites show a slightly decrease after being used for three times. Gradually decreasing catalytic activities of the three groups of catalyst composites can be attributed to the formation of water in weakening the Brönsted and Lewis acid sites of the catalyst surface. However, the decrease in catalytic activities of the catalyst composites is not drastic which means they are still good for repetitive use.

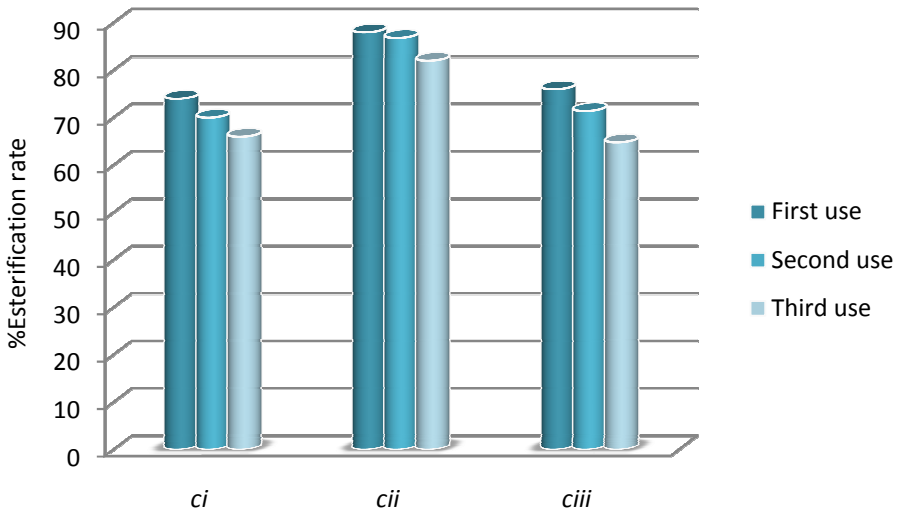

Figure 3.6 *Catalysts repetitive using tests by c_i, c_{ii}, and c_{iii} (80wt% metal compounds loading) catalyst composites.*

Decreasing of esterification rate Calibrated refractive index results in ***Figure 3.7*** indicate the purity of the synthesized *n*-butyl acetate by S-TiO_2/MCM-41s decreased with time on stream (from 1 to 4hr). Similar decrease tendencies of the purity of the synthesized *n*-butyl acetate were also found for S-ZrO_2/MCM-41s and S-Fe_2O_3/MCM-41s with time on stream.

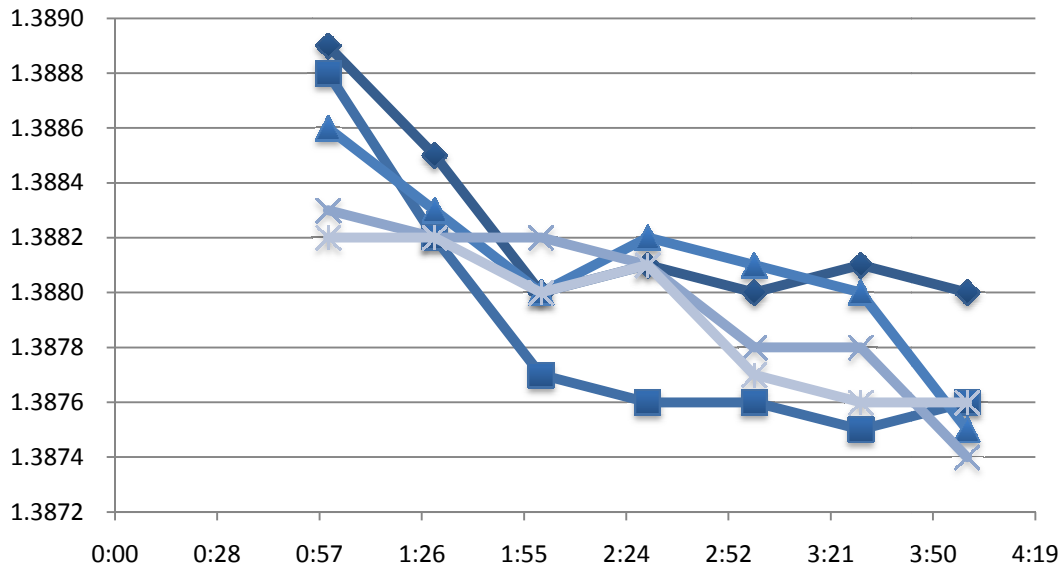

Figure 3.7 *Refractive index (n_D^{20}) of acetic acid and n-butanol esterification versus time on stream (1 to 4hr) by S-TiO_2/MCM-41s.*

The decreased purity of *n*-butyl acetate with 4hr on stream may be attributable to higher acidity of this catalyst resulting in a large amount of coke being deposited during the reaction (Y. Wang et al., 2009) which the reaction was carried under the fixed-bed reactor. Another reasonable explanation of the decreasing esterification rates versus time on stream is related with the formation of H_2O molecules. Some of the water backflow into the reaction system could be absorbed onto the surface acid

sites. Water is highly polar and could reduce the surface acidity. There is a similar problem found in the catalysts repetitive use tests. Such problem might be solved by adding water-carrying agents (e.g. benzene, toluene) in removing water from the reaction system. However, it still remains unclear for the gradually decreased esterification rates in the present reaction set.

3.2 Formation of the Catalysts

3.2.1 MCM-41 structure formation by TEOS and CTAB

TEOS as silica source Reported by Estevao et al. (Estevao Candeias et al., 2002), TEOS as the silica precursor in the MCM-41 structure synthesis is effective in producing and stabilizing highly ordered pore structure. Moreover, free from aluminum and sodium of TEOS avoids interference effects with the Ti^{4+}, Zr^{4+} and Fe^{3+} sulfate ions (Koyano & Tatsumi, 1997).

By adding water at room temperature, TEOS is prone to convert into silicon dioxide (SiO_2) and ethanol as a side product reaction (3.2):

$$Si\ OC_2H \qquad 2H_2O \rightarrow SiO_2 \quad 4C_2H\ OH \quad (3.2)$$

Gaydhanker et al. (Gaydhankar, Samuel, Jha, Kumar, & Joshi, 2007) pointed out that the synthesized silicon dioxide presents in the form of a non-linear network Si-O-Si linkage. This kind of linkage follows the formation of intermediate alkoxy derivatives of silicic acid and polysilicates during TEOS hydrolysis. The addition of surfactant induces the silicate oligomers to exhibit ion exchange activity. In addition, the rate of the TEOS conversion can be accelerated by the presence of base such as sodium hydroxide (Gaydhankar et al., 2007).

CTAB as surfactant Surfactant CTAB performs the role of directing agent to form of a structure with high surface area and uniform pore distribution. Also CTAB helps control the growth of the structure and inhibit agglomeration (Y. Guo et al., 2008; Zhang, Liu, Song, & Guo, 2009).

Adding CTAB with the cationic surfactant can induce a series of ionic changes in the aqueous solution as described by Asim et al. (Asim, Radiman, & Ambar bin yarmo, 2009): interactions of Br^- and $–CH_3–CH_3–CH_3–N^+$ with silicate oligomers induces the transition of micelles to the rod-like shapes. The ionic surface of the ionic micelles is called the Stern layer, while surrounding this ionic mantle is a region containing both counter ions and oriented water molecules as the Gouy-Chapman layer. Together the Stern layer and Gouy-Chapman layer forms the electrical double layer which covers onto the newly formed mesoporous silica particles (Asim et al., 2009).

Mesoporous silica assembled by TEOS and CTAB Formation of the mesoporous silica begins with the mixture of the precursors TEOS and CTAB. That is similar with the ‘three-step’ mechanism proposed by A. Sayari (refer to section ***1.2.2***) (Sayari, 1996),. Immediately after the silica source TEOS is added with the cationic surfactant CTAB at pH higher than 7, ion exchange of silicate oligomers with Br^- and OH^- anions (I in ***Figure 3.8***) form the inorganic-organic self-assembled silicate rod-like micelles (II). Lengths of the silicate rod-like micelles are then controlled according to the catalysis of NaOH. And final step is the silicate rod-like micelles condensation by the electrostatic interactions (III). Here, a more detailed scheme for the MCM-41 shape formation is displayed in ***Figure 3.8***.

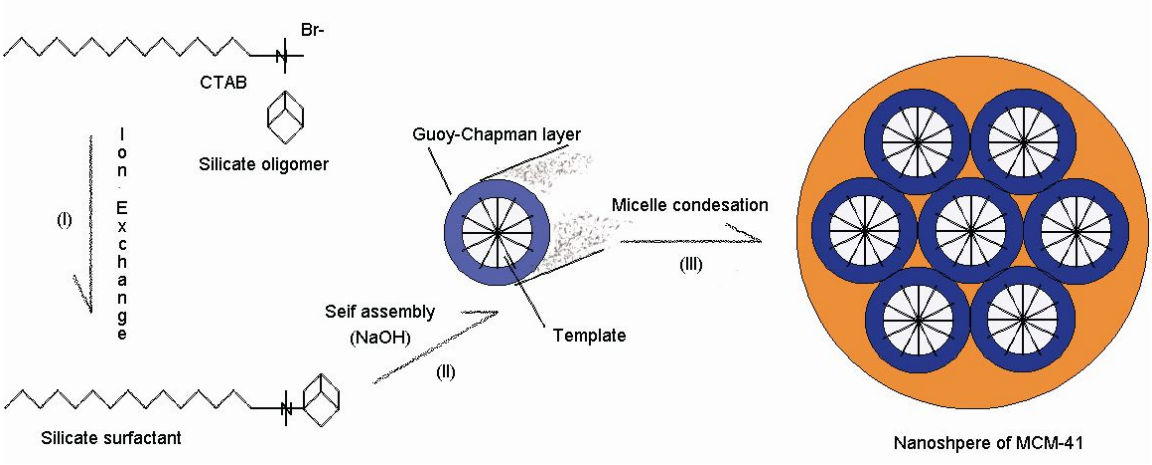

Figure 3.8 *Formation of MCM-41 like shape by precursors TEOS silicate source and CTAB surfactant (templates in the rod structures are then removed under thermal treatments).*

3.2.2 Effects of thermal treatments

Thermal treatments As the groups of solid superacid catalyst composites do not show intrinsic acidities comparable with liquid superacids (Olah et al., 1985). Thermal treatments with high temperatures are necessary to turn their catalytic activities into active forms.

Thermal treatments during the catalyst synthesis involve drying and calcinantion. These generally have their functions in burning off any residual organics (e.g. alcohol, ligands), present in dried inorganic gels, converting metal oxides into active forms, and turn them into the cogelled catalysts (Regalbuto, 2007). Furthermore, both of the two thermal treatments have their specific functions.

Drying The drying step involves a three-stage process consisting of a preheating period, a constant temperature period, and a falling rate period (Regalbuto, 2007). For the preheating period, the rate of liquid vaporization at the support surface increases as the temperature increases. During the constant rate period, vapor is removed from

the support surface. At this stage, temperature of the wet support remains constant which is known as the wet bulb temperature. The falling rate period occurs when the moisture transport inside the support is no longer sufficient to keep the surface saturated. Thus the drying rate decreases and dry patches appear near the surface (see ***Figure 3.9***).

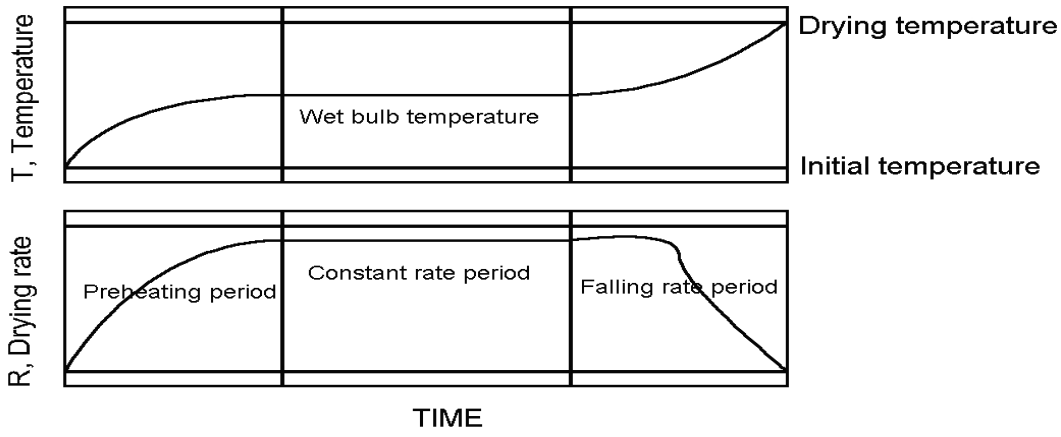

Figure 3.9 *Variation of drying rate and temperature of the wet porous material during drying, redrawn from Regalbuto* (Regalbuto, 2007).

Metal redistribution During the drying stage, the active metal compounds (i.e. Ti^{4+}/SO_4^{2-}, Zr^{4+}/ SO_4^{2-}, and Fe^{3+}/ SO_4^{2-}) are redistributed onto the support surface (Lekhal, Glasser, & Khinast, 2001, 2004; Lekhal, Khinast, & Glasser, 2001).

This metal migration after the impregnation stage can lead to desired or undesired changes to the metal profiles which are determined by several physical and chemical processes (see ***Figure 3.10***). They involve: (1) adsorption of the active metal onto the support, (2) transport of the solvent, (3) transport of various dissolved species in the solvent, (4) heat transport, and (5) mass and heat transfer at the surface of the support particle.

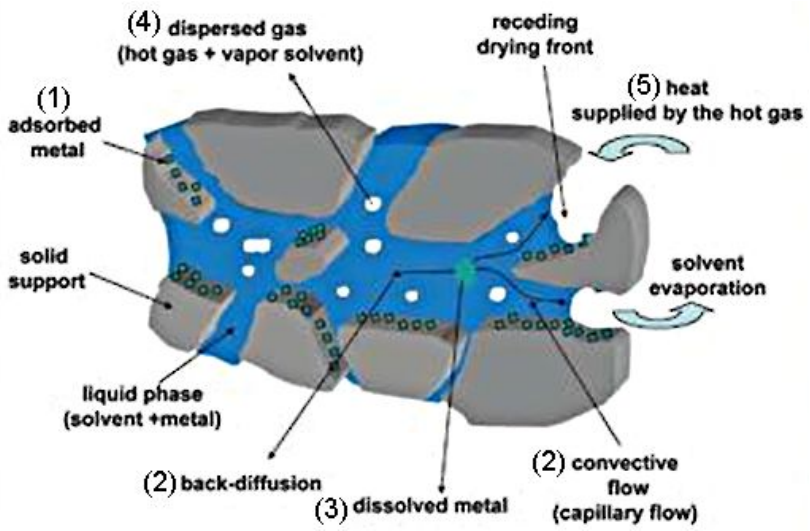

Figure 3.10 *Physical and chemical processes on the catalyst support during the drying stage. Redrawn from Regalbuto* (Regalbuto, 2007).

Calcination Calcination, also known as annealing or thermolysis is to expose the as-prepared catalyst precursors into high temperatures for the final step in converting the crystal phase catalyst.

Here, the calcination process is essential for thoroughly removing the residues that block up the MCM-41 pores. Calcination subsequently acts one of its roles in removing micelle templates within the cylindrical pores and leaving an impurity-free support surface. Another role performed by the calcination process is to provide thermal energy to ‘lock’ the crystalline phase, grain size of the support, surface oxides and control surface density. Thus, the ‘crystals analyzing’ can be carried out for their highly ordered arrangements with the XRD method (Jenkins, 1976).

The calcinations temperatures should be high enough to ensure the complete removal of all organic components but not higher than necessary to avoid sintering of the MCM-41 support and/or of the metal compounds. Through the calcination process, structure and substance changes of MCM-41 and the relevant metal compounds composites can be detected by thermal gravimetric analysis.

3.2.3 Thermal decomposition analysis

TGA for the catalysts characterization As a branch of thermal analysis, the TGA technique examines the mass change of a sample as functions of temperature in a controlled atmosphere (Hatakeyama & Quinn, 1994). Changes of weight form the basis of TG analysis.

For the three groups of the catalyst composites, mass changes are largely related to the decomposition of the space-filling template (i.e. CTAB) and sulfated metal compounds [i.e. $Ti(SO_4)_2$, $Zr(SO_4)_2$, $Fe_2(SO_4)_3$] in their 'as-synthesized' conditions.

Therefore, the TGA study is applied to determine the composition of the catalyst composites and their thermal stabilities of the as-synthesized samples decomposition through the resulting mass-changes versus temperature curves. These provide quantitative information on weight change processes, and enable the stoichiometry of a reaction to be followed directly (Dodd & Tsnge, 1987).

Thermal affects on the catalysts synthesis The TGA profile (taken in air) of $Ti(SO_4)_2$ impregnated on as synthesized MCM-41 is shown in ***Figure 3.11*** (curve a) in comparison to those of as-synthesized MCM-41 (curve c) and of $Ti(SO_4)_2$ (curve b). Curve (c) shows that most of the surfactant in as synthesized MCM-41 was decomposed in the temperature range of 200-300^oC. Curve (b) shows that the decomposition of $Ti(SO_4)_2$ is negligible before 300^oC, but around 350-650^oC most of $Ti(SO_4)_2$ decomposed. Curve (a) (the TG profile of $Ti(SO_4)_2$ impregnated on as-synthesized MCM-41) shows several weight loss steps up to 700^oC. Comparing curve (a) and with curve (c) suggests that the weight loss occurring at temperatures below 300^oC is likely due to the decomposition of surfactant, CTAB.

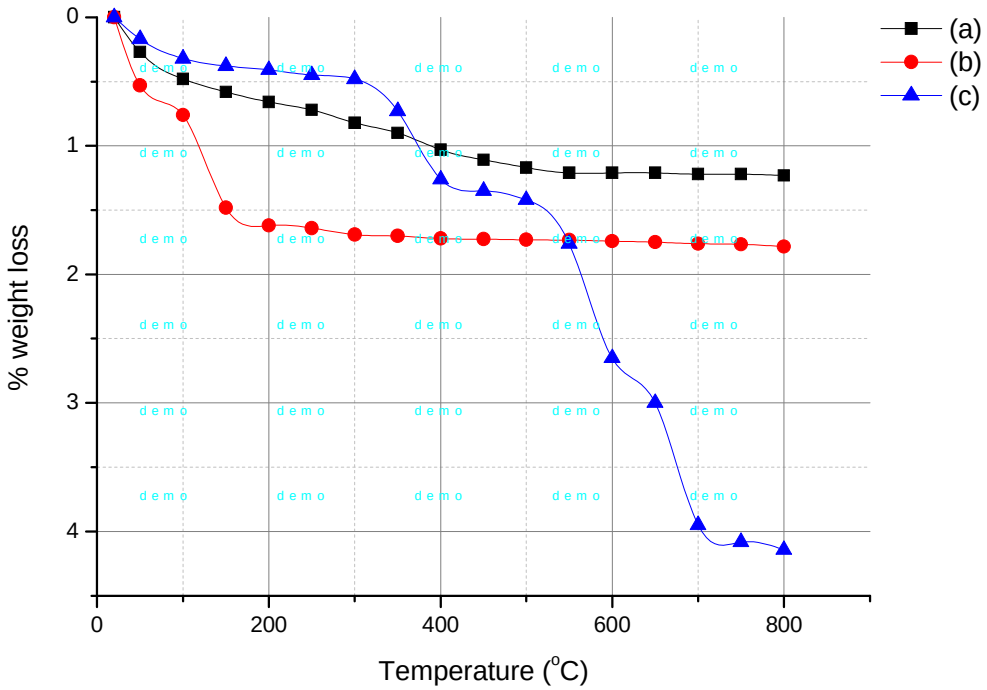

Figure 3.11 *TGA profiles in air of (a) $Ti(SO_4)_2$ impregnated on as-synthesized MCM-41, (b) $Ti(SO_4)_2$, and (c) as-synthesized MCM-41.*

Comparing curve (a) with curve (b) suggests that the weight loss occurring at temperatures above 350°C is attributable to the decomposition of $Ti(SO_4)_2$. In between these two temperatures in curve (a) there is probably a continuous decomposition of surfactant followed by a gradual decomposition of $Ti(SO_4)_2$. The decomposition of surfactant was apparently slower when $Ti(SO_4)_2$ was present. One possible reason for the slower decomposition is that the interaction between surfactant and sulfate is stronger than that between surfactant and silica. Another is that some small $Ti(SO_4)_2$ crystallites may block the pore mouths of MCM-41 so that the surfactant and/or its decomposition products cannot evaporate as easily as from the pristine MCM-41.

The critical decomposition temperature points are similar to the results of Wang et al. (Y. Wang et al., 2009). In addition, decomposition temperatures of zirconia sulfate and

ferric oxide sulfate as their impregnation onto MCM-41 compared with MCM-41 decomposition are found and listed in ***Table 3.3***.

Table 3.3 *Decomposition temperatures of the catalyst composites.*

Sample	Decomposition temperature range of surfactant, CTAB (^oC)	Decomposition temperature range of metal sulfates (^oC)
$Ti(SO_4)_2$ impregnated on MCM-41 (as synthesized)	200-300	350-650
$Zr(SO_4)_2$ impregnated on MCM-41 (as synthesized)	220-310	500-750
$Fe_2(SO_4)_3$ impregnated on MCM-41 (as synthesized)	210-300	300-670

From ***Table 3.3*** we can find that decomposition temperatures of the surfactant, CTAB are all similar on the three as-synthesized catalyst composites, while for their metal sulfates, zirconia sulfate has the highest decomposition temperature range which is probably due to the high stability of the tetragonal polycrystalline structure of zirconia under high temperatures compared to crystallites of titania and ferric oxides.

3.3 Catalysts Struture and Surface Characterization

Catalyst structure and surface characterizations involve catalyst crystallography, morphology, porosity, and surface study. Catalyst crystallography uses powder X-ray diffraction in determining the geometry of the catalyst structure. The porosity and specific surface area are measured by the nitrogen adsorption method to determine the catalysts' unique porous structure and probable capacity for catalysis. From the catalyst morphology, we can see the texture changes with increasing loading of the

sulfated metal compounds via scanning electron microscopy.

Based on the study of MCM-41, results for the catalyst composites were further studied using different types and loadings of sulfated metal oxides to investigate their effectiveness in improving the catalysis.

3.3.1 Catalysts crystallography and morphology

XRD principles Powder X-ray diffraction (XRD) is a technique used to gather information about the structure of powdered crystalline materials through their diffraction patterns. This technique is related to the X-ray analytical method and diffraction phenomenon. Generated with high photon, stable output, and selectable levels of kilovolts source, X-ray incident beams are transmitted onto the atomic plane of a crystalline material. The atomic plane splits the beams which interfere with one another and away from the plane at certain angles and give a pattern of spots. Thus the diffraction interference can be used to obtain information about the structure of crystal powders (Jenkins & Snyder, 1996). ***Figure 3.12*** displays the basic working mechanism of the XRD diffraction.

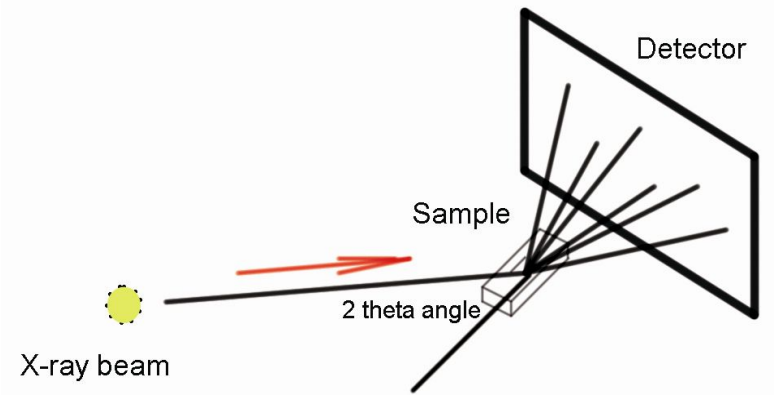

Figure 3.12 *Working mechanism of the X-ray diffraction.*

Developed by the Bragg family (W.H. Bragg and his son L. Bragg) in 1913, the

Bragg's Law explains the phenomena of crystal diffraction in ***Figure 3.13*** (Jenkins & Snyder, 1996):

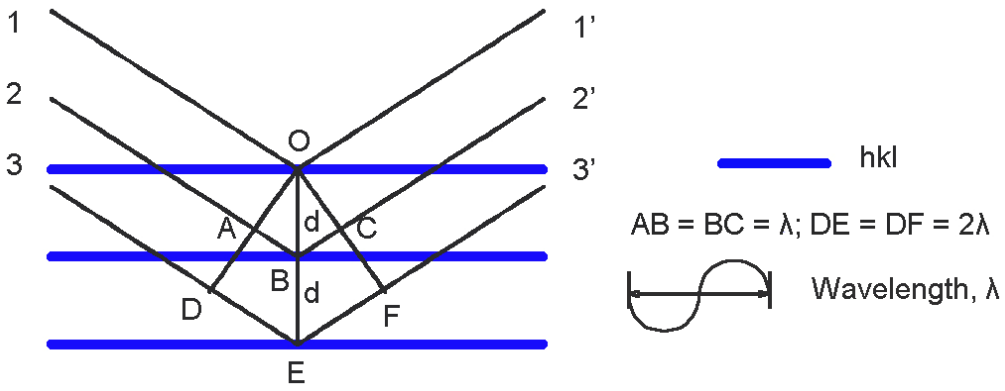

Figure 3.13 *The Bragg's Law X-ray diffraction* (Jenkins & Snyder, 1996).

In ***Figure 3.13***, three crystallographic planes are described with Miller indices (*hkl*). The incident X-ray beams come from the left hand at angle, θ and reflect with the same angle according to the Snell's Law. The wave reflecting from the second plane must travel a distance ABC farther than the wave reflecting from the top one. Similarly conditions for the third plane. Thus, as the distance ABC is exactly equal to one wavelength λ, distance DEF will equal 2λ. Depending on the depth in the crystal, it will produce the constructive interference which is known as the phenomena of diffraction. The distance AB may be obtained by taking the sine of θ:

$$A \qquad \sin$$

When diffraction occurs, wavelength AB=BC=λ. The Bragg's Law results in (3.3):

$$\lambda \quad 2 \quad \sin \quad , \qquad 1,2,3, \ldots \quad (3.3)$$

With billions of tiny and randomly oriented crystallites, X-ray diffraction will only occur at a certain diffraction angle, θ. If the experimental angle was regulated to 2θ, all of the possible diffraction peaks can be produced from the differently oriented crystallites of the powders.

Figure 3.14 shows the X-ray diffraction pattern of *m* (MCM-41) sample.

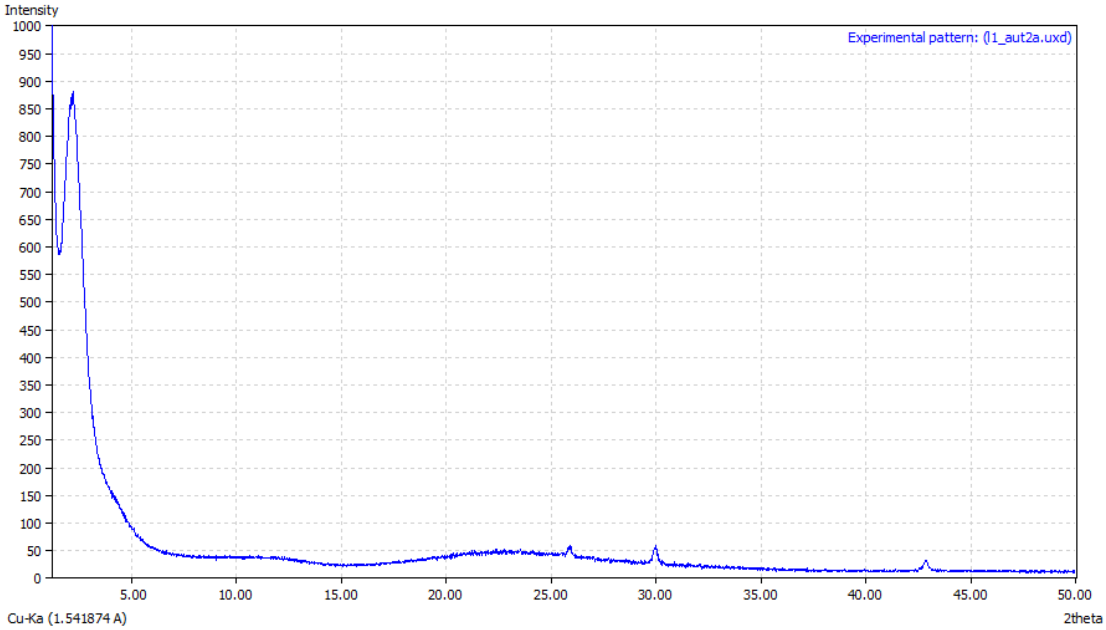

Figure 3.14 *Powder XRD pattern of the MCM-41 catalyst sample obtained after calcinations at 823 K for 5h.*

The MCM-41 silicate displays a sharp diffractions peaks with lattice spacing (interplaner distance) d = 2.88 nm (hkl = 100) at Bragg angle 2.41^{o}. As proved by the researches (Carvalho, Varaldo, Wallau, & Schuchardt, 1997; C. L. Chen, Li et al., 2001; Giraldo et al., 2007; Kresge et al., 1992; Sayari, 1996; Y. Wang et al., 2009). This diffractogram exhibits the characteristic reflections of the highly ordered hexagonal crystal mesostructure (***Figure 3.15*** *left*) of MCM-41. This structure belongs to the *p6mm* space group which still maintained after high temperature calcination (***Figure 3.15*** *right*).

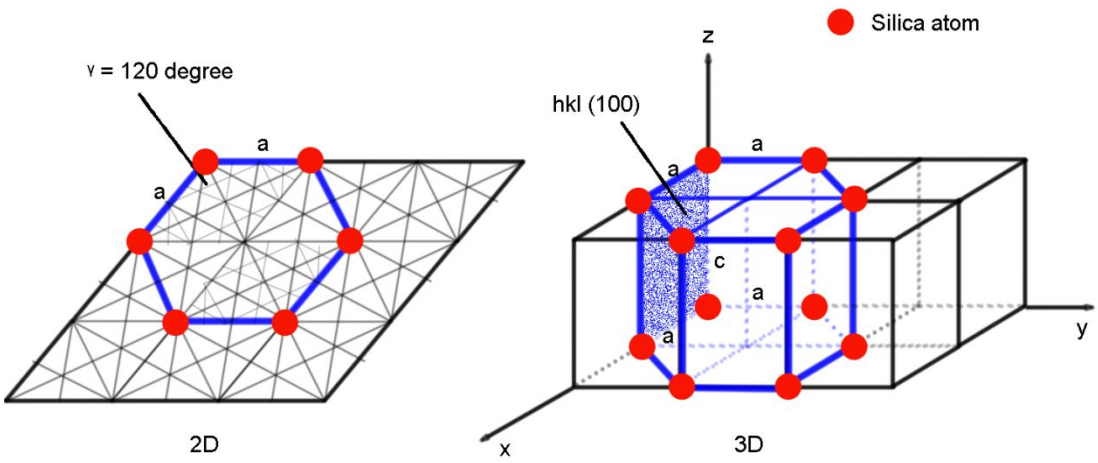

Figure 3.15 *Geometrical description of 2D (left), built by infinite repeating unit cells and 3D (right), repeating unit cells develop in horizontal dimension hexagonal structure of MCM-41.*

In addition, according to the Scherrer equation (3.4),

$$D \quad \frac{K\lambda}{\beta \cos \theta} \qquad 3.4$$

where K is the shape factor, λ is the X-ray wavelength, β is the line broadening at half the maximum intensity (FWHM) in radians, and θ is the Bragg angle.

Mean particle size of the MCM-41 particle is 6.14 μm according to the calculation. This result agrees with the SEM micrographs of MCM-41 in ***Figure 3.16*** which also displays the prism structure of MCM-41.

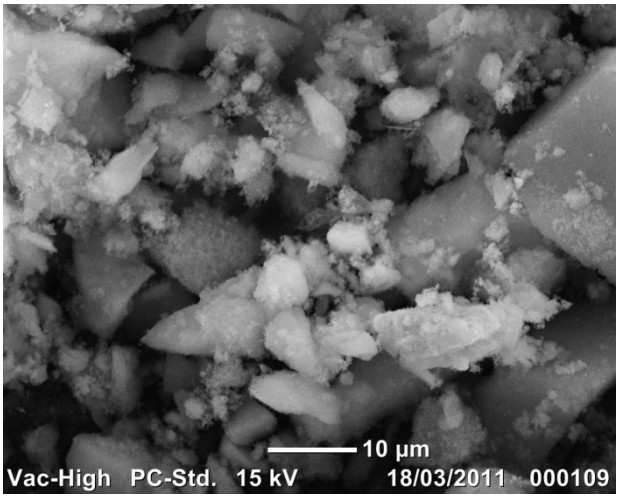

Figure 3.16 *Scanning electron micrographs of the MCM-41 sample after 550 ^{o}C calcination on 10µm scale.*

Scanning electron microscope Scanning electron microscope (SEM) is a type of electron microscope that images a sample by scanning with a high energy beam of electrons in a raster scan pattern. The electrons interact with the atoms that make up the sample producing signals which contains information about the sample's surface topography, composition and other information. SEM is used to study the surface morphology of the catalyst samples. We can directly 'read' information from the photos.

S-TiO_2/MCM-41

From the S-TiO_2/MCM-41 SEM micrographs in ***Figure 3.17***, it can be found that both catalyst composites with 40wt% and 80wt% sulfated titania loadings shows the prism crystal structure. This indicates that for the S-TiO_2/MCM-41 catalyst composites with metal loading up to 80wt%, the prism crystal structure can still be maintained. The increased mean particle size from 40wt% to 80wt% loading samples is related with the increased amounts of metal compound agglomeration with the MCM-41 structure.

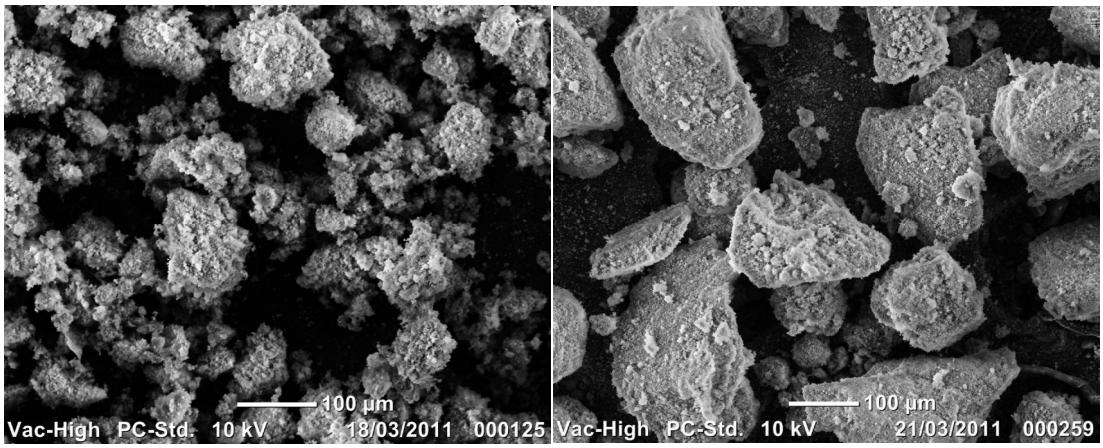

Figure 3.17 *Scanning electron micrographs at 100 nm scale of S-TiO_2/MCM-41 catalyst composites after calcination. Left: catalyst composite with 80wt% titania sulfate loading; Right: catalyst composite with 40wt% titania sulfate loading.*

S-ZrO_2/MCM-41

Figure 3.18 is the XRD patterns of ranges of S-ZrO_2/MCM-41 catalyst composites from 40wt% to 80wt% metal compounds loading. Comparing with the XRD pattern of MCM-41, XRD patterns of S-ZrO_2/MCM-41s show shift of bands from 23 to 27^o which indicates S-ZrO_2 was dispersed onto the surface of the MCM-41 sieve (Bevy, 2005).

Also according to the research by Y. Wang et al. on sulfated titania (Y. Wang et al., 2009), peaks in the high angle region (20 to 30^o) correspond to a ZrO_2 phase. These peaks appeared when the samples were heated at 550^{o}C for 5hr. This suggests that the sulfated zirconia has been decomposed to give SO_x and ZrO_2. However, for the catalyst composite with 80wt% zirconia sulfate loading, there is a broadening of the peak at 25^o compared with other samples. This may imply a structural change of the MCM-41 shape with 80wt% zirconia sulfate loading.

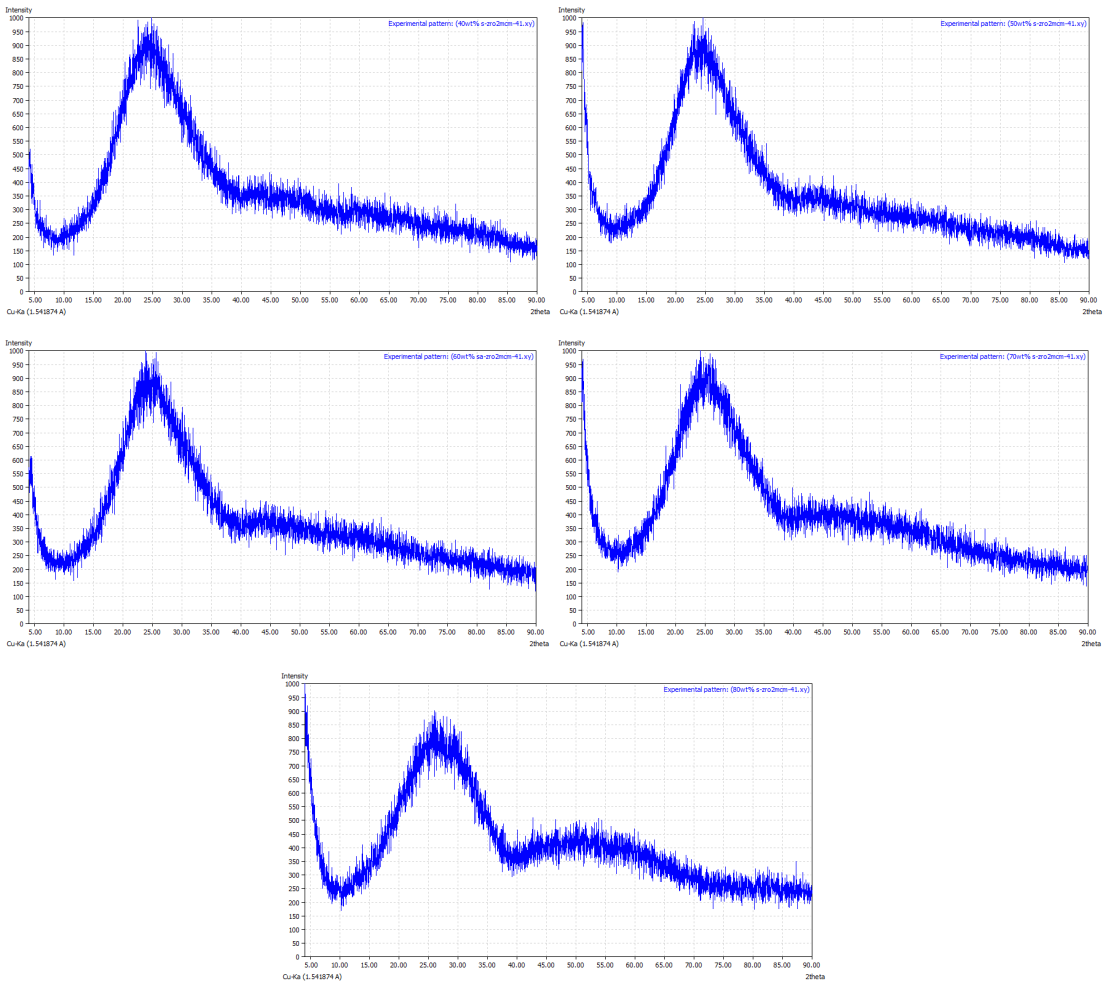

Figure 3.18 *XRD patterns of the S-ZrO_2/MCM-41 composites with different (40wt% to 80wt%, from left to right, up to down) S-ZrO_2 contents calcined at 550 ^oC for 5hr in air.*

From ***Figure 3.19*** the S-ZrO_2/MCM-41 SEM micrographs, it can be found that the 40wt% loading sample maintain the prism crystal structure while the 80wt% loading sample lost the prism crystal structure. This suggests the loss of long range ordering of the S-ZrO_2/MCM-41 sample when the metal compound loading reached to 80wt%. The SEM graphs also explain the broadening of XRD pattern of the 80wt% loading sample.

The particle size of 40wt% loading sample got increased when with 80wt% loading. The increased particle size between 40wt% sample and 80wt% loading shows a

similar effect occurs in the S-TiO_2/MCM-41 catalyst composites (see ***Figure 3.17***).

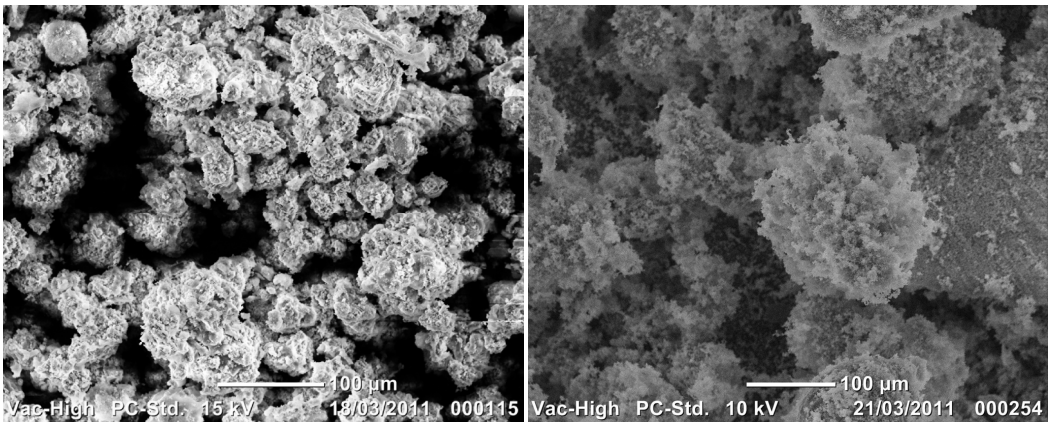

Figure 3.19 *Scanning electron micrographs at 100 nm scale of S-ZrO_2/MCM-41 catalyst composites after calcination. Left: catalyst composite with 40wt% zirconia sulfate loading; Right: catalyst composite with 80wt% zirconia sulfate loading.*

S-Fe_2O_3/MCM-41

Figure 3.20 displays the SEM micrographs of S-Fe_2O_3/MCM-41 catalyst composites. This prism crystal structure can be found from the 40wt% and 80wt% loading samples. Also, metal compound agglomeration increases mean particle size of samples from 40wt% to 80wt% compounds loadings. This is similar to the behaviour of S-TiO_2/MCM-41 and S-ZrO_2/MCM-41 samples.

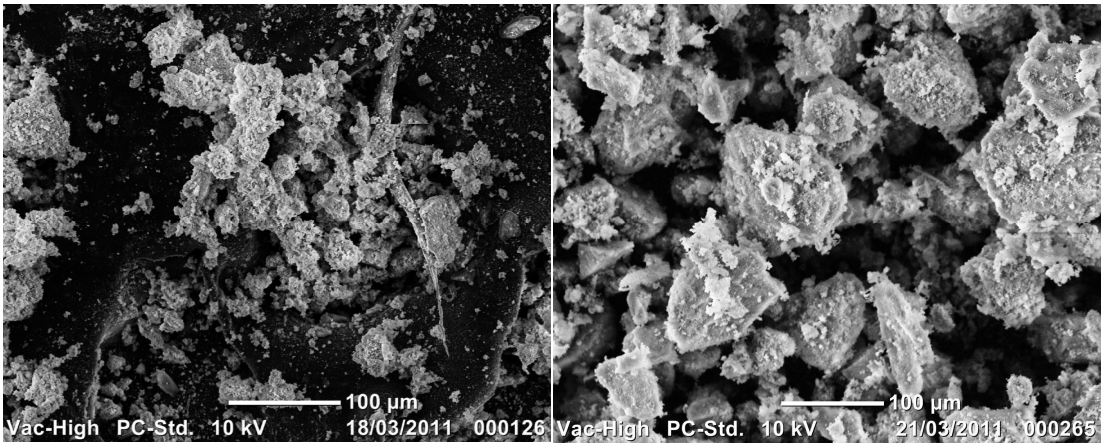

Figure 3.20 *Scanning electron micrographs at 100 nm scale of S-Fe_2O_3/MCM-41 catalyst composites after calcination. Left: catalyst composite with 40wt% ferric oxide sulfate loading; Right: catalyst composite with 80wt% ferric oxide sulfate loading.*

The SEM and XRD method can directly and clearly provide us information on the structure and texture variations among the three groups of catalyst composites at the micro-scale. However, for a more accurate and adequate determination of their specific surface area, pore structure, reasons for the catalyst agglomeration and their relations with esterification rates at nano-scale. The nitrogen adsorption isotherm method was used in solving these problems.

3.3.2 Catalysts surface area and porosity determination

Specific surface area and porosity determination of the catalyst composites were carried out by the nitrogen adsorption-desorption isotherm method. This kind of gas physic-sorption onto the monolayer coverage allows probing of the entire surface and pore interiors (Lowell, Shields, Thomas, & Thommes, 2004). From the nitrogen adsorption-desorption isotherms, pore volume, pore size and their distribution, and the specific surface area of the catalyst samples can be determined by the appropriate calculation methods, i.e. B.E.T. and B.J.H. theory.

Nitrogen at 77 K is an ideal adsorbent to determine the catalysts surface capacities. This is not only due to its low cost, and inert nature, but it produces well defined saturation on the (porous) solid surface. It also allows sufficient nitrogen to be adsorbed onto the solid surface to give an accurate measure of the pore volumes (Osborne, 2004).

Nitrogen adsorption-desorption isotherms Physical adsorption is a physical process of attraction atoms (through van der Waals force) from the adjacent gas to an exposed solid surface. Adsorption of nitrogen involves the monolayer molecule adsorption

stage, the multilayer/capillary condensation stage, and the total pore volume coverage stage.

This reversible (adsorption & desorption) process is usually described by the isotherms. That is, the amount of adsorbate onto the adsorbent as a function of its pressure at constant temperature.

Figure 3.21 displays the nitrogen adsorption isotherm of MCM-41 sample.

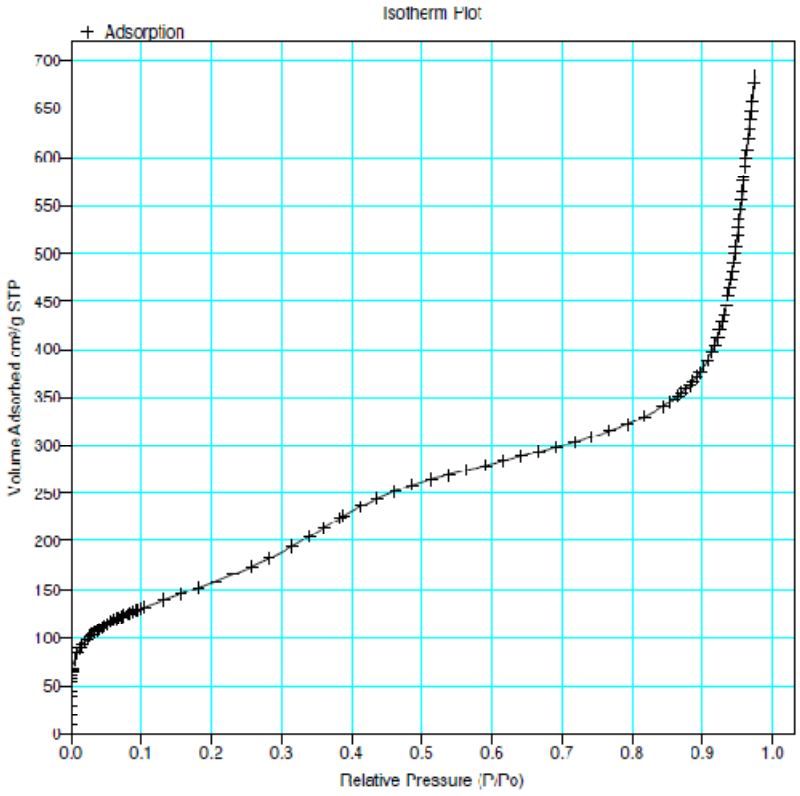

Figure 3.21 *MCM-41 adsorption isotherm plot after 23hrs nitrogen adsorption.*

From ***Figure 3.21***, the adsorption isotherm with plateaus at high P/P_0 (from 0.5 to 0.8) can be observed. Type IV isotherms (refer to Appendix) are typical for this MCM-41mesoporous material. Desorption data indicates the phenomena of capillary condensation occurs within the pore structure which means the presence of the

well-defined open-ended cylindrical-like pore channels.

This type of nitrogen adsorption-desorption isotherm described by Lowell et al. (Lowell et al., 2004) is divided into six steps (refer to ***Figure 3.22***): after completion of the monolayer formation (A), multilayer adsorption commences (B). After reaching a critical film thickness (C), capillary condensation occurs essentially in the core of the pore (transition from configuration C to D). The plateau region of the isotherm reflects the situation where the pores are completely filled with liquid and separated from the bulk gas phase by a hemispherical meniscus. Pore evaporation therefore occurs with a receding meniscus (E) at a pressure which is less than the pore condensation pressure. The desorption process occurs at lower pressures than the adsorption process which results in a hysteresis loop. The pressure where the hysteresis closes corresponds again to the situation of an adsorbed layer film which is in equilibrium with a vapour in the core of the pore and the bulk gas phase. In the relative pressure range between (F) and (A) adsorption and desorption are reversible.

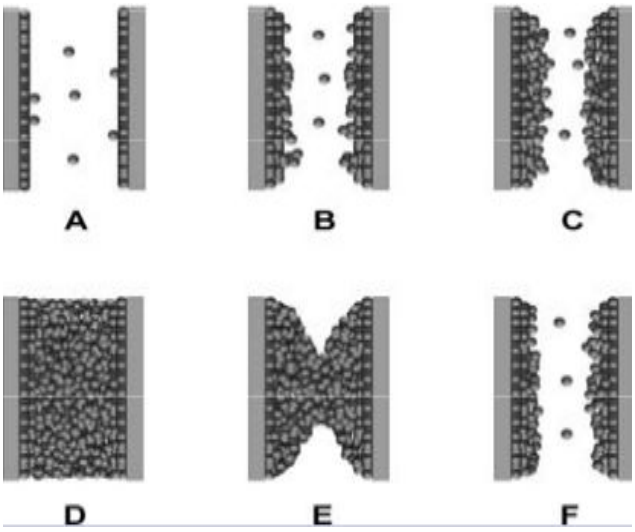

Figure 3.22 *Schematic illustrations of the pore adsorption (combine with* ***Figure 3.21****), pore condensation, and hysteresis behavior of a fluid in a single cylindrical mesopore, reprinted from* (Lowell et al., 2004).

B.E.T. theory for surface area determination B.E.T. surface area is the adsorption of gas to the estimation of the specific surface area *S* (m^2g^{-1}, total surface area per gram) of the porous powder. The B.E.T. surface area is calculated through the B.E.T. equation (Brunauer, Emmett, & Teller, 1938).

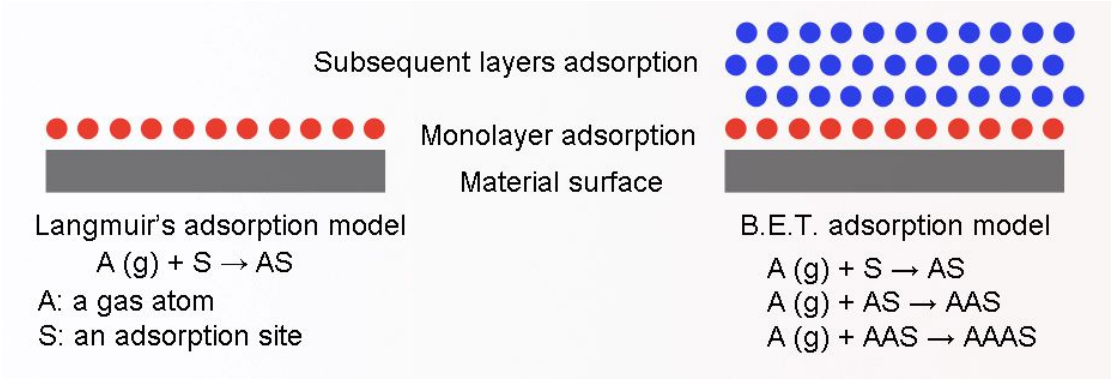

Figure 3.23 *Langmuir's theory assumes at the maximum adsorption, only a monolayer of the adsorbent (i.e. nitrogen) is formed which is always unrealistic. The B.E.T. theory addressed this problem for the multilayer atoms distributed onto the material (porous) surface.*

Extended by the Langmuir's monolayer adsorption theory (Langmuir, 1916) (***Figure 3.23***), the B.E.T. equation (3.5) presents the adsorptions of multilayer gas of the solid surfaces (Yang, 1987):

$$\frac{P}{\nu\,(P_0 - P)} \quad \frac{1}{\nu\ c} \quad \frac{c-1}{\nu\ c}\,\frac{P}{P_0} \qquad 3.5$$

Where the B.E.T. constant is given by (3.6):

$$c \quad \exp\frac{Q - Q}{RT} \qquad 3.6$$

Where Q_1 is the heat of adsorption for the first layer, and Q_L is that for the second and

higher layers and is equal to the heat of gas liquefaction. v is the adsorbed gas quantity. The value v_m is experimentally determined.

By using experimental data in the range of P/P_0 = 0.05 to 0.3, the left-hand side of equation (3.5) is plotted against the relative pressure (see ***Figure 3.24***), and the slope and intercept yield the values of v_m and c. Then a total surface area S_{total} and a specific surface area S can be evaluated by equation (3.7) (Yang, 1987):

$$S_{BET,t} = \frac{\upsilon \, Ns}{V} ; S_{BET} = \frac{S_t}{a} \quad 3.7$$

N: Avogadro's number; s: adsorption cross section; V: molar volume of adsorbent gas; a: molar mass of adsorbed species.

Table 3.4 and ***Figure 3.24*** display the relative pressure plot as illustrated above, B.E.T. surface area plot and the surface area summarize report of the MCM-41 mesoporous silica catalyst by using the nitrogen adsorption-desorption isotherms.

Table 3.4 *Relative pressure range from 0.05 to 0.30 for MCM-41 catalyst B.E.T. surface area calculation.*

Relative Pressure	Volume Adsorbed (cm^3/g, STP)	1/ [VA*(P_0/P-1)]
0.04835	127.182	0.00040
0.09840	148.440	0.00074
0.18261	175.045	0.00128
0.23197	190.226	0.00159
0.29501	213.706	0.00196

The relative linear graph is plotted in ***Figure 3.24***,

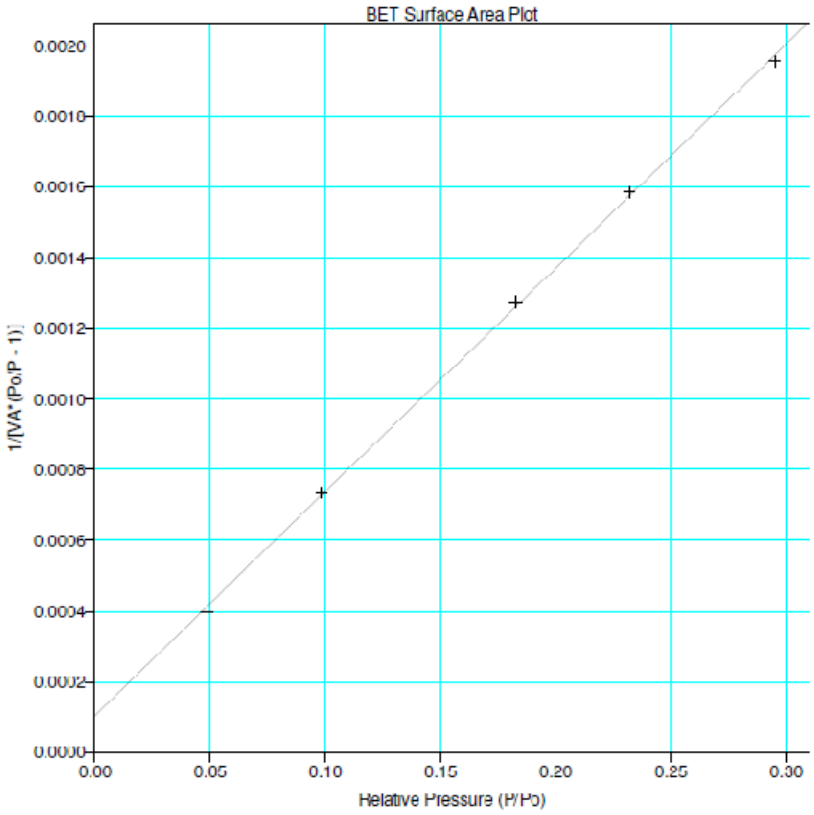

Figure 3.24 *B.E.T. surface area plot for the specific surface area calculation.*

B.E.T. specific surface area of the MCM-41 mesoporous silica catalyst (*m*) is **675.89 m^2g^{-1}** according to the B.E.T. theory calculation.

Determination for pore volume Total pore volume is calculated through the total volume of adsorptive (i.e. N_2) adsorbed within the pores. To calculate the total pore volume, a relative pressure as close to unity as possible should be chosen (Lowell & Shields, 1991).

For MCM-41 catalyst, if W_a grams of nitrogen are adsorbed at P/P_0 = 0.9665 (saturation pressure, 790.45 mmHg), according to the ideal gas law, gas N_2 mole volume adsorbed is converted to the liquid one, then the corresponding volume of pores V_P can be given by (3.8)

$$V_P \quad \frac{W}{\rho_l} \qquad 3.8$$

At boiling point 77 K, density of liquid nitrogen is 0.808 cm^3g^{-1}. Thus, the corresponding total pore volume of MCM-41 catalyst sample is **<u>1.09 cm^3g^{-1}</u>**.

Using this assumption and that of geometry, the average pore diameter d_p can be calculated from the ratio of the total pore volume and the B.E.T. surface area from the following equation (3.9):

$$d \quad \frac{4V_P}{S_{B.E.T.}} \qquad 3.9$$

Adsorption average pore diameter of MCM-41 catalyst is **<u>6.59 nm</u>** according to the calculation.

S-TiO_2/MCM-41 surface area and porosity determination

As presented the N_2 adsorption isotherms of group I catalyst composites in ***Figure 3.25***, all the samples with different S-TiO_2 loading (i.e. from 40wt% to 80wt%) show isotherms of type IV, characteristic of MCM-41 type ordered mesoporous materials. These samples still maintain the mesoporosity structure after high temperature calcination and with various amounts of metal compound dispersion.

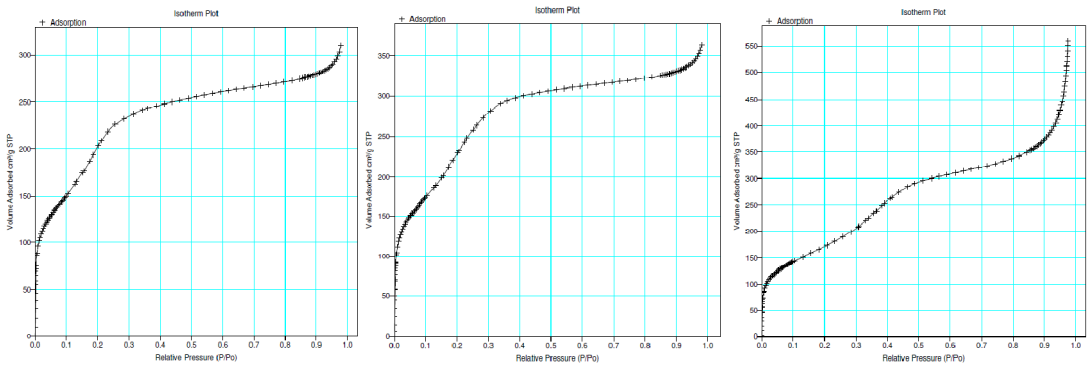

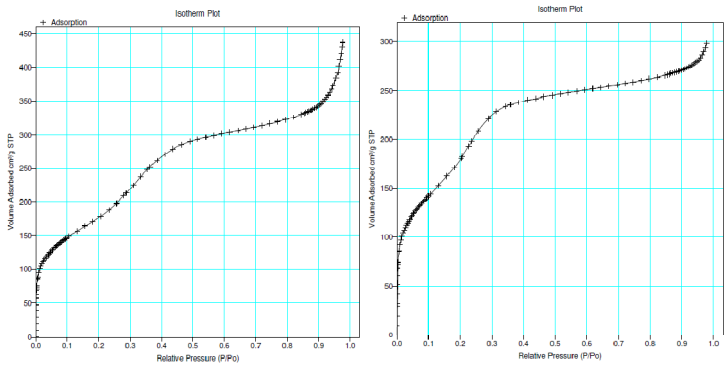

Figure 3.25 *Nitrogen adsorption isotherms of S-TiO_2/MCM-41 samples, from left to right, up to down: e_i, 40wt% to a_i, 80wt%.*

From the surface area and porosity information in ***Table 3.5***, BJH pore volume and average pore diameter of the group I catalyst composites are all significantly smaller than MCM-41. This indicates the successful distribution of sulfated titania within the mesoporous pore channels by using the direct impregnation method in keeping the porous structure.

Table 3.5 *Surface area and porosity properties of the group I catalyst composites.*

wt% TiO_2 in S-TiO_2/MCM-41	BET S. S. A. (m^2g^{-1})	BJH cumulative pore volume (cm^3g^{-1})	BJH average pore diameter (nm)
e_i, 40 wt%	656	0.72	5.36
d_i, 50 wt.%	753	0.48	4.13
c_i, 60 wt.%	616	0.30	3.43
b_i, 70 wt.%	635	0.22	3.19
a_i, 80 wt.%	632	0.20	2.88
m, MCM-41	676	1.09	6.59

B.E.T. specific surface area (average: 658.4 m^2g^{-1}) still remains high for the group I catalysts which means they are able to provide enough spaces for the interactions to

happen among the reactants. This can also be proved by the high esterification rates (average 76.2%) of *n*-butyl acetate by using the group I catalyst composites. No obvious trend was found on the specific surface area results which may be attributed to the metal compounds coated onto the surface of the mesoporous material as well as inside the in the open-ended channels.

In addition, within the group I samples, decreasing BJH pore volume (from 0.72 to 0.20 cm^3g^{-1}) and average diameter (from 5.36 to 2.88 nm) with increasing loading contents of sulfate titania means the gradually accumulation of the metal compounds inside the pore channels. This tendency can also be learnt from the pore size distribution curves in ***Figure 3.26***.

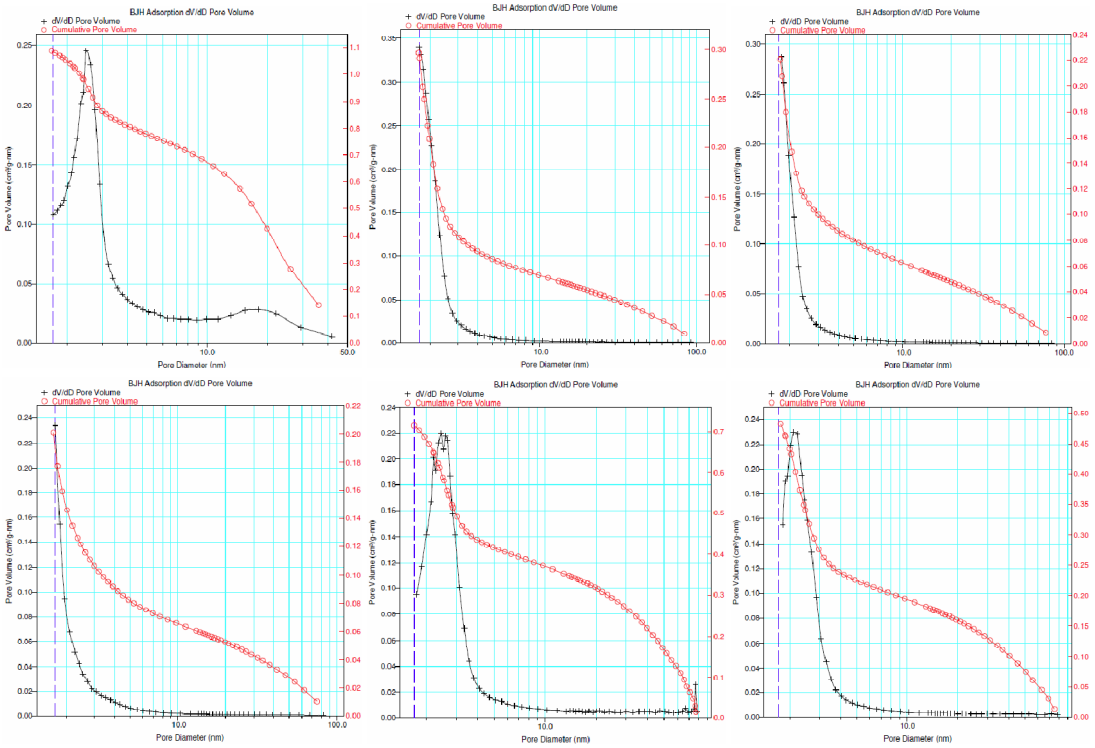

Figure 3.26 *The pore size distribution curves of MCM-41 and various (40wt% to 80wt% loadings) S-TiO_2/MCM-41 samples (from left to right, up to down).*

S-ZrO_2/MCM-41 surface area and porosity determination

For the N_2 adsorption isotherms of group II catalyst composites in ***Figure 3.27***, catalyst samples with 40wt% and 70wt% loadings exhibits the type IV isotherms, characteristic of MCM-41 type ordered mesopores. While for the catalyst sample with 80wt% loading, this kind of structure disappears, giving a type II isotherm. Type II sorption isotherms are typically obtained in the case of non-porous or macroporous adsorbents, where unrestricted monolayer-multilayer adsorption can occur (Lowell et al., 2004). This indicates the porous structure of S-ZrO_2/MCM-41 catalyst composites was lost with high loadings (i.e. 80wt%) of sulfated zirconia. This can be shown from the BJH pore volume 0.09 cm^3g^{-1}.

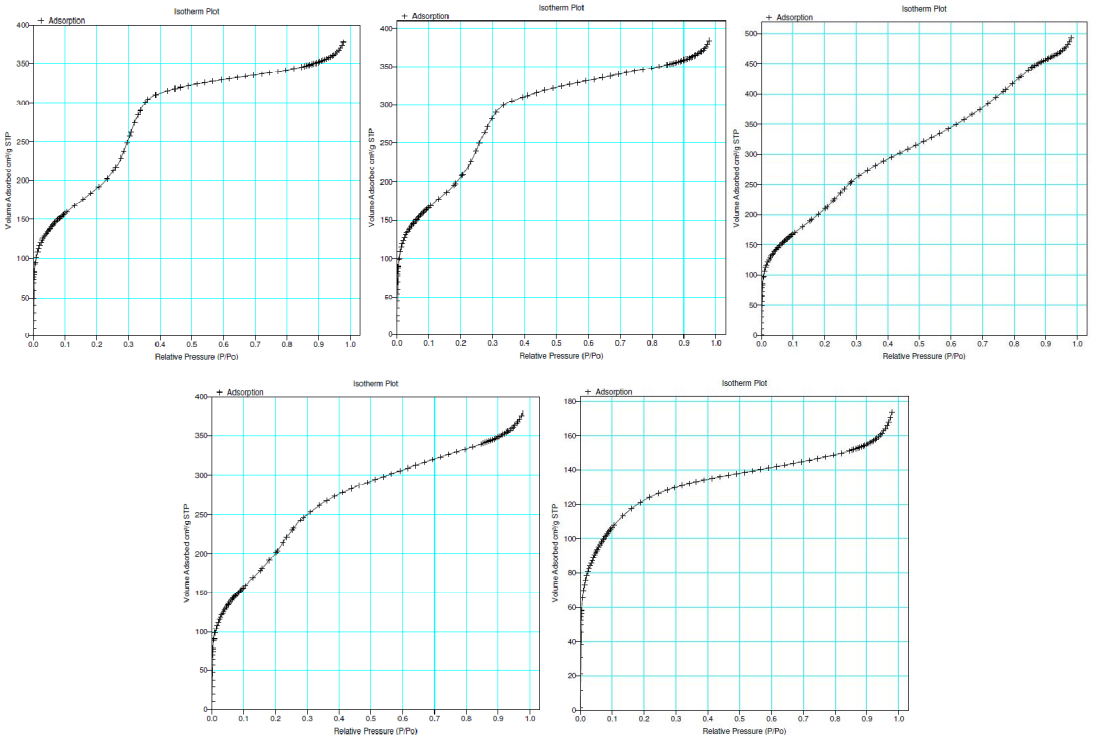

Figure 3.27 *Nitrogen adsorption isotherms of S-ZrO_2/MCM-41 samples, from left to right, up to down: e_{ii}, 40wt% to a_{ii}, 80wt%.*

For group II catalyst composites, 40wt% to 70wt% sulfated zirconia samples still have the trends similar with group I: decreasing pore volume and pore diameter with increasing metal compound loadings (see ***Table 3.6*** and ***Figure 3.28***). This also proved the direct impregnation method in keeping the porous structure up to 70wt%

zirconia sulfate loadings within the mesoporous pore channels.

Table 3.6 *Surface area and porosity properties of the group II catalyst composites.*

wt% ZrO_2 in S-ZrO_2/MCM-41	BET S. S. A. (m^2g^{-1})	BJH cumulative pore volume (cm^3g^{-1})	BJH average pore diameter (nm)
e_{ii}, 40 wt%	683	0.55	3.92
d_{ii}, 50 wt.%	726	0.45	3.40
c_{ii}, 60 wt.%	748	0.39	2.73
b_{ii}, 70 wt.%	707	0.33	2.63
a_{ii}, 80 wt.%	456	0.09	5.03
m, MCM-41	676	1.09	6.59

B.E.T. specific surface area results for e_{ii} to b_{ii} catalyst samples are relatively higher than group I catalyst composites in ***Table 3.5*** with average 664 m^2g^{-1}. This may be the cause of their higher catalytic performance (*n*-butyl-acetate esterification rate 87.4%) than group I samples. Also, the disordered specific surface area results indicate the re-distribution of metal compounds onto the MCM-41 surface. For sample e_{ii} (i.e. 80wt%), surface area decreased to 456 m^2g^{-1} due to the porous structure blockage. However, e_{ii} catalytic activity still exhibits the highest catalytic activities for the esterification rate (96%) which indicates the large surface and porous structure of these catalysts do not plays the critical role in their catalytic activities. The catalytic activities may also depend on their acid strength, acid types or types of transition metal compounds.

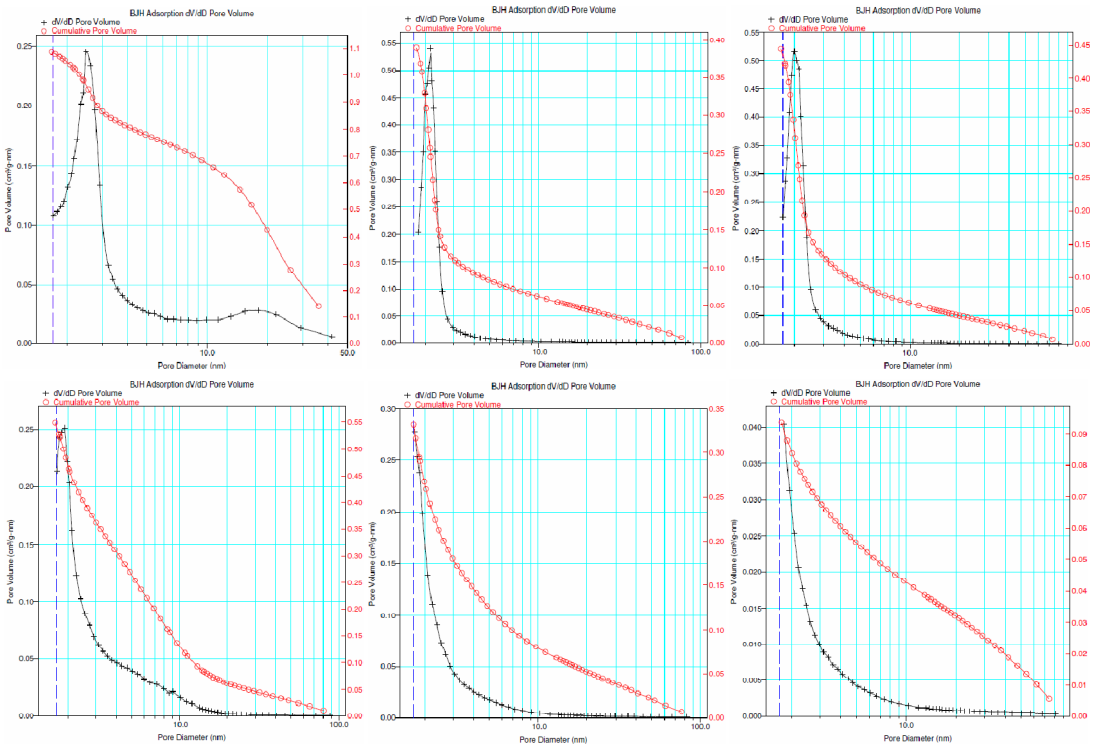

Figure 3.28 *The pore size distribution curves of MCM-41 and various (40wt% to 80wt% loadings) S-ZrO_2/MCM-41 samples (from left to right, up to down).*

S-Fe_2O_3/MCM-41 surface area and porosity determination

Nitrogen adsorption isotherms of group III catalyst composites in ***Figure 3.29*** show that for only 40wt% and 50wt% sulfated ferric oxides loading has the type IV isotherm, whereas the rest of them exhibit type II isotherms. This indicates the blockage of mesoporous structure of S-Fe_2O_3/MCM-41 catalyst composites with metal compound loadings higher than 50wt%.

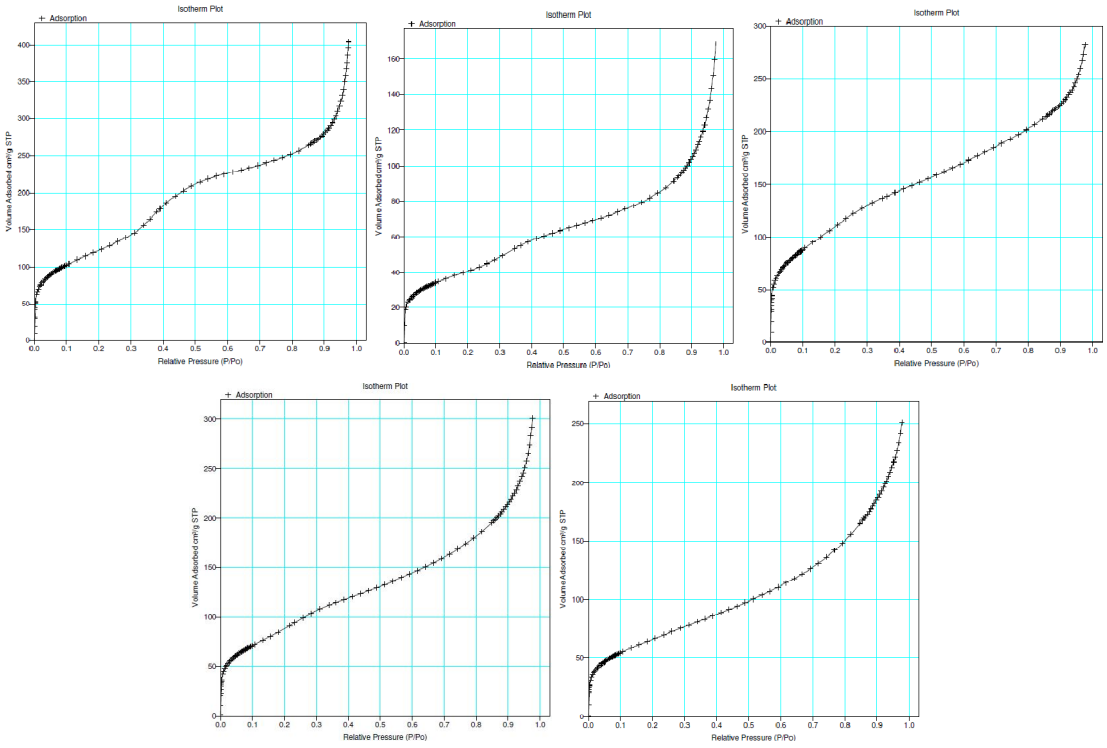

Figure 3.29 *Nitrogen adsorption isotherms of S-Fe_2O_3/MCM-41 samples, from left to right, up to down: e_{iii}, 40wt% to a_{iii}, 80wt%.*

Because of the blockage of the pore structure, B.E.T. specific surface area results of group III catalyst composites are the lowest (average: 309 m^2g^{-1}) among the three groups. They are also relatively low compared to the non-impregnated MCM-41 catalyst. This may explain their having the lowest catalytic activities: 71.6% of *n*-butyl acetate esterification rates among the three groups of the catalyst composites.

Table 3.7 *Surface area and porosity properties of the group III catalyst composites.*

wt% Fe_2O_3 in S-Fe_2O_3/MCM-41	BET S. S. A. (m^2g^{-1})	BJH cumulative pore volume (cm^3g^{-1})	BJH average pore diameter (nm)
e_{iii}, 40 wt%	442	0.50	5.53
d_{iii}, 50 wt.%	152	0.24	7.70
c_{iii}, 60 wt.%	394	0.31	5.14
b_{iii}, 70 wt.%	316	0.38	6060
a_{iii}, 80 wt.%	241	0.32	7.07
m, MCM-41	676	1.09	6.59

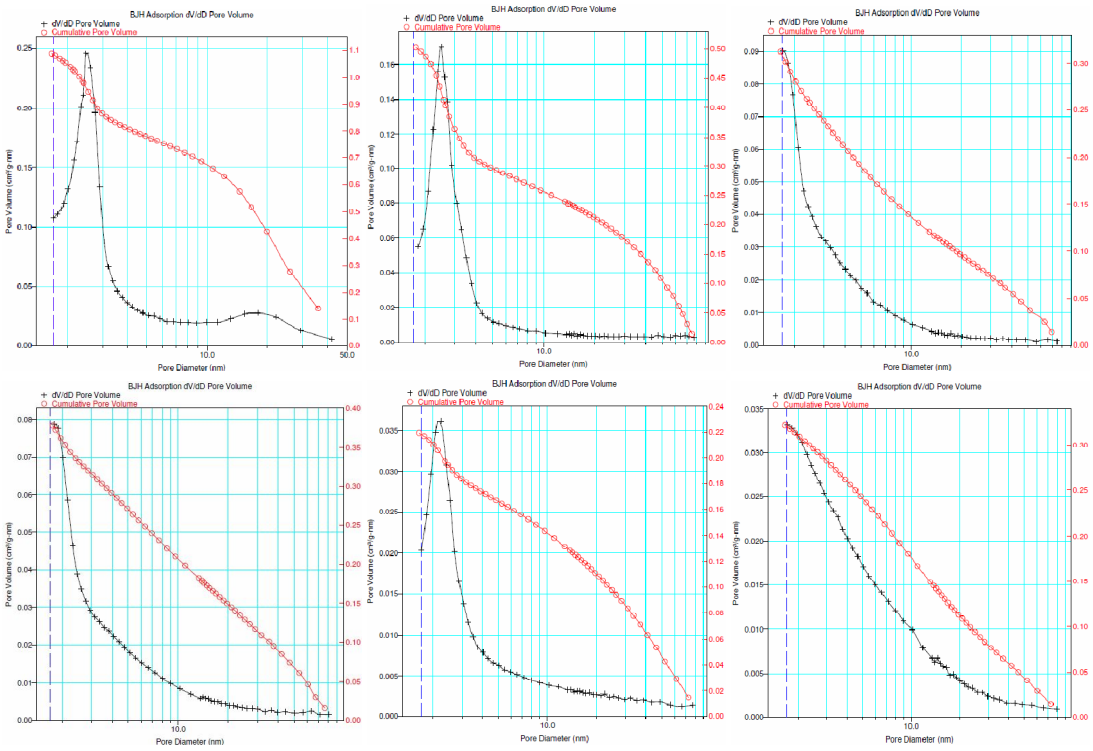

Figure 3.30 *The pore size distribution curves of MCM-41 and various (40wt% to 80wt% loadings) S-Fe_2O_3/MCM-41 samples (from left to right, up to down).*

3.4 Nature of Active Sites

3.4.1 Acidity measurements of solid superacid catalysts

IR spectroscopy Infrared (IR) spectroscopy is the investigation and measurement of the IR spectra produced from the molecules absorbing IR electromagnetic radiation (Rao, 1963). As a molecule absorbs IR radiation, it will cause energy changes within the molecule according to the Planck's Law: $E = h\nu$. Here, E refers to the radiation energy while ν is the frequency of the radiation (Kendall, 1966). The IR spectra of the molecule can thus be produced by the transitions between the vibrational and rotational energy levels.

'In-situ' DRIFTS pyridine adsorption The DRIFTS technique, based on the optical phenomenon known as the diffuse reflectance along with the Fourier transform IR spectroscopy is commonly applied to obtain the spectra of powders with minimum sample preparation (Ryczkowski, 2001). The diffuse reflection spectroscopy is associated with reflectance of electromagnetic radiation from the dull surfaces which is then collected and analyzed.

For solid superacid catalysts, DRIFT has been the most frequently used technique in identifying and characterizing adsorption species and intermediates on the surface active sites. This is because of the ease of sample preparation, sensitivity to surface species, and its capability of controlling the environmental conditions (Centeno, Carrizosa, & Odriozola, 1998; Sambeth et al., 2000; D. Song, Li, & Cai, 2007; Sun et al.).

In our present research, the heterocyclic amine, pyridine (C_5H_5N) is used as the basic probe molecule in investigating the strength of adsorption of basic molecules onto the acid sites. The relatively strong basicity ($pK_b = 9$) of pyridine will avoid it reacting with some of the weaker acid sites (Parry, 1963).

This basic probe molecule is useful in forming the conjugated acid, $C_5H_5NH^+$ which is ideal as the base probe for the IR spectroscopic catalysis study: the Brönsted acidity can be characterized by looking at the pyridine protonation by the site; while Lewis acidity can be accessed from the shift of the IR bands that are sensitive to the Lewis acid-pyridine interaction (Busca, 2006). The conjugated reactants of pyridine with the two types of acid sites can be recorded through the IR spectra.

In realizing the introduction of pyridine into the acid catalysts, the reaction is required to occur under '*in-situ*' condition, namely under 'the reaction mixture' condition. With a cell operating as a catalytic reactor, this attachment (refer to ***Figure 2.8***) can be a powerful tool for monitoring catalyst deactivation (Voskoboinikov et al., 1998).

Hammett indicator method We have discussed concepts of acid and acidity measurement for solid acid (i.e. Hammett acidity function) in the introduction section. It can be easily understood for the reaction mechanism of the Hammett indicators with solid superacid catalysts.

When the basic indicator, B reacts with a Brönsted acid (AH) to form the corresponding conjugated acid (HB^+) and base (A^-), the acid strength can be expressed by the Hammett acidity function H_0 in the following way (3.10):

$$_0 \quad p \qquad \log B \ / \ BH \qquad (3.10)$$

In the case of the interaction with a Lewis acid site, H_0 is expressed by (3.11):

$$_0 \quad p \qquad \log B \ / \ AB \qquad (3.11)$$

Where [B] is the concentration of the neutral base which reacted with the Lewis acid or electron pair acceptor, A.

From this point of view, the acid strength of solid superacid catalysts can be estimated by noting which members of a series of Hammett indicators adsorbed in the acid form (Corma, 1995).

If the indicator shows the acid colour, the H_0 function value of the surface is the same or lower than the pK_a of the conjugated acid of the indicator. Then the H_0 range can be decided by means of a range of indicators with different pK_a values.

3.4.2 S-TiO_2/MCM-41 active sites

Acidity strength Hammett indicator results of the group I samples are reported in ***Table 3.8***. The positive sign (+) means that the solid presents an acid strength that is higher than that of the indicator. If the acid strength is lower than that of the indicator, it is marked as the negative sign.

The results show that all the group I catalysts have an acid strength of $H_0 \leq +1.2$ which represents a large distribution of acid strength. If indicators with lower $p\mathrm{K_a}$ values (< -10) can be used, more precise measurements of the acidity strength of titania sulfate (≤ -14.52 by reference Yamaguchi, 1990) can be made.

Table 3.8 *Acidity strength of S-TiO_2/MCM-41s by using various Hammett indicators.*

S-TiO_2/MCM-41	H_0 value			
	≤ + 7.2	≤ + 4.8	≤ + 3.8	≤ + 1.2
a_i	+	+	+	+
b_i	+	+	+	+
c_i	+	+	+	+
d_i	+	+	+	+
e_i	+	+	+	+

Here, the Hammett indicator method for determination acid strength shows its limitations. Only one pK_a value per indicator is not accurate enough. Also the solid acid catalyst should be white or colourless. And sometimes the basic or acid colour change it is not sensitive enough to be identified by the naked eye.

Acid sites structures The infrared adsorption spectra for a_i to e_i samples are shown in ***Figure 3.31***.

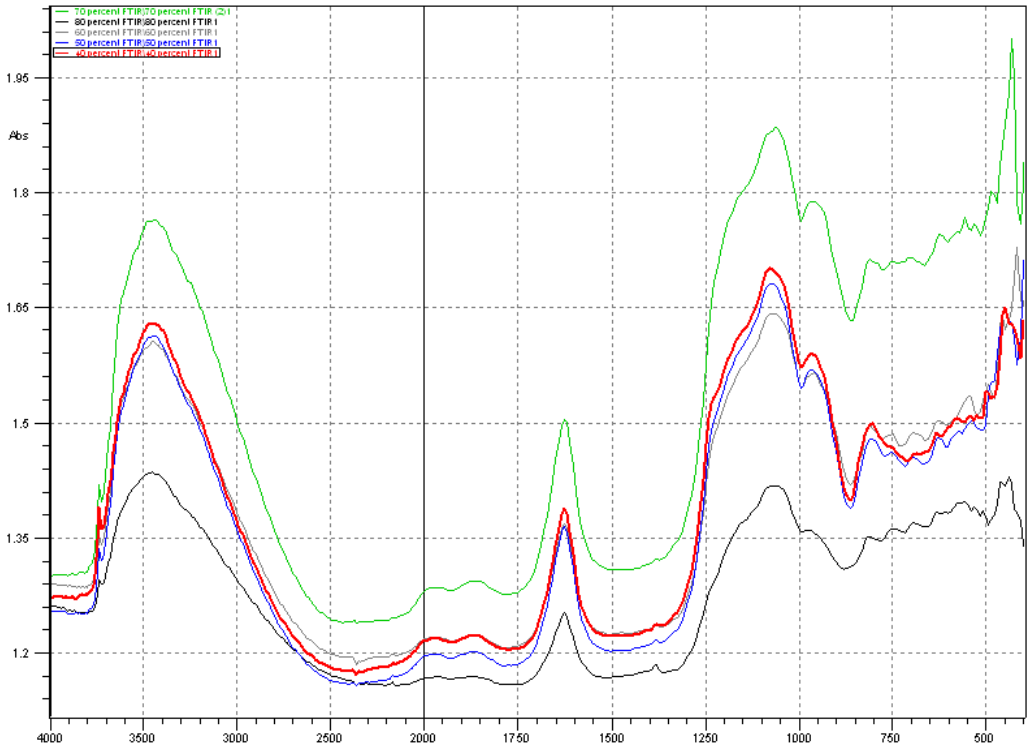

Figure 3.31 *FTIR spectra of group I samples annealed at 623 K for 2 hr.*

A number of researches (Guzman-Castillo et al., 2003; Noda, de Almeida, Probst, & Goncalves, 2005; Ropero-Vega et al., 2010) have proved the two peaks at 980 and 1075 cm^{-1} can be attributed to vibrational modes of bidentate sulfate ions. In sulfated metal oxides, it has been assumed that the sulfate ion is covalently bounded to the oxide. It shows C_{2v} symmetry, when it is bounded by two oxygen atoms forming chelate and bridge structures (see ***Figure 3.32***).

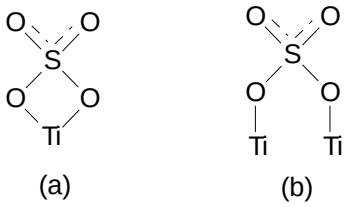

Figure 3.32 *Sulfate structures: (a) coordinated with C_{2v} chelate and (b) C_{2v} bridge.*

IR spectra above have proved the sulfated titania structure exist in the group I catalyst

composites with metal compounds distribution and calcination. Also, the IR spectra indicate that under temperature at 823 K, the C_{2v} symmetry structure still exists in the entire group I samples.

Types of acids From the DRIFT spectra of a_i to e_i samples (see ***Figure 3.33***), four ranges of significant peaks exist around 1450, 1485, 1540 and 1600 to 1640 cm^{-1}. This can be observed after adsorption of pyridine which represents the Lewis and Brönsted acid sites respectively.

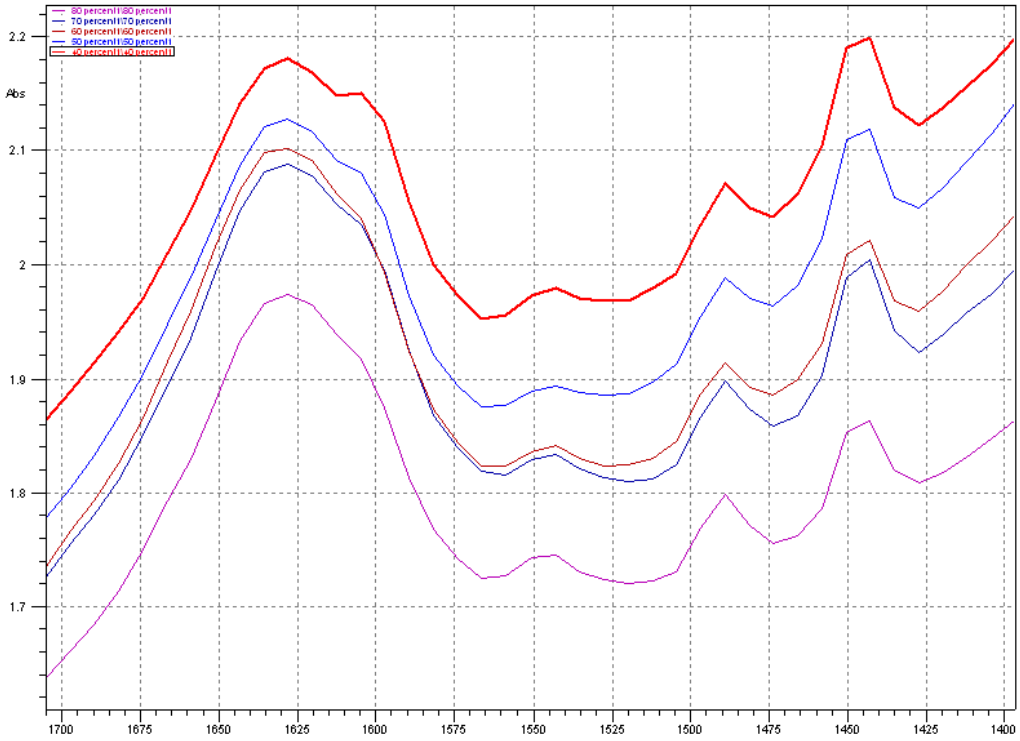

Figure 3.33 *In-situ DRIFT-pyridine adsorption of S-TiO_2/MCM-41 from 80wt% to 40wt% titania sulfate loading at room temperature.*

With the pyridinium ions (PyH^+) formed by the transfer of protons from the acidic hydroxyl groups in the material to the organic base (Ropero-Vega et al., 2010), all the catalysts show the bands at 1450 cm^{-1} which is assigned to the adsorption of coordinated pyridine in Lewis sites. Peaks near 1485 cm^{-1} represent the pyridine chemisorbed either on Lewis or Brönsted acid sites whereas the band around 1540

cm^{-1} can be assigned to the presence of Brönsted acid sites in the solids. In addition, wide bands from 1600 to 1640 cm^{-1} are shown from all the samples indicating the formation of strong Lewis acid sites rather than Brönsted acid sites (Corma, 1995; Dalai, Sethuraman, Katikaneni, & Idem, 1998; Gui et al., 2005; Noda et al., 2005; Parry, 1963).

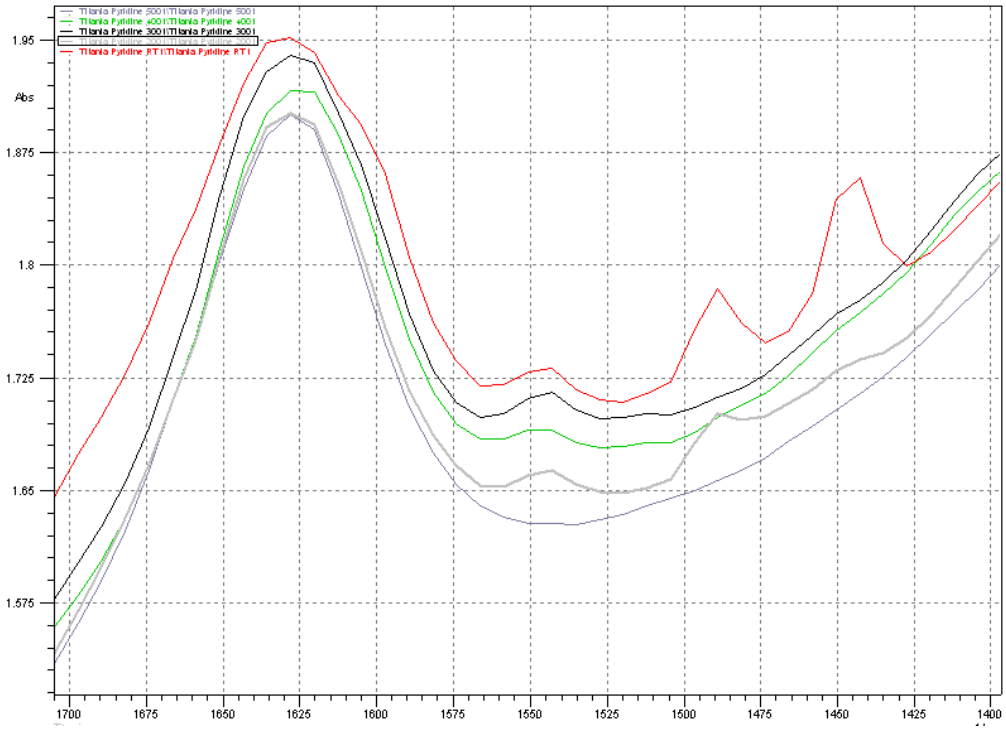

Figure 3.34 *In-situ DRIFT spectra of 80wt% loading S-TiO_2/MCM-41 after adsorption of pyridine and evacuation at different temperatures from 373 to 773 K.*

From ***Figure 3.34***, it can be seen that the number of Brönsted and Lewis acid sites (peaks) slightly decreases as the annealed temperature increases from 373 to 773 K after pyridine adsorption. At 773 K, both of the Brönsted and Lewis acid peaks disappearing which means most of the acid sites decompose as the temperature increases. On the other hand, the strength of the Brönsted acid sites (decomposition up to 673 K) is relative stronger than that of the Lewis acid sites (decomposition up to 473 K) for group I samples.

3.4.3 S-ZrO_2/MCM-41 active sites

Acidity strength Hammett indicator results from ***Table 3.9*** confirm that all the group II catalyst composites have acid strength of $H_0 \leq +1.2$ which presents wide distribution of acid strength.

Table 3.9 *Acidity strength of S-ZrO_2/MCM-41s by using various Hammett indicators.*

S-ZrO_2/MCM-41	H_0 value			
	$\leq +7.2$	$\leq +4.8$	$\leq +3.8$	$\leq +1.2$
a_{ii}	+	+	+	+
b_{ii}	+	+	+	+
c_{ii}	+	+	+	+
d_{ii}	+	+	+	+
e_{ii}	+	+	+	+

Acid sites structures Refer to ***Figure 3.35***, C_{2v} symmetry structures of the vibrational modes of bidentate sulfate ions are found in zirconia sulfate supported on MCM-41 catalyst composites, shown by the two peaks near 950 and 1070 cm^{-1}. This also indicates the sulfated zirconia structure is present in the group II catalyst composites and the stability due to high temperatures.

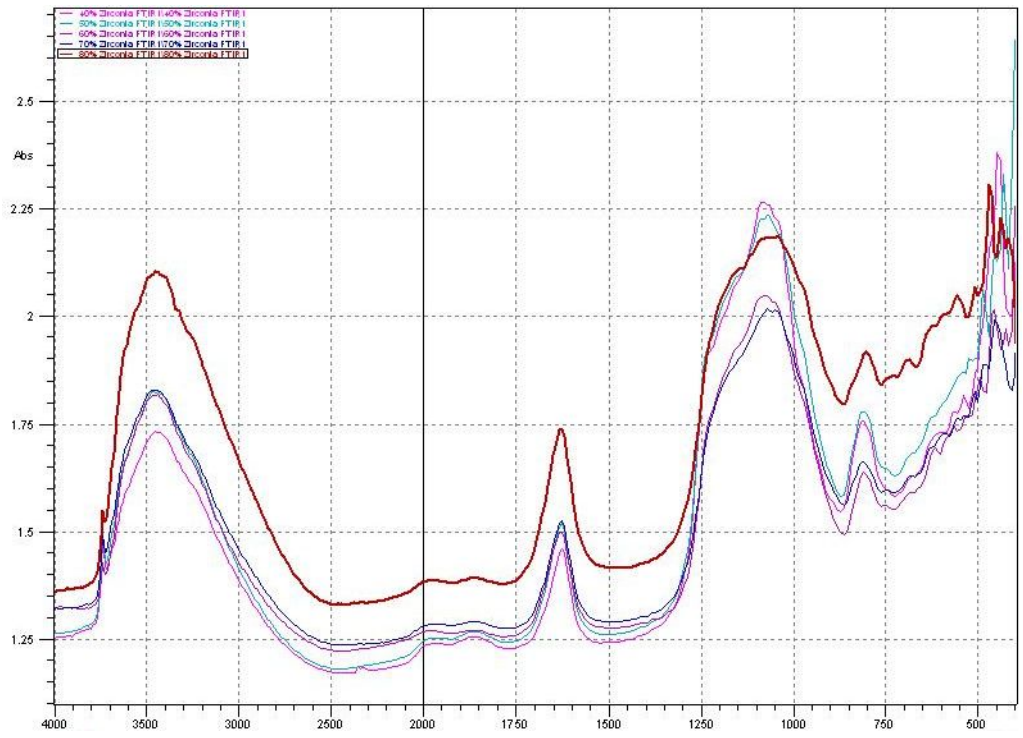

Figure 3.35 *FTIR spectra of group II samples annealed at 623 K for 2 hr.*

Types of acids Figure 3.36 displays the four significant peaks (around 1447, 1489, 1620, 1539 and 1639 cm^{-1}) for the Lewis and Brönsted acid sites of the group II zirconia catalyst composites.

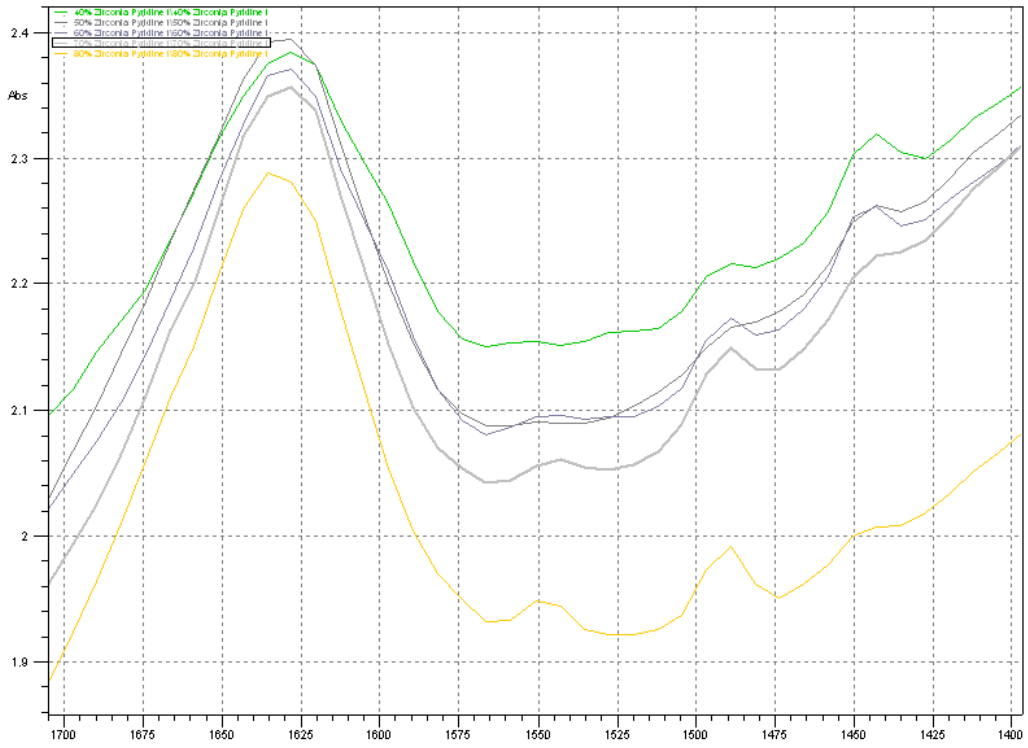

Figure 3.36 *In-situ DRIFT-pyridine adsorption of S-ZrO_2/MCM-41 from 80wt% to 40wt% zirconia sulfate loading at room temperature.*

Similar with the condition of S-TiO_2/MCM-41 catalyst composites from ***Figure 3.37***, here the intensity of Brönsted and Lewis acid sites (peaks) slightly decrease as the annealed temperature increases from 373 to 773 K after pyridine adsorption. At 773 K, both of the Brönsted and Lewis acid sites decomposed. They are not thermally stable enough to resist high temperatures up to 773 K, while until 673 K the Brönsted and acid sites are still stable and the Lewis acid sites disappeared at 573 K.

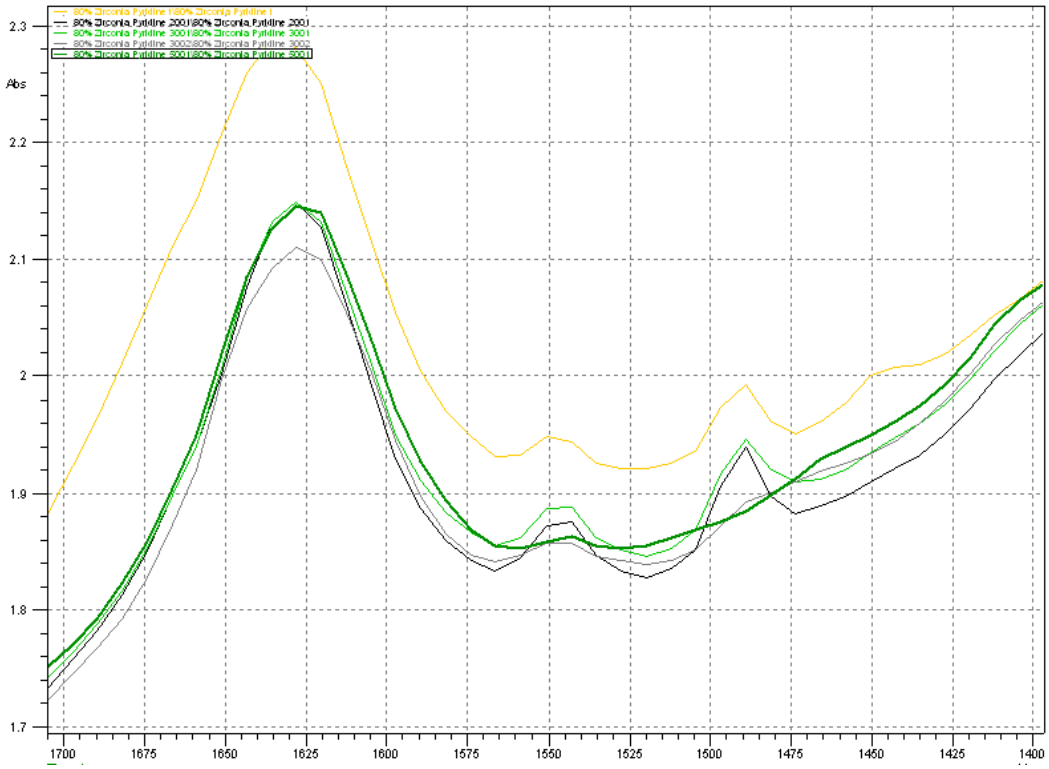

Figure 3.37 *In-situ DRIFT spectra of 80wt% loading S-ZrO_2/MCM-41 after adsorption of pyridine and evacuation at different temperatures from 373 to 773 K.*

3.4.4 S-Fe_2O_3/MCM-41 active sites

Acidity strength For the red colour S-Fe_2O_3/MCM-41 catalyst composites, Hammett indication method shows its limitation for colored samples.

Acid sites structures From ***Figure 3.38*** stretching frequencies of SO_4^{2-} species can be found in the 1240-1000 cm^{-1} region for group III catalyst composites as referred by Yamaguchi (Yamaguchi, 1990). The structures of sulfated iron compounds also exhibit the C_{2v} symmetry after high temperature calcination and remain the same under thermal treatment. These sulfated iron compounds are classified into chelate and bridge bidentate structures (see ***Figure 3.32***).

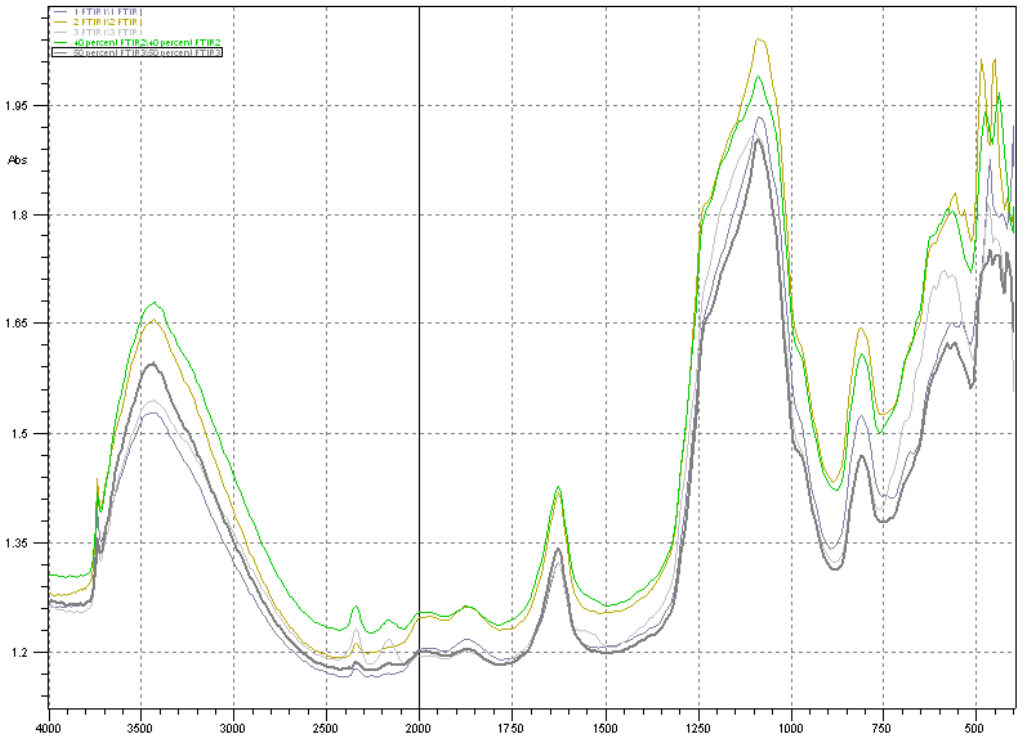

Figure 3.38 *FTIR spectra of group III sample annealed at 623 K for 2 hr.*

Type of acids Characteristic peak signals at positions 1440, 1542, 1487, and wide bands around 1609 and 1629 cm^{-1} correspond to pyridine interaction with both Brönsted and Lewis acid sites which can be found from ***Figure 3.39***.

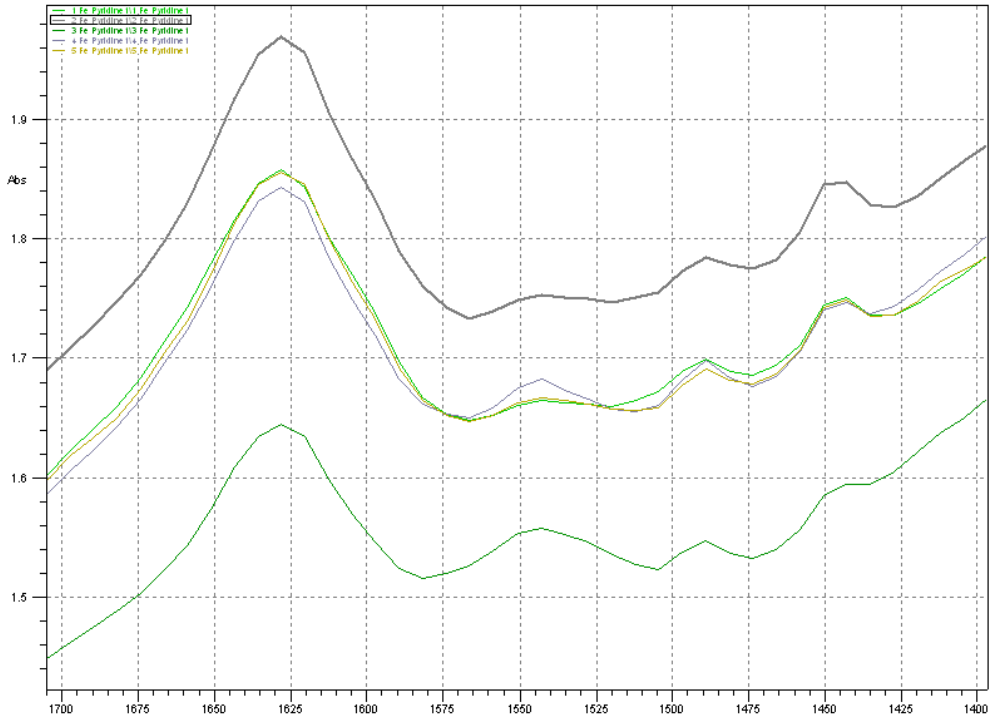

Figure 3.39 *In-situ DRIFT-pyridine adsorption of S-Fe_2O_3/MCM-41 from 80wt% to 40wt% ferric oxide loading at room temperature.*

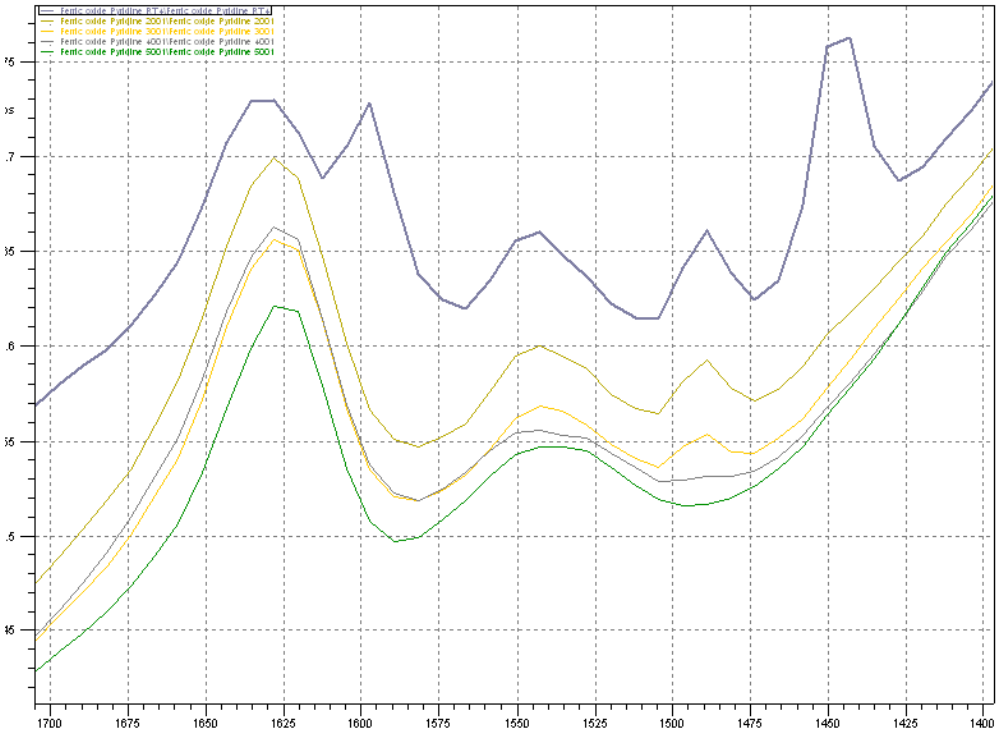

Figure 3.40 *In-situ DRIFT spectra of 80wt% loading S-Fe_2O_3/MCM-41 after*

adsorption of pyridine and evacuation at different temperatures from 373 to 773 K.

Similarly to the case of S-TiO_2/MCM-41 and S-ZrO_2/MCM-41 catalyst composites, intensities of Brönsted and Lewis acid sites (peaks) slightly decreases as the annealed temperature increases from 373 to 773 K after pyridine adsorption. At 773 K, both of the Brönsted and Lewis acid peaks disappear with the decomposition of acid sites as with increased temperature; The strength of the Brönsted acid sites (decomposition up to 673 K) is relative stronger than that of the Lewis acid sites.

For group III samples, the Brönsted acid sites appear to have stronge thermal strength than that of group I and II samples. There is no decomposition for the Brönsted acid sites even when the sample is heated up to 773 K.

For all the three groups of catalyst composites S-TiO_2/MCM-41, S-ZrO_2/MCM-41, and S-Fe_2O_3/MCM-41, the Lewis acid sites appear to be stronger than the Brönsted acid sites. That indicates the Lewis acid sites are more responsible for the catalysts catalytic activities than the Brönsted acid sites. On the other hand, the Brönsted acid sites have higher thermal stability than that of the Lewis sites.

Chapter 4 CONCLUSIONS AND DEVELOPMENTS

4.1 Overall Conclusions

The present research reports the successful preparation of the S-TiO_2/MCM-41, S-ZrO_2/MCM-41, and S-Fe_2O_3/MCM-41 catalyst composites by the direct impregnation method with high metal content loadings.

With this method, S-TiO_2/MCM-41 of up to 80wt% sulfated titania loading can be obtained without destroying the pore structure of MCM-41 after thermal treatments. Decomposition of surfactant CTAB and titania sulfate were found around 200 to 300^{o}C and 350 to 650^{o}C respectively during the formation of the composite. The crystal structure still existed with metal compounds agglomerating on the surface. High specific surface area of the MCM-41 substrate was maintained with the composite. The pore size and volume changed regularly with changes in the amount of S-TiO_2. Both Brönsted and Lewis acid sites were detected in the role of active sites with C_{2v} symmetry and they appear to decrease with the increasing temperature.

S-ZrO_2/MCM-41 with an upper limit of 70wt% sulfated zirconia loading can be obtained without destroying the pore structure of MCM-41 after thermal treatments. Decomposition of surfactant CTAB and zirconia sulfate were found around 220 to 310^{o}C and 500 to 750^{o}C respectively during the formation of the composite which may be attributed to the high stability of the tetragonal polycrystalline structure of zirconia under high temperatures. The crystal structure was found to be lost with over 70wt% metal compound loading. The highest specific surface area of the MCM-41 substrate was detected among these composites. The pore size and volume changed regularly with changes in the amount of S-ZrO_2 within the composites from 40wt% to 70wt% loadings. Both Brönsted and Lewis acid sites were detected in the role of active sites with C_{2v} symmetry. The acid sites showed the weakest thermal stability.

S-Fe_2O_3/MCM-41 with an upper limit of 50wt% sulfated ferric oxide loading can be obtained without destroying the pore structure of MCM-41 after thermal treatment. Decomposition of surfactant CTAB and zirconia sulfate were found around 210 to 300^oC and 300 to 670^oC respectively during the formation of the composite. The crystal structure still existed with metal compounds agglomeration on the surface. These composites showed lowest specific surface area of the MCM-41 substrate among the three groups of catalyst composites. The pore size and volume changed regularly with changes in the amount of S-Fe_2O_3 within the composites for 40wt% and 50wt% loadings. Both Brönsted and Lewis acid sites were detected in the role of active sites with C_{2v} symmetry, and they appeared the strongest thermal stability of their acid sites.

For the *n*-butyl acetate esterification by the S-TiO_2/MCM-41, S-ZrO_2/MCM-41, and S-Fe_2O_3/MCM-41 catalyst composites, three facts affected the esterification rates. They are metal compounds loading, specific surface area, and number of active sites. Both Lewis and Brönsted acid sites were detected in the three groups of catalysts. The Lewis acid sites are more responsible for the catalytic activities, and the Brönsted acid sites have higher thermal stability. The catalytic activity increases with increasing loadings of titania sulfate, zirconia sulfate, or ferric oxides sulfate. S-Fe_2O_3/MCM-41 catalysts showed the lowest conversions for the *n*-butyl acetate esterification because they process relative low B.E.T. surface area for average 309 m^2g^{-1}. This indicates lower specific surface area may lead to lower conversion rates. However, for S-ZrO_2/MCM-41 with 80wt% content loading, the pores blockage the surface area decrease, but it still gave the highest conversion rate. The high conversion rate is related to the high metal compounds loading and acid sites. Thus, the specific surface area has effects but cannot decide the esterification rates absolutely. There is also a trend for the decreasing esterification rate after 4hr on stream. The coke and water formed during the reaction can probably cover the active sites of the catalyst and cause catalyst deactivation.

4.2 Further Developments

For the three catalyst composites S-TiO_2/MCM-41, S-ZrO_2/MCM-41, and S-Fe_2O_3/MCM-41, further studies can be focus on the improvements of their acid sites thermal stabilities. For both S-TiO_2/MCM-41, S-ZrO_2/MCM-41 catalyst composites have good catalytic activities and maintained structure with MCM-41 combination. However, through *in-situ* DRIFT study we found that the Lewis acid sites and Brönsted acid sites got lost with higher than 200^{o}C heating. This means for the catalysts are not able to apply in a wider range of reactions which can limit their usefulness.

For the sulfate promoted transition metal oxides supported on mesoporous silica materials, further studies can be considered in applying a wider range of transition metals such as manganese, vanadium, chromium, etc in their sulfated promoted oxides on the mesoporous silica materials MCM-41 as solid superacid catalyst from the study of their structures and acid natures. And their catalytic activities can be evaluated on a wider range of reactions to get the optimum combinations of the kinds of metal oxides, loading contents and their relative reactions.

REFERENCES

Arata, K., & Hino, M. (1990). Solid catalyst treated with anion: XVIII. Benzoylation of toluene with benzoyl chloride and benzoic anhydride catalysed by solid superacid of sulfate-supported alumina. *Applied Catalysis, 59*(1), 197-204.

Arrhenius, S. (1887). On the dissociation of substances dissolved in water. *Zeitschrift fur physikalische Chemie, 1*, 631-648.

Asim, N., Radiman, S., & Ambar bin yarmo, M. (2009). Preparation of WO3 nanoparticles using cetyl trimethyl ammonium bromide supermolecular template. *American Journal of Applied Sciences, 6*(7), 1424-1428.

Babou, F., Coudurier, G., & Vedrine, J. C. (1995). Acidic properties of sulfated zirconia: an Infrared spectroscopic study. *Journal of Catalysis, 152*(2), 341-349.

Barwell, N. (2002). *Acylation*. from http://www.chm.bris.ac.uk/webprojects2002/barwell/Data/Acylation.html

Bensitel, M., Saur, O., Lavalley, J. C., & Mabilon, G. (1987). Acidity of zirconium oxide and sulfated ZrO2 samples. *Materials Chemistry and Physics, 17*(3), 249-258.

Bevy, L. P. (Ed.). (2005). *Leading Edge Catalysis Research*. New York: NOVA Science Publishers, Inc.

Brønsted, J. N. (1923). Some remarks on the concept of acids and bases. *Recueil des Travaux Chimiques des Pays-Bas, 42*, 718-728.

Brown, W. H. (1995). *Organic chemistry*. Orlando: Saunders College Publishing.

Brunauer, S., Emmett, P. H., & Teller, E. (1938). Adsorption of gases in multimolecular layers. *Journal of the American Chemical Society, 60*(2), 309-319.

Busca, G. (2006). The surface acidity and basicity of solid oxides and zeolites. In J. L. G. Fierro (Ed.), *Metal oxides* (pp. 247-319). Boca Raton: CRC Press.

Carvalho, W. A., Varaldo, P. B., Wallau, M., & Schuchardt, U. (1997). Mesoporous redox molecular sieves analogous to MCM-41. *Zeolites, 18*(5-6), 408-416.

Centeno, M. A., Carrizosa, I., & Odriozola, J. A. (1998). In situ DRIFTS study of the SCR reaction of NO with NH3 in the presence of O2 over lanthanide doped V2O5/Al2O3 catalysts. *Applied Catalysis B: Environmental, 19*(1), 67-73.

Chen, C. L., Cheng, S., Lin, H. P., Wong, S. T., & Mou, C. Y. (2001). Sulfated zirconia catalyst supported on MCM-41 mesoporous molecular sieve. *Applied Catalysis A: General, 215*(1-2), 21-30.

Chen, C. L., Li, T., Cheng, S., Lin, H. P., Bhongale, C. J., & Mou, C. Y. (2001). Direct impregnation method for preparing sulfated zirconia supported on mesoporous silica. *Microporous and Mesoporous Materials, 50*(2-3), 201-208.

Chen, F. R., Coudurier, G., Joly, J. F., & Vedrine, J. C. (1993). Superacid and catalytic properties of sulfated zirconia. *Journal of Catalysis, 143*(2), 616-626.

Clayden, J. (2001). *Organic chemistry* Oxford: Oxford University Press.

Clearfield, A., Serrette, G. P. D., & Khazi-Syed, A. H. (1994). Nature of hydrous zirconia and sulfated hydrous zirconia. *Catalysis Today, 20*(2), 295-312.

Corma, A. (1995). Inorganic solid acids and their use in acid-catalyzed hydrocarbon reactions. *Chemical Reviews, 95*(3), 559-614.

Corma, A., Fornes, V., Juan-Rajadell, M. I., & Nieto, J. M. L. (1994). Influence of preparation

conditions on the structure and catalytic properties of SO4 2-/ZrO2 superacid catalysts. *Applied Catalysis A, General, 116*(1-2), 151-163.

Cui, B., Gao, P., Jin, Q., Zhao, W. Y., & Dong, L. L. (2008). Characterization of solid super acid catalyst modified by La oxide and its catalysis on synthesis of ethgl acetate. *Gao Xiao Hua Xue Gong Cheng Xue Bao/Journal of Chemical Engineering of Chinese Universities, 22*(1), 60-64.

Dalai, A. K., Sethuraman, R., Katikaneni, S. P. R., & Idem, R. O. (1998). Synthesis and Characterization of Sulfated Titania Solid Acid Catalysts. *Industrial & Engineering Chemistry Research, 37*(10), 3869-3878.

Davis, B. H., Keogh, R. A., & Srinivasan, R. (1994). Sulfated zirconia as a hydrocarbon conversion catalyst. *Catalysis Today, 20*(2), 219-256.

Dodd, J. W., & Tsnge, K. H. (1987). *Thermal methods*. London: John Wiley & Sons.

Dunn, J. P., Jehng, J. M., Kim, D. S., Briand, L. E., Stenger, H. G., & Wachs, I. E. (1998). Interactions between surface vanadate and surface sulfate species on metal oxide catalysts. *Journal of Physical Chemistry B, 102*(32), 6212-6218.

Estevao Candeias, A., Ribeiro Carrott, M. M. L., Carrott, P. J. M., Schumacher, K., Grun, M., & Unger, K. K. (2002). *Pore structural characteristics of mesostructured materials prepared under different conditions*, 2002). Retrieved from http://www.scopus.com/inward/record.url?eid=2-s2.0-0036922979&partnerID=40&md5=926ede720d6e4d9a8b3f7cec33064f6a

Gaydhankar, T. R., Samuel, V., Jha, R. K., Kumar, R., & Joshi, P. N. (2007). Room temperature synthesis of Si-MCM-41 using polymeric version of ethyl silicate as a source of silica. *Materials Research Bulletin, 42*(8), 1473-1484.

Gillespie, R. J., Peel, T. E., & Gold, V. (1971). Superacid systems. *Advances in Physical Organic Chemistry, Volume 9*, 1-24.

Giraldo, L. F., Lopez, B. L., Perez, L., Urrego, S., Sierra, L., & Mesa, M. (2007). Mesoporous silica applications. *Macromolecular Symposia, 258*(1), 129-141.

Guan, D., Fan, M., Wang, J., Zhang, Y., Liu, Q., & Jing, X. (2010). Synthesis and properties of magnetic solid superacid: SO4 2-/ZrO2-B2O3-Fe3O4. *Materials Chemistry and Physics, 122*(1), 278-283.

Gui, J., Ban, H., Cong, X., Zhang, X., Hu, Z., & Sun, Z. (2005). Selective alkylation of phenol with tert-butyl alcohol catalyzed by Bronsted acidic imidazolium salts. *Journal of Molecular Catalysis A: Chemical, 225*(1), 27-31.

Guo, H., Chen, Z., & Yan, P. (2010). Preparation and characterization of rare earth solid super acid catalyst SO4 2-/SnO2-Nd2O3 using solft template agent. *Petroleum Processing and Petrochemicals, 41*(10), 58-63.

Guo, Y., Mylonakis, A., Zhang, Z., Yang, G., Lelkes, P. I., Che, S., et al. (2008). Templated synthesis of electroactive periodic mesoporous organosilica bridged with oligoaniline. *Chemistry (Weinheim an der Bergstrasse, Germany), 14*(9), 2909-2917.

Guzman-Castillo, M. L., Lopez-Salinas, E., Fripiat, J. J., Sanchez-Valente, J., Hernandez-Beltran, F., RodrIguez-Hernandez, A., et al. (2003). Active sulfated alumina catalysts obtained by hydrothermal treatment. *Journal of Catalysis, 220*(2), 317-325.

Hall, N. F., & Conant, J. B. (1927). A study of superacid solutions. I. the use of the chloranil electrode in glacial acetic acid and the strength of certain weak bases. *Journal of the American*

Chemical Society, 49(12), 3047-3061.

Hammett, L. P., & Deyrup, A. J. (1932). A series of simple basic indicators. I. the acidity functions of mixtures of sulfuric and perchloric acids with water. *Journal of the American Chemical Society, 54*(7), 2721-2739.

Hatakeyama, T., & Quinn, F. X. (1994). *Thermal analysis*. Chichester: John Wiley & Sons Ltd.

Hino, M., & Arata, K. (1979a). Reaction of butane to isobutane catalyzed by iron oxide treated with sulfate ion. solid superacid catalyst. *Chemistry Letters, 8*(10), 1259-1260.

Hino, M., & Arata, K. (1979b). Reactions of butane and isobutane catalysed by titanium oxide treated with sulphate ion. Solid superacid catalyst. *Journal of the Chemical Society, Chemical Communications*(24), 1148-1149.

Hino, M., & Arata, K. (1980a). Polymerization of ethyl and methyl vinyl ethers catalyzed by iron oxide treatei with sulfate ion. synthesis of stereospecific poly. (methyl vinyl ether). *Chemistry Letters, 9*(8), 963-964.

Hino, M., & Arata, K. (1980b). Synthesis of solid superacid catalyst with acid strength of H0 < -16.04. *Journal of the Chemical Society, Chemical Communications*(18), 851 - 852.

Hino, M., Kobayashi, S., & Arata, K. (1979). Solid catalyst treated with anion. 2. Reactions of butane and isobutane catalyzed by zirconium oxide treated with sulfate ion. Solid superacid catalyst. *Journal of the American Chemical Society, 101*(21), 6439-6441.

Jenkins, R. (1976). *An introduction to X-ray spectrometry*. London: Heyden.

Jenkins, R., & Snyder, R. L. (1996). *Introduction to X-ray powder diffractometry* (Vol. 138). New York: John Wiley & Sons, Inc.

Kendall, D. N. (1966). Infrared radiation: description and simple theory of absorption by molecules. In D. N. Kendall (Ed.), *Applied infrared spectroscopy* (pp. 2-30). New York: Reinhold Publishing Corporation.

Kleitz, F. *Ordered nanoporous materials: synthesis, characterization and functionalization methods*). Retrieved from http://nano.uib.no/abstracts/kleitz.html

Koyano, K. A., & Tatsumi, T. (1997). Synthesis of titanium-containing MCM-41. *Microporous Materials, 10*(4-6), 259-271.

Kresge, C. T., Leonowicz, M. E., Roth, W. J., Vartuli, J. C., & Beck, J. S. (1992). Ordered mesoporous molecular sieves synthesized by a liquid-crystal template mechanism. *Nature, 359*(6397), 710-712.

Langmuir, I. (1916). The constitution and fundamental properties of solids and liquids. Part I. Solids. *The Journal of the American Chemical Society, 38*(2), 2221-2295.

Lei, T., Xu, J. S., Tang, Y., Hua, W. M., & Gao, Z. (2000). New solid superacid catalysts for n-butane isomerization: [gamma]-Al2O3 or SiO2 supported sulfated zirconia. *Applied Catalysis A: General, 192*(2), 181-188.

Lekhal, A., Glasser, B. J., & Khinast, J. G. (2001). Impact of drying on the catalyst profile in supported impregnation catalysts. *Chemical Engineering Science, 56*(15), 4473-4487.

Lekhal, A., Glasser, B. J., & Khinast, J. G. (2004). Influence of pH and ionic strength on the metal profile of impregnation catalysts. *Chemical Engineering Science, 59*(5), 1063-1077.

Lekhal, A., Khinast, J. G., & Glasser, B. J. (2001). Predicting the effect of drying on supported coimpregnation catalysts. *Industrial & Engineering Chemistry Research, 40*(18), 3989-3999.

Lewis, G. N. (1923). *Valence and the structure of atoms and molecules.* New York: The Chemical Catalog Co., Ltd.

Li, Y., Zhang, X. D., Sun, L., Xu, M., Zhou, W. G., & Liang, X. H. (2010). Solid superacid catalyzed fatty acid methyl esters production from acid oil. *Applied Energy, 87*(7), 2369-2373.

Lowell, S., & Shields, J. E. (1991). *Powder surface area and porosity* (3 ed.). London: Chapman & Hall.

Lowell, S., Shields, J. E., Thomas, M. A., & Thommes, M. (2004). *Characterization of porous solids and powders* (4 ed.). Buston: Kluwer Academic Publisher.

Luo, X. M., Ren, L. F., Zhang, X. L., & Qiang, T. T. (2009). The synthesis of oleic acid polyglycol ester catalyzed by solid super acid. *Journal of Surfactants and Detergents, 12*(1), 1-5.

Magnacca, G., Cerrato, G., Morterra, C., Signoretto, M., Somma, F., & Pinna, F. (2003). Structural and surface characterization of pure and sulfated iron oxides. *Chemistry of Materials, 15*(3), 675-687.

McMurry, J. (2000). *Organic chemistry* (5 ed.). Pacific Grove, CA Brooks/Cole.

McNaught, A. D., & Wilkinson, A. (1997). *IUPCA compendium of chemical terminology* (2 ed.). Oxford: Blackwell Scientific Publications.

Morterra, C., Cerrato, G., Pinna, F., Signoretto, M., & Strukul, G. (1994). On the acid-catalyzed isomerization of light paraffins over a ZrO2/SO4 System: the effect of hydration. *Journal of Catalysis, 149*(1), 181-188.

Mukaida, K.-i., Ishikawa, S., Yoneya, M., Satoh, T., & Watanabe, H. (1988). Variation of topographical and catalytic properties of constituent particles of SO4 2-promoted oxides in the preparation process. *Zairyo/Journal of the Society of Materials Science, Japan, 37*(422), 1313-1318.

Nagaraju, N. (1997). Synthesis of isoamyl acetate using NaX and NaY zeolites as catalysts. *Reaction Kinetics and Catalysis Letters, 61*(1), 155-160.

Noda, L. K., de Almeida, R. M., Probst, L. F. D., & Goncalves, N. S. (2005). Characterization of sulfated TiO2 prepared by the sol-gel method and its catalytic activity in the n-hexane isomerization reaction. *Journal of Molecular Catalysis A: Chemical, 225*(1), 39-46.

Olah, G. A., Prakash, G. K. S., & Sommer, J. (1985). *Superacids*. New York: Wiley.

Osborne, M. (2004). Adsorption isotherms.

Paragen. (2008). *Friedel-Crafts Acylation*. from http://blog.para-gen.com/2008/07/141/friedel-crafts-acylation.html

Parry, E. P. (1963). An infrared study of pyridine adsorbed on acidic solids. Characterization of surface acidity. *Journal of Catalysis, 2*(5), 371-379.

Rao, C. N. R. (1963). *Chemical applications of infrared spectroscopy*. New York: Academic Press Inc.

Rao, C. N. R., & Raveau, B. (1995). *Transition metal oxides*. New York: VCH Publishers

Regalbuto, J. (2007). *Handbook of catalyst preparation* Boca Raton Taylor & Francis.

Roberts, G. K., & Russell, C. A. (2005). *Chemical history: reviews of the recent literature*. Cambridge: Royal Society of Chemistry.

Ropero-Vega, J. L., Aldana-Perez, A., Gomez, R., & Nino-Gomez, M. E. (2010). Sulfated titania [TiO2/SO42-]: A very active solid acid catalyst for the esterification of free fatty acids with ethanol. *Applied Catalysis A: General, 379*(1-2), 24-29.

Rouquerol, J., Avnir, D., Fairbridge, C. W., Everett, D. H., Haynes, J. M., Pernicone, N., et al. (1994). Recommendations for the characterization of porous solids *Pure and Applied Chemistry, 66*(8), 1739-1758.

Ryczkowski, J. (2001). IR spectroscopy in catalysis. *Catalysis Today, 68*(4).

Sambeth, J. E., Centeno, M. A., Paul, A., Briand, L. E., Thomas, H. J., & Odriozola, J. A. (2000). In

situ DRIFTS study of the adsorption-oxidation of CH3OH on V2O5. *Journal of Molecular Catalysis A: Chemical, 161*(1-2), 89-97.

Sayari, A. (1996). Catalysis by Crystalline Mesoporous Molecular Sieves. *Chemistry of Materials, 8*(8), 1840-1852.

Simpson, C. (1970). *Gas Chromatography*. London: Kogan Page.

Sohn, J. R., & Jang, H. J. (1992). Characterization of TiO2---SiO2 modified with H2SO4 and activity for acid catalysis. *Journal of Catalysis, 136*(1), 267-270.

Song, D., Li, J., & Cai, Q. (2007). In ditu diffuse reflectance FTIR study of CO adsorbed on a cobalt catalyst supported by silica with different pore sizes. *The Journal of Physical Chemistry C, 111*(51), 18970-18979.

Song, W., Venimadhavan, G., Manning, J. M., Malone, M. F., & Doherty, M. F. (1998). Measurement of residue curve maps and heterogeneous kinetics in methyl acetate synthesis. *Industrial & Engineering Chemistry Research, 37*(5), 1917-1928.

Sorensen, S. P. L., & Enzymstudien. (1909). Ueber die messung und die bedeutung der wasserstoffionenkonzentration bei enzymatischen prozessen. *Biochem. Zeitschr., 21*, 131-304.

Sun, S., Ding, J., Bao, J., Gao, C., Qi, Z., & Li, C. Photocatalytic Oxidation of Gaseous Formaldehyde on TiO2: An In Situ DRIFTS Study. *Catalysis Letters, 137*(3), 239-246.

Timofeeva, M. N., Matrosova, M. M., Maksimov, G. M., Likholobov, V. A., Golovin, A. V., Maksimovskaya, R. I., et al. (2001). Esterification of n-butanol with acetic acid in the presence of heteropoly acids with different structures and compositions. *Kinetics and Catalysis, 42*(6), 791-795.

Voskoboinikov, T. V., Coq, B., Fajula, F., Brown, R., McDougall, G., & Luc Couturier, J. (1998). An in situ diffuse reflectance FTIR study of the cyclodimerization of 1,3-butadiene over Cu-exchanged zeolites. *Microporous and Mesoporous Materials, 24*(1-3), 89-99.

Wang, J. H., & Mou, C. Y. (2008). Characterizations of aluminum-promoted sulfated zirconia on mesoporous MCM-41 silica: Butane isomerization. *Microporous and Mesoporous Materials, 110*(2-3), 260-270.

Wang, S., Murata, K., Hayakawa, T., Hamakawa, S., & Suzuki, K. (1999). Oxidative dehydrogenation of ethane by carbon dioxide over sulfate-modified Cr2O3/SiO2 catalysts. *Catalysis Letters, 63*(1-2), 59-64.

Wang, Y., Gan, Y., Whiting, R., & Lu, G. (2009). Synthesis of sulfated titania supported on mesoporous silica using direct impregnation and its application in esterification of acetic acid and n-butanol. *Journal of Solid State Chemistry, 182*(9), 2530-2534.

Xia, Q. H., Hidajat, K., & Kawi, S. (2002). Effect of ZrO2 loading on the structure, acidity, and catalytic activity of the SO42-/ZrO2/MCM-41 acid catalyst. *Journal of Catalysis, 205*(2), 318-331.

Yadav, G. D., & Nair, J. J. (1999). Sulfated zirconia and its modified versions as promising catalysts for industrial processes. *Microporous and Mesoporous Materials, 33*(1-3), 1-48.

Yamaguchi, T. (1990). Recent progress in solid superacid. *Applied Catalysis, 61*(1), 1-25.

Yanagisawa, T., Shimizu, T., Kuroda, K., & Kato, C. (1990). The preparation of alkyltriinethylaininonium–kaneinite complexes and their conversion to microporous materials. *Bulletin of the Chemical Society of Japan, 63*(4), 988-992.

Yang, R. T. (1987). *Gas separation by adsorption processes*. Boston: Butterworths.

Ye, F., Dong, Z., & Zhang, H. (2009). n-Hexane isomerization over copper oxide-promoted sulfated

zirconia supported on mesoporous silica. *Catalysis Communications, 10*(15), 2056-2059.

Zhang, J. C., Liu, M., Song, C. S., & Guo, X. W. (2009). Preparation of spherical MCM-41 in water-acetone media. *Shiyou Xuebao, Shiyou Jiagong/Acta Petrolei Sinica (Petroleum Processing Section), 25*(SUPPL. 2), 61-64.

Zhao, D., Feng, J., Huo, Q., Melosh, N., Fredrickson, G. H., Chmelka, B. F., et al. (1998). Triblock copolymer syntheses of mesoporous silica with periodic 50 to 300 angstrom pores *Science, 279*(5350), 548 - 552.

APPENDIX

IUPAC classification – 6 types of ads-desorption isotherms:

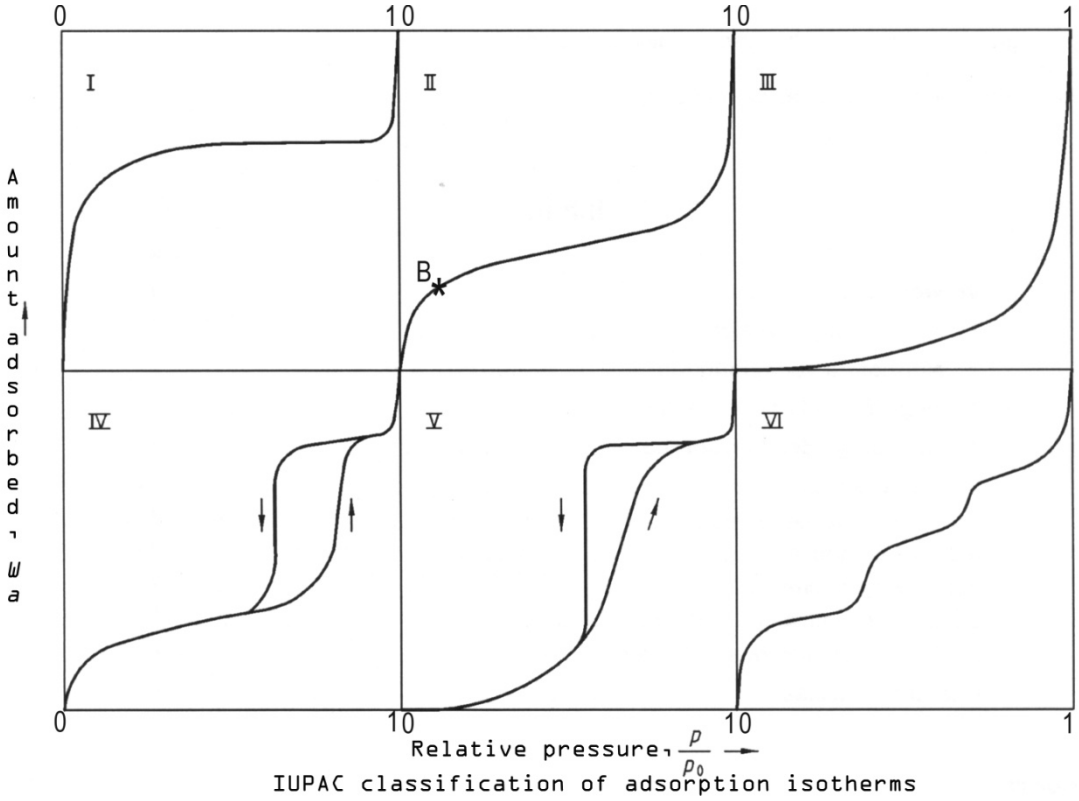

IUPAC classification of adsorption isotherms

Type I – Microporous solids Langmuir isotherm.

Type II – Multilayer adsorption on non-porous / macroporous solids.

Type III – Adsorption on non-porous /macro-porous solids with weak adsorption.

Type IV – Adsorption on meso porous solids with hysteresis loop.

Type V – Same as IV type with weak adsorbate-adsorbent interaction.

Type VI – Stepped adsorption isotherm, on different faces of solid.